

1      **Muon tagging using a Match- $\chi^2$  based Soft Muon**  
2      **Tagger in top quark analyses using data from the**  
3      **ATLAS detector**

4      Jacobo Ezequiel Blanco

5      Department of Physics  
6      Royal Holloway, University of London



7      A thesis submitted for the degree of Doctor of Philosophy

8      May 28, 2014

## DECLARATION

<sup>10</sup> I confirm that the work presented in this thesis is my own. Where information has been derived  
<sup>11</sup> from other sources, I confirm that this has been indicated in the document. Jacobo Ezequiel  
<sup>12</sup> Blanco

**Abstract**

<sup>14</sup> This is an abstract

## Acknowledgements

<sup>16</sup> Thanks Mum!

---

# **Preface**

<sup>17</sup> This thesis describes the calibration and utilization of a soft muon tagger for the purposes of

---

# Contents

19	<b>1 Introduction and motivation</b>	12
20	<b>2 The Standard Model of Particle Physics</b>	13
21	2.1 Quantum Electrodynamics . . . . .	16
22	2.2 Quantum Chromodynamics . . . . .	17
23	2.3 Weak Interactions . . . . .	19
24	2.3.1 Electroweak Unification and the Higgs mechanism . . . . .	23
25		
26	<b>3 Top-quark physics</b>	26
27	3.1 Top quark production . . . . .	27
28	3.2 Top quark decay modes . . . . .	29
29	3.3 Latest developments in top physics . . . . .	31
30	<b>4 The LHC and the ATLAS Detector</b>	37
31	4.1 The Large Hadron Collider . . . . .	37
32	4.1.1 Pileup . . . . .	40
33	4.2 The ATLAS detector . . . . .	41
34	4.2.1 Inner Detector . . . . .	43
35	4.2.2 Calorimetry . . . . .	47
36	4.2.3 Muon spectrometer . . . . .	51
37	4.2.4 Magnet system . . . . .	54
38	4.2.5 Triggering and DAQ . . . . .	54
39	4.3 Athena and ROOT framework . . . . .	54

40	<b>5 Calibration of the Soft Muon Tagger</b>	56
41	5.0.1 Software, Collision Data and Simulated samples . . . . .	57
42	5.1 Tag and Probe Selection . . . . .	57
43	5.1.1 Trigger requirements . . . . .	58
44	5.1.2 Selection Cuts . . . . .	59
45	5.2 Invariant mass fitting . . . . .	61
46	5.2.1 Uncertainty Measurement . . . . .	63
47	5.3 Efficiencies . . . . .	64
48	5.3.1 Isolation dependence . . . . .	64
49	5.3.2 2011 Calibration . . . . .	66
50	5.3.3 Efficiency Binning . . . . .	66
51	5.3.4 Results . . . . .	66
52	<b>6 Measurement of the <math>t\bar{t}</math> cross-section</b>	79
53	6.1 Soft Muon Tagger . . . . .	79
54	6.2 Data and Monte Carlo samples . . . . .	79
55	6.3 Object selection and event selection . . . . .	79
56	6.4 Background estimation . . . . .	80
57	6.4.1 Multijet in the electron channel . . . . .	80
58	6.4.2 Multijet background in the muon channel . . . . .	83
59	6.4.3 $W+jets$ background . . . . .	84
60	6.5 Systematic uncertainties . . . . .	85
61	6.6 Results and conclusion . . . . .	85
62	<b>7 Muon Tagging in a boosted <math>t\bar{t}</math> environment</b>	86
63	7.1 Data samples . . . . .	87
64	7.2 Boosted event topology . . . . .	87
65	7.3 Signal muon selection . . . . .	89
66	7.3.1 Muon selection . . . . .	89
67	7.4 Efficiency definition . . . . .	92
68	7.5 Results . . . . .	95
69	7.5.1 Background . . . . .	95

70	7.6 B-tagging potential in boosted events . . . . .	97
71	<b>8 Conclusions</b>	<b>99</b>
72	<b>Appendices</b>	<b>100</b>
73	<b>A List of triggers used in calibration</b>	<b>101</b>
74	<b>B List of combined muon performance (MCP) cuts</b>	<b>104</b>

---

# 75 List of Figures

76      2.1	The interaction vertex described by QED. One can obtain all possible vertex 77      shapes by rotating this basic vertex and assigning the appropriate electric charge 78      and making sure to conserve lepton number across the vertex. . . . .	16
79      2.2	LO feynman diagrams of the process $e^+e^- \rightarrow e^+e^-$ allowed in QED. Additional 80      vertices can be added to produce higher-order diagrams of the same pro- 81      cess. . . . .	17
82      2.3	Diagrams of the fundamental interaction vertices described by quantum chro- 83      modynamics. Shown are (a) Gluon emission from a quark, (b) Gluon emission 84      from a gluon and finally (c) the four-gluon vertex. . . . .	19
85      2.4	The neutral current and charged current vertices allowed via the weak force. 86      Where $f$ can be an $e$ , $\mu$ or $\tau$ and $\nu_\ell$ is the corresponding lepton neutrino of the 87      same flavour. One can obtain all possible interaction vertices by rotating these 88      basic vertices and assigning the appropriate electric charge and making sure to 89      conserve lepton flavour across the vertex. . . . .	19
90      2.5	Neutral current weak scattering vertex . . . . .	20
91      3.1	The leading order Feynman diagrams for $t\bar{t}$ production. . . . .	28
92      3.2	Example Feynman diagrams for single top quark at leading order. . . . .	29
93      3.3	Branching ratios of all possible $t\bar{t}$ decays. These probabilities are based on the 94      branching-ratios of $W$ decay shown in Table 3.2. . . . .	31
95      3.4	Example event display of a dilepton $t\bar{t}$ event recorded by ATLAS. . . . .	32

---

96	3.5	The feynman diagram of lepton plus jets channel including $t\bar{t}$ production via gluon fusion and decay with a leptonically decaying $W^+$ . Note that all other production mechanisms are also considered and the final state where the $W^-$ is decayed leptonically is also taken into account. . . . .	32
100	3.6	A summary of all $t\bar{t}$ production cross section measurements performed at the LHC at $\sqrt{s} = 7$ TeV. Note the theory prediction shown as a dotted black line with its associated uncertainties as grey bands. The results shown above the black line have been statistically combined, producing the results labelled as <b>combined</b> . Many of these analyses have been superseded and the results are shown below the line. Other analyses performed but not included in the combination are also shown below the line. . . . .	34
107	3.7	A summary of the most precise $t\bar{t}$ production cross section measurements performed at the LHC at $\sqrt{s} = 7$ and 8 TeV and the Tevatron at $\sqrt{s} = 1.96$ TeV compared to the theoretical prediction. Note that the Tevatron results should be compared against the prediction for $p\bar{p}$ collisions while the LHC against the $pp$ collision predictions. . . . .	35
112	4.1	The layout of CERN complex of experiments, note the main four LHC experiments located at different points around the ring. . . . .	38
114	4.2	Shown in (a) is the number of bunches colliding at the LHC and (b) the peak luminosity per unit time. . . . .	39
116	4.3	Distribution of the total integrated luminosity delivered by the LHC and the recorded by ATLAS for the 2011 and 2012 $pp$ collision period. Note the $\sqrt{s}$ changing from 7 TeV to 8 TeV between 2011 and 2012. . . . .	41
119	4.4	Number of interactions per bunch for the 2012 $pp$ data-taking period at ATLAS per day. Note that both the average number of interactions for all bunches and the maximum number of interactions are shown. . . . .	42
122	4.5	An overview diagram of the ATLAS experiment. Shown are all detection and tracking systems and the toroid magnet which encompasses them. Note also the muon system on the outside of the detector. . . . .	43
125	4.6	caption . . . . .	44

126	4.7 An event-display of an event as reconstructed by the ATLAS inner detector. Shown are the results of the vertexing algorithm where each line represents a track. the purple tracks have been fitted to a secondary vertex. . . . .	45
127		
128		
129	4.8 Plan-view of a quarter-section of the ATLAS ID showing the major detector elements with its active dimensions and envelopes. Note also the $\eta$ markers showing the maximum coverage up to $\eta = 2.5$ . . . . .	45
130		
131		
132	4.9 A drawing of in the transverse plane of the ATLAS ID showing all major de- tection elements in the barrel regions. Note the charged particle track marked in red traversing all the detector elements. . . . .	46
133		
134		
135	4.10 A cut-away diagram of the ATLAS detector highlighting the calorimetry sys- tem. Shown are the ECal barrel and end-cap, the HCal barrel and end-cap and the FCal end-cap. . . . .	48
136		
137		
138	4.11 Cut-away diagram of the EM calorimeter barrel at $\eta = 0$ . Shown are the three different layers with varying cell structures. The strip section is designed to enhance particle identification and position measurement in $\eta$ . . . . .	50
139		
140		
141	4.12 Cut-away drawing of the ATLAS muon system. . . . .	52
142		
143	4.13 Plan view of quarter-section of the ATLAS muon spectrometer. . . . .	53
144		
145	4.14 Transverse view of the muon system. Shown are the . . . . .	53
146		
147	4.15 Diagram of the ATLAS toroid magnet system. The red central solenoid is lo- cated closest to the beam surrounded by layers of tile calorimetry. The eight barrel toroid magnets are shown along with the offset end-cap toroids at each end. . . . .	55
148		
149		
150	5.1 The distribution of $\chi^2_{\text{match}}/N_{\text{dof}}$ for all muon probes for ATLAS collision data and prompt $J/\psi$ Monte Carlo simulation. . . . .	61
151		
152	5.2 A diagram of the various components of the fit procedure. The composite fit is shown along with the corresponding implied signal and background. The two variations of the background shape are also shown. . . . .	62

---

153	5.3	Invariant mass distributions of tag and probe pairs at a) probe level and at b) muon probe level in collision data. Note the various components of the fit as well as the variations on the background fits and the $3\sigma$ and $5\sigma$ integration windows used for systematics. Note the fit parameters and their respective uncertainties . . . . .	65
158	5.4	$\chi^2_{\text{Dof}}$ efficiencies and scale factor with respect to $\sum E_T$ . . . . .	67
159	5.5	$\chi^2_{\text{Dof}}$ efficiencies and scale factor with respect to $\sum p_T$ . . . . .	68
160	5.6	$\chi^2_{\text{Dof}}$ efficiencies and scale factor with respect various isolation variables. . . .	69
161	5.7	$\chi^2_{\text{match}}$ efficiencies and scale factor with respect to the (a) $\phi$ and (b) $\eta$ . . . .	71
162	5.8	$\chi^2_{\text{match}}$ efficiencies and scale factor with respect to the transverse momentum of the muon probe . . . . .	72
164	5.9	$\chi^2_{\text{match}}$ efficiencies and scale factors in the crack region of the detector for side (a) A and (b) C . . . . .	73
166	5.10	$\chi^2_{\text{match}}$ efficiencies and scale factors in the barrel region of the detector for side (a) A and (b) C . . . . .	74
168	5.11	$\chi^2_{\text{match}}$ efficiencies and scale factors in the transition region of the detector for side (a) A and (b) C . . . . .	75
170	5.12	$\chi^2_{\text{match}}$ efficiencies and scale factors in the endcap region of the detector for side (a) A and (b) C . . . . .	76
172	5.13	$\chi^2_{\text{match}}$ efficiencies and scale factors in the forward region of the detector for side (a) A and (b) C . . . . .	77
174	5.14	$\chi^2_{\text{match}}$ efficiencies and scale factor with respect to impact parameter $d_0$ for muon probes with $p_T$ in the range (a) 4 to 6GeV, (b) 6 to 8GeV and (c) 8 to 10GeV. The measurement was carried out only on Period B of 2012 ATLAS collision data. . . . .	78
178	6.1	A diagram of the $E_T$ -isolation phase space. Shown are the four regions as defined by the event selection. . . . .	81
180	7.1	This figure shows a simple diagram for the possible configuration of final-state objects in a (a) boosted and (b) non-boosted events. Note that in both cases a muon is embedded within the $b$ -jet . . . . .	88

183	7.2	The angular separation ( $\Delta R$ ) between the truth $W$ muon and the corresponding $b$ -quark for all examined $Z'$ mass points. . . . .	89
184	7.3	The transverse momentum of the top/anti-top quarks in the event for all examined $Z'$ mass points. . . . .	90
185	7.4	The angular separation ( $\Delta R$ ) between the $b$ and $\bar{b}$ in the event for all examined $Z'$ mass points. . . . .	91
186	7.5	This figure shows the distribution of (a) transverse momentum and (b) pseudo-rapidity of muons which pass the SMT selection, the (c) angular separation between those muons and the nearest jet in the event and (d) the $\chi^2_{\text{match}}$ used in the selection for all tested $Z'$ mass points. . . . .	92
187	7.6	This figure shows the (a) transverse momentum and (b) pseudo-rapidity of muons which pass the MI10 selection, the (c) angular separation between those muons and the nearest jet in the event and (d) the cone size used in the selection for all tested $Z'$ mass points. . . . .	93
188	7.7	Structure of the efficiency measurement. . . . .	94
189	7.8	Efficiency of mini-isolation ( $k_T=10$ ) and $\chi^2_{\text{match}}$ tagger as a function of the angular separation between the reconstructed muon and the nearest reconstructed jet. Note the dip in the mini-isolation efficiency at low $\Delta R$ . In the nominal analysis an overlap removal between the jet and the muon is applied. . . . .	96
190	7.9	Efficiency of mini-isolation ( $k_T=10$ ) and $\chi^2_{\text{match}}$ muon tagger as a function of the transverse momentum of the muon. . . . .	97
191			
192			
193			
194			
195			
196			
197			
198			
199			
200			
201			
202			
203			

---

# List of Tables

205	2.1	A summary of all elementary particles described by the SM [1]. Note the various groupings and divisions including by spin, generation and particle type. For each particle the charge ( $q$ ), mass and name are shown as per the legend on the bottom-right. . . . .	15
209	2.2	A summary of the four fundamental forces ordered by relative strength. These are approximate relative strengths for the purpose of demonstrating the hierarchy of forces as a function of their strength. A more accurate determination of the interaction strength depends on the details of the interaction itself. Note however the order-of-magnitude differences in the relative strengths of these forces. Note that the graviton is the theoretical boson responsible for mediating gravitational interactions, it is not part of the SM. . . . .	16
216	3.1	Summary of the predicted SM single top production [2] and top pair production [3] cross sections at the LHC for $\sqrt{s}=7$ and 8 TeV. . . . .	29
218	3.2	Branching ratios for the decay of $W$ boson. Note that “hadrons” refers to a possible combination of $q\bar{q}'$ where $\bar{q}'$ denotes the antiquark of a flavour different to that of the first quark. [1] . . . . .	30
221	4.1	Design energy resolution of all ATLAS calorimeter components. The resolution is made of a sampling term ( $1/\sqrt{E}$ ) associated with the choice of passive and active materials and construction of the layers and a constant term associated with the depth of the detector, cracks and dead material. . . . .	49
225	4.2	Main parameters of the muon system. . . . .	52

226	4.3	Summary of spatial and temporal resolutions per chamber for all chamber types used in the the ATLAS muon spectrometer. Adapted from [4]. . . . .	54
228	5.1	Pseudorapidity regions of the ATLAS detector . . . . .	66
229	5.2	Data/MC Scale Factors for 2012 Data in all five regions of the detector as a function of $p_T$ . The uncertainties include systematic and statistical components as described in Section 5.2.1 . . . . .	70
231	6.1	Multijet SMT event taggin-rate(in percent) in regions A) inverted- $\cancel{E}_T$ , non- isolated, B) High- $\cancel{E}_T$ , non-isolated and C) low- $\cancel{E}_T$ , isolated. . . . .	82
232	6.2	Multijet estimates in the e+jets obtained by the jet-electron method. The un- certainties are combined statistical and systematics. A systematic uncertainty of 50% is used on the jet-electron pretag event yields [5] in addition to e uncer- tainties obtained on $R_{\text{WGT}}^{\text{SMT}}$ . . . . .	82
233	7.1	Muon reconstruction selection used by Mini-Isolation and by Muon Tagging .	91
234	7.2	Efficiency of selecting a muon by using the $\chi^2_{\text{match}}$ tagger against mini-isolation. Note that ‘MI10 + Overlap’ is the efficiency of applying both the mini-isolation cut and overlap removal. . . . .	96
235	7.3	Fake rate of $\chi^2_{\text{match}}$ tagger, mini-isolation and mini-isolation including overlap removal as measured using all $Z'$ mass points. . . . .	97
236	7.4	Summary of the number of muons remaining after each selection cut and the efficiency. . . . .	98
237			
238			
239			
240			
241			
242			
243			
244			
245			

<sup>246</sup> **Chapter 1**

<sup>247</sup> **Introduction and motivation**

## <sup>248</sup> Chapter 2

# <sup>249</sup> The Standard Model of Particle <sup>250</sup> Physics

<sup>251</sup> Particle physics, or high-energy physics, is the study of the most fundamental constituents  
<sup>252</sup> of matter and their interactions. The best current description of these interactions is known  
<sup>253</sup> as The Standard Model of Particle Physics (SM); a group of theories that cover all currently  
<sup>254</sup> known particles and their interactions. The SM was developed through-out the latter half of  
<sup>255</sup> the 20th century and has seen tremendous success in predicting the behaviour of our universe  
<sup>256</sup> at the most fundamental level. The SM has stood the test of time and rigorous examination  
<sup>257</sup> by numerous experiments. Additionally many of its parameters have been measured with  
<sup>258</sup> tremendous precision e.g. the electron magnetic moment  $g$  is known to  $10^{-13}$  [6]. The last piece  
<sup>259</sup> to be confirmed was the existence of the Higgs boson, which in turn points to the existence  
<sup>260</sup> of the so-called Higgs field. Evidence of the elusive Higgs were observed by the ATLAS and  
<sup>261</sup> CMS experiments at CERN [7, 8]. Despite its tremendous success, the SM cannot account and  
<sup>262</sup> explain for all observed phenomenon in the universe. Firstly, the theory requires many of  
<sup>263</sup> its parameters to be measured empirically. The theory does not a priori provide a value for  
<sup>264</sup> these parameters such as the number of particle generations. Additionally the theory does  
<sup>265</sup> not describe the most familiar of the forces, gravity. Furthermore, the SM does not provide a  
<sup>266</sup> candidate for dark matter or dark energy, which according to recent measuremetns accounts for  
<sup>267</sup> more than 90% of the total energy density in the universe [9]. The asymmetry between matter  
<sup>268</sup> and antimatter is also not fully explained by the SM. rite something about radiative corrections

269 to higgs mass and the hierarchy problem As such there is a strong focus on developing theories  
270 which go beyond the standard model (BSM) to provide an answer to these open questions. The  
271 discussion in this chapter is largely based on [10] and [11].

272 The SM describes the nature of the interactions of the fundamental constituents of our  
273 universe in terms of the three different fundamental forces: strong, weak and electromagnetic,  
274 each described by a specific theory. As mentioned before, the most familiar of the forces,  
275 gravity, is not described by the SM. The SM classifies particles into several categories depending  
276 on their properties and allowed interactions. Particles which have a half-integer spins (e.g.  
277  $S = \frac{1}{2}, \frac{3}{2}, \dots$ ) are known as *fermions*, these are the basic constituents of matter. Particles  
278 with integer spins (e.g.  $S = 0, 1, \dots$ ) are known as *bosons*, these mediate interactions between  
279 fermions and other bosons.

280 Fermions can be divided into two subgroups: quarks, which can interact via the strong,  
281 weak and electromagnetic forces and leptons which can only interact by the weak and elec-  
282 tromagnetic forces. There are six known leptons: electron  $e$ , muon  $\mu$  and tau  $\tau$ , which all  
283 have electric charge<sup>1</sup>  $Q = 1$ , and the corresponding electrically neutral neutrino  $\nu_e$ ,  $\nu_\mu$  and  $\nu_\tau$ .  
284 Analogously, six quark *flavours* are known:  $u$ ,  $c$  and  $t$ , with electric charge  $Q = +2/3$  and  $d$ ,  
285  $s$  and  $b$ , with electric charge  $Q = -1/3$ .

286 Quarks and leptons are divided into three generations, which differ only by the mass and  
287 flavour of their constituent fermions, each generation being heavier than the previous. A sum-  
288 mary of all elementary particles described by the SM can be found in Table 2.1.

289 For every matter fermion ( $f$ ) there is an equivalent antimatter partner ( $\bar{f}$ ) which possesses  
290 the same characteristics as its matter companion but is opposite in electric charge. Thus 12  
291 matter particles are combined with 12 antimatter partners for a total of 24 elementary particles  
292 which form all visible matter in the universe.

293 The interaction between fermions occur via the exchange of spin one particles known as  
294 bosons. Each force is mediated by one or more bosons (Table 2.2). The strong force is mediated  
295 by a set of massless bosons known as the gluons. The weak force is mediated by a neutral  
296 massive boson known as the  $Z$  boson and a pair of charged massive bosons known as the  $W$   
297 bosons. Finally, the elecromagentic force is mediated by a massless boson known as the photon.  
298 Note that each boson has an antimatter partner however some are indistinguishable from their

---

<sup>1</sup>The electric charge is always stated in units of elementary charge  $e$

<sup>299</sup> matter partner. A summary of their properties is shown in Table 2.1.

<sup>300</sup> Each fermion has a set of so-called quantum numbers which dictate the type of interactions  
<sup>301</sup> that can occur. For example each lepton has a lepton number associated with it, electrons have  
<sup>302</sup> an electron lepton number ( $L_e$ ) of +1, while the positron has  $L_e = -1$ . Muons and taus have  
<sup>303</sup> their own respective lepton number ( $L_\mu$  and  $L_\tau$ ). Each neutrino has lepton number  $L_f = 1$  and  
<sup>304</sup> their anti-matter counterpart have  $L_f = -1$ . Each of these lepton numbers is approximately  
<sup>305</sup> conserved separately across interaction vertices. The conservation is only approximate due to  
<sup>306</sup> the non-zero mass of neutrinos. Another example of a quantum number is baryon number ( $B$ ),  
<sup>307</sup> each quark has  $B = \frac{1}{3}$  and anti-quarks have  $B = -\frac{1}{3}$ .

Fermions ( $s = \frac{1}{2}$ )			Bosons ( $s = 0$ )	Higgs ( $s = 1$ )
	I	II	III	
Quarks	$+\frac{2}{3}$ $u$ Up	$+\frac{2}{3}$ $c$ Charm	$+\frac{2}{3}$ $t$ Top	$0$ $\gamma$ Photon (EM)
	$-\frac{1}{3}$ $d$ Down	$-\frac{1}{3}$ $s$ Strange	$-\frac{1}{3}$ $b$ Bottom	$\pm 1$ $W^\pm$ W boson (Weak)
	$-1$ $e$ Electron	$-1$ $\mu$ Muon	$-1$ $\tau$ Tau	$0$ $Z$ Z boson (Weak)
	$0$ $\nu_e$ Electron Neutrino	$0$ $\nu_\mu$ Muon Neutrino	$0$ $\nu_\tau$ Tau Neutrino	$0$ $g$ Gluon (Strong)
				<b>q</b> <b>symbol</b> name (force)
				mass

Table 2.1: A summary of all elementary particles described by the SM [1]. Note the various groupings and divisions including by spin, generation and particle type. For each particle the charge ( $q$ ), mass and name are shown as per the legend on the bottom-right.

Name	Relative Strength	Boson
Strong	$10^{38}$	Gluons
Electromagnetic	$10^{36}$	Photon
Weak	$10^{25}$	$W^\pm$ and $Z^0$
Gravity	1	Graviton*

Table 2.2: A summary of the four fundamental forces ordered by relative strength. These are approximate relative strengths for the purpose of demonstrating the hierarchy of forces as a function of their strength. A more accurate determination of the interaction strength depends on the details of the interaction itself. Note however the order-of-magnitude differences in the relative strengths of these forces. Note that the graviton is the theoretical boson responsible for mediating gravitational interactions, it is not part of the SM.

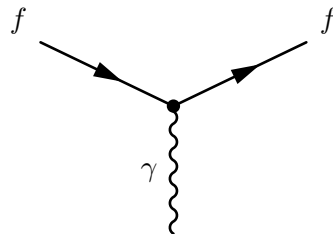


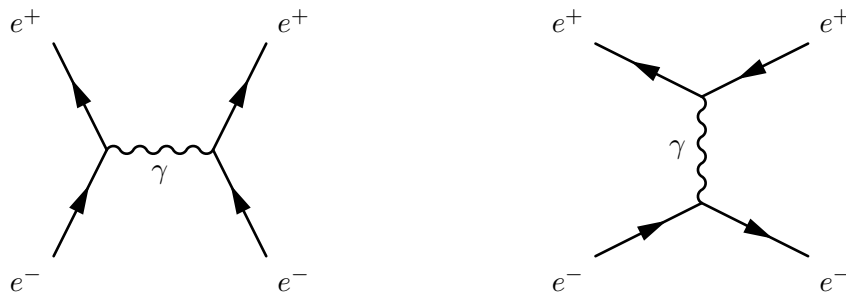
Figure 2.1: The interaction vertex described by QED. One can obtain all possible vertex shapes by rotating this basic vertex and assigning the appropriate electric charge and making sure to conserve lepton number across the vertex.

## 308 2.1 Quantum Electrodynamics

309 The interaction of particles via the electromagnetic force is described by Quantum Electrodynamics or QED. These interactions are mediated by the massless neutral boson known as the 310 photon and the strength of the interaction is characterized by the fine-structure constant  $\alpha$ . All 311 electrically charged fermions are allowed to interact, since the photon itself is not charged, no 312 self-interaction is allowed within QED. Figure 2.1 shows the single vertex described by QED, 313 where two fermions interact via a photon. Note that the electric charge is conserved across the 314 vertex, so for example  $\gamma \rightarrow e^+e^-$  is not allowed within QED.  
315

316 By combining different forms of this vertex one can build every possible QED interaction.  
317 The interaction  $e^+e^- \rightarrow e^+e^-$  is known as Bhabha scattering. Two leading order (LO)<sup>2</sup> dia-  
318 grams contribute to this interaction, annihilation (Figure 2.2a) and scattering (Figure 2.2b).

<sup>2</sup>The simplest diagram with the least vertices



(a) Electron-positron pair annihilation mediated by a photon.  
 (b) Electron-positron pair scattering via the emission of a photon.

Figure 2.2: LO Feynman diagrams of the process  $e^+e^- \rightarrow e^+e^-$  allowed in QED. Additional vertices can be added to produce higher-order diagrams of the same process.

## <sup>319</sup> 2.2 Quantum Chromodynamics

<sup>320</sup> Interactions via the strong force are described in the theory of Quantum Chromodynamics or  
<sup>321</sup> QCD. These interactions are mediated by a set of massless neutral bosons known as gluons.  
<sup>322</sup> QCD introduces the concept of colour, which similarly to electrical charge, determines the  
<sup>323</sup> possible interactions that can occur via the strong force. Colour can take three states, red  
<sup>324</sup> (antired), blue (antiblue), green (antigreen):

$$r = \begin{pmatrix} 1 \\ 0 \\ 0 \end{pmatrix}, \quad g = \begin{pmatrix} 0 \\ 1 \\ 0 \end{pmatrix}, \quad b = \begin{pmatrix} 0 \\ 0 \\ 1 \end{pmatrix} \quad (2.1)$$

$$\bar{r} = \begin{pmatrix} 1 & 0 & 0 \end{pmatrix}, \quad \bar{g} = \begin{pmatrix} 0 & 1 & 0 \end{pmatrix}, \quad \bar{b} = \begin{pmatrix} 0 & 0 & 1 \end{pmatrix} \quad (2.2)$$

Both quarks and gluons possess colour and as a result gluons, unlike photons, can self-interact in a three gluon vertex (Figure 2.3b) or a four gluon vertex (Figure 2.3c). As with electrical charge, colour-charge must also be conserved. Thus in the scattering process  $q \rightarrow q + g$  shown in Figure 2.3a the flavour of the quark may not change but the colour-charge does and the gluon carries away the difference in colour. Thus each gluon has a colour-anticolour charge associated with it. Naively one would expect nine different types of gluon that participate in interaction, owing to the nine possible combinations of colour and anticolour, however the

SU(3) symmetry on which QCD is based results in a colour octet:

$$\begin{array}{ll}
 (r\bar{b} + b\bar{r})/\sqrt{2} & -i(r\bar{g} - g\bar{r})/\sqrt{2} \\
 -i(r\bar{b} - b\bar{r})/\sqrt{2} & (b\bar{g} + g\bar{b})/\sqrt{2} \\
 (r\bar{r} + b\bar{b})/\sqrt{2} & -i(b\bar{g} - g\bar{b})/\sqrt{2} \\
 (r\bar{g} + g\bar{r})/\sqrt{2} & (r\bar{r} + b\bar{b} - 2g\bar{g})/\sqrt{6}
 \end{array}$$

<sup>325</sup> and a “colour singlet”:

$$(r\bar{r} + g\bar{g} + b\bar{b})/\sqrt{3} \quad (2.3)$$

<sup>326</sup> which is overall colourless.

<sup>327</sup> There are then eight different gluons that can participate in QCD interactions each with a  
<sup>328</sup> different colour-charge combination. Additionally there is a ninth combination which is overall  
<sup>329</sup> colorless so it cannot take part in interactions.

<sup>330</sup> In an analogous fashion to screening which occurs with electric charges, quark-antiquark  
<sup>331</sup> pairs act like dipoles which screen the true colour charge of the central quark. However since  
<sup>332</sup> gluons also carry colour, they cause the opposite effect (anti-screening) to amplify and change  
<sup>333</sup> the observed colour of the quark. Which effect wins out depends on the number of colours in  
<sup>334</sup> the theory and the number of quark flavours. As it is with three colour states and six different  
<sup>335</sup> quark flavours, anti-screening is the overall dominant effect. As a result the colour potential  
<sup>336</sup> decreases with distance and quarks experience very little potential when very near to each  
<sup>337</sup> other. This effect is known as asymptotic freedom and results in quarks only existing within  
<sup>338</sup> colorless bound states known as *hadrons*.

<sup>339</sup> Hadrons can be divided into two categories: *mesons*, which contain a quark and an anti-  
<sup>340</sup> quark ( $q\bar{q}$ ); and *baryons* which are made of three quarks (or antiquarks) each with a different  
<sup>341</sup> (anti)colour-charge to result in a colourless composite particle. Common examples of baryons  
<sup>342</sup> are protons ( $uud$ ) and neutrons ( $udd$ ) which are the building blocks of atomic nuclei. While  
<sup>343</sup>  $\pi^0$  ( $u\bar{u}/d\bar{d}$ ) is a commonly produced meson in hadron colliders. Note that due to the quark  
<sup>344</sup> configuration, baryons have baryon number  $B = +1$  while mesons have  $B = 0$ .

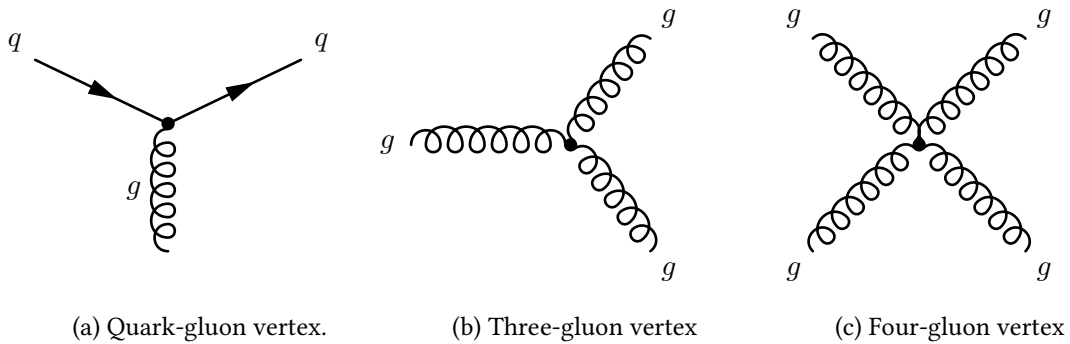


Figure 2.3: Diagrams of the fundamental interaction vertices described by quantum chromodynamics. Shown are (a) Gluon emission from a quark, (b) Gluon emission from a gluon and finally (c) the four-gluon vertex.

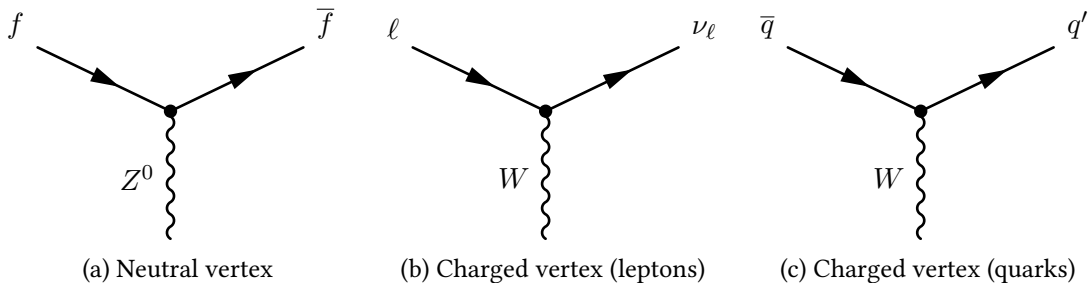


Figure 2.4: The neutral current and charged current vertices allowed via the weak force. Where  $f$  can be an  $e$ ,  $\mu$  or  $\tau$  and  $\nu_\ell$  is the corresponding lepton neutrino of the same flavour. One can obtain all possible interaction vertices by rotating these basic vertices and assigning the appropriate electric charge and making sure to conserve lepton flavour across the vertex.

### 2.3 Weak Interactions

The final type of interaction involves the so-called weak force. The weak force is responsible for  $\beta^-$  decay ( $n \rightarrow p + e^- + \bar{\nu}_e$ ) and  $\beta^+$  decay. Interactions via the weak force are mediated by a single neutral massive boson and two charged massive bosons. Since the bosons responsible for weak interactions are massive, the range of interaction is very short, unlike electromagnetic interactions via a massless photon.

All fermions can take part in interactions via the weak force. Let us consider weak interactions involving only leptons. The weak neutral vertex is very similar to the basic vertex seen in QED (2.1). A valid interaction via the weak force is then formed by combining these simple vertices (Figure 2.4) while taking care to conserve electric charge and lepton flavour. An example of a leptonic weak interaction is muon decay ( $\mu \rightarrow \nu_\mu e^- \bar{\nu}_e$ ) shown in Figure 2.5.

Let us consider weak interactions involving quarks. The neutral vertex is similar to that of

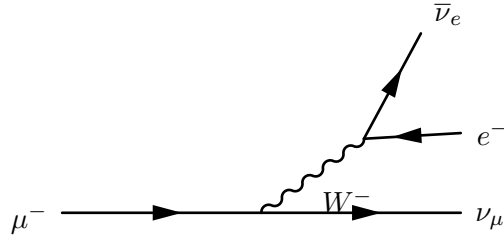


Figure 2.5: Neutral current weak scattering vertex

357 the leptonic version, a quark can emit a  $Z$  boson or a  $Z$  can decay to a quark-antiquark pair.  
 358 The charged current then changes the flavour of an up-type quark into a down-type quark  
 359 (or vice-versa) with a  $W$  boson of the appropriate charge (Figure 2.4c). Weak interactions  
 360 can also change the flavour of a quark across generations. A well-known example of such an  
 361 interaction is Kaon decay ( $K^+ \rightarrow \mu^+ \nu_\mu$ ). In order to account for this interaction and preserve  
 362 the universality of weak interactions, Nicola Cabibbo postulated [12] that the states that couple  
 363 to the charged current are really a mixture of 'rotated' quark states:

$$\begin{pmatrix} u \\ d' \end{pmatrix} \begin{pmatrix} c \\ s' \end{pmatrix} \quad (2.4)$$

364 where

$$d' = d \cos \theta_c + s \sin \theta_c \quad (2.5a)$$

365

$$s' = -d \sin \theta_c + s \cos \theta_c \quad (2.5b)$$

366 This introduces an arbitrary parameter into the theory known as the quark mixing angle  
 367 or the Cabibbo angle  $\theta_c$ . The introduction of quark mixing has the effect of attenuating the  
 368 interaction strength at vertices involving multiple quark generations. Interactions which cross  
 369 one generation are said to be Cabibbo Suppressed while those that cross two generations are  
 370 Doubly Cabibbo suppressed.

371 Taking into account the three quark generations, quark mixing can be expressed in matrix  
 372 notation as shown in Equation 2.6. This unitary matrix is known as the Cabibbo-Kobayashi-  
 373 Maskawa Matrix (CKM Matrix) after Cabibbo which initially postulated quark mixing and  
 374 Makoto Kobayashi and Toshihide Maskawa who later added an additional generation, con-  
 375 taining the top and bottom quarks, to the matrix [13].

$$\begin{pmatrix} d' \\ s' \\ b' \end{pmatrix} = V_{CKM} \begin{pmatrix} d \\ s \\ b \end{pmatrix} = \begin{pmatrix} V_{ud} & V_{us} & V_{ub} \\ V_{cd} & V_{cs} & V_{cb} \\ V_{td} & V_{ts} & V_{tb} \end{pmatrix} \begin{pmatrix} d \\ s \\ b \end{pmatrix} \quad (2.6)$$

376 Several parameterizations of the CKM matrix exist, the Chau-Keung parametrization [14]  
377 uses angles  $\theta_{12}, \theta_{23}, \theta_{13}$  and a phase  $\delta_{13}$ :

$$V_{CKM} = \begin{pmatrix} c_{12}c_{13} & s_{12}c_{13} & s_{13}\exp(-i\delta) \\ -s_{12}c_{23} - c_{12}s_{23}s_{13}\exp(i\delta) & c_{12}c_{23} - s_{12}s_{23}s_{13}\exp(i\delta) & s_{23}c_{13} \\ s_{12}s_{23} - c_{12}c_{23}s_{13}\exp(i\delta) & -c_{12}s_{23} - s_{12}c_{23}s_{13}\exp(i\delta) & c_{23}c_{13} \end{pmatrix} \quad (2.7)$$

378 where  $c_{ij} = \cos \theta_{ij}$  and  $s_{ij} = \sin \theta_{ij}$  for  $i=1,2,3$ . This parametrization has the advantage that  
379 each angle  $\theta_{ij}$  relates to a specific transition from one generation to the other. If  $\theta_{13} = \theta_{23} = 0$   
380 the third generation is not coupled to the other two and the matrix reduces to the original  
381 matrix postulated by Cabibbo. Note that  $\theta_{12}$  is the Cabibbo angle,  $\theta_c$ , described earlier.

382 Another parameterization due to Wolfenstein [15] expresses all elements in terms of the  
383 Cabibbo angle by defining  $\lambda \equiv s_{12} = \sin \theta_{12}$  and then expressing the other elements in terms  
384 of powers of  $\lambda$ :

$$V_{CKM} \approx \begin{pmatrix} 1 - \lambda^2/2 & \lambda & A\lambda^3(\rho - i\eta) \\ -\lambda & 1 - \lambda^2/2 & A\lambda^2 \\ A\lambda^3(1 - \rho - i\eta) & -A\lambda^2 & 1 \end{pmatrix} \quad (2.8)$$

385 where  $A, \rho$  and  $\eta$  are all real numbers intended to express the order of magnitude differences  
386 between  $s_{12}$  and the other elements in the matrix. Of course, all the elements should be the  
387 same irrespective of which parametrization is used.

388 The elements of the CKM matrix have been measured and the latest accepted results are  
389 summarized in 2.10 [1]. The interaction strength is then proportional to  $|V_{ij}|^2$ . Unitarity of the  
390 CKM implies that the probability of transition from any up-type quark to any down-type is the  
391 same,

$$\sum_k |V_{ik}|^2 = \sum_i |V_{ik}|^2 = 1 \quad (2.9)$$

392 for all  $i$  quark generations [16]. The term  $V_{tb}$  is approximately unity and by far dominates  
 393 over the other  $V_{tj}$  terms. This means that the top-quark transitions almost exclusively into a  
 394  $b$ -quark ( $t \rightarrow Wb$ ) with transitions  $t \rightarrow Ws$  and  $t \rightarrow Wd$  having a probability of less than 1%.  
 395 The soft muon tagger which is the focus of this thesis relies on weak semileptonic decays of  
 396  $b$ -quarks. From 2.10 one can see that the transition  $b \rightarrow c$  dominates over  $b \rightarrow u$ . Additionally  
 397 the focus of this thesis is on semileptonic  $t\bar{t}$  events, where one of the  $W$  bosons in the event  
 398 decays to quarks as per the magnitude of  $V_{ij}$ .

$$V_{CKM} = \begin{pmatrix} 0.97427 \pm 0.00015 & 0.22534 \pm 0.00065 & 0.00351^{+0.00015}_{-0.00014} \\ 0.22520 \pm 0.00065 & 0.97344 \pm 0.00016 & 0.0412^{+0.0011}_{-0.0005} \\ 0.00867^{+0.00029}_{-0.00031} & 0.0404^{+0.0011}_{-0.0005} & 0.999146^{+0.000021}_{-0.000046} \end{pmatrix} \quad (2.10)$$

399 An additional unique feature of weak interactions is that the charge conjugation-parity  
 400 ( $CP$ ) symmetry is violated. The operator  $C$  denotes the change of a particle by its antiparticle  
 401 partner and  $P$  denotes a reversal of helicity (the projection of spin onto the momentum of  
 402 a particle). A clear violation of  $C$  and  $P$  was observed in the radioactive decay of Cobalt-  
 403 60, where the resulting electrons were preferentially emitted in the opposite direction of the  
 404 nuclear spin of the Cobalt [17]. Thus weak currents only couple to left-handed neutrinos (or  
 405 right-handed antineutrinos) which is a violation of parity. Additionally charge symmetry is also  
 406 violated since a left-handed neutrino is preferentially picked over a left-handed antineutrino.  
 407 Finally in 1964  $CP$  violation was observed in the decay of neutral kaon [18].

408 Thus the probability of  $\bar{a} \rightarrow \bar{b}$  is not equal to that of  $a \rightarrow b$ . The existence of  $CP$  violation  
 409 has interesting consequences for the formation of the early universe. The preferential produc-  
 410 tion of matter over antimatter in  $CP$  violating interactions would shift the balance in favour of  
 411 matter resulting in a universe similar to our own. In terms of the Wolfenstein parameterization  
 412 of the CKM matrix, if  $\eta = 0$  there is no  $CP$  violation.

413 Finally as with QCD, weak interactions couple weak bosons to each other. Thus the vertex  
 414  $Z \rightarrow W^- W^+$  is allowed via the weak force.

### 415 2.3.1 Electroweak Unification and the Higgs mechanism

416 The unification of the electromagnetic and weak theories was first proposed by Glashow and  
 417 later developed by Weinberg and Salam into the electroweak theory [19–21]. The theory pos-  
 418 tulates that while at low energies the two forces are to be treated separately, at higher the  
 419 two can be seen as a single force. Thus the two forces are different manifestation of the same  
 420 “electroweak” interaction. There were several stumbling blocks to the unification of the forces.  
 421 Firstly, the boson which drives the electromagnetic interaction, the photon, is massless while  
 422 the weak bosons are both massive. Evidence for the massive nature of these bosons has been  
 423 established by experimental results from the UA1 experiment at CERN [22].

424 Thus the symmetry of the theory must be spontaneously broken in some way. A mechanism  
 425 for electroweak symmetry breaking (EWSB) was postulated by Higgs, Brout, Englert and others  
 426 which introduces masses to the weak bosons and posits the existence of an additional scalar  
 427 (spin  $S = 0$ ) boson known as the Higgs boson.

### 428 Gauge Theories

429 Gauge invariance is one of the underlying invariances which underpins the Standard Model.  
 430 Given the so-called Dirac lagrangian<sup>3</sup>

$$\mathcal{L} = i\hbar c\bar{\psi}\gamma^\mu\partial_\mu\psi - mc^2\bar{\psi}\psi \quad (2.11)$$

431 which describes a free particle of spin- $\frac{1}{2}$  with mass  $m$  [11]. Note that it is invariant under the  
 432 transformation

$$\psi \rightarrow e^{i\theta}\psi, \text{ where } \theta \text{ is a real number} \quad (2.12)$$

433 since the adjoint  $\bar{\psi} \rightarrow e^{-i\theta}\bar{\psi}$  and the two terms cancel out. This is known as a *(global) gauge*  
 434 *transformation* since  $\theta$  is the same at all points of space-time. A *(local) gauge transformation*  
 435 occurs when the phase is different for different points in space-time:

$$\psi \rightarrow e^{i\theta(x)}\psi \quad (2.13)$$

---

<sup>3</sup>A Lagrangian is a mathematical function that describes the underlying dynamics of a system as a function of time and space coordinates ( $x^\mu$ ) and their time derivatives.

436     The Dirac lagrangian (Equation 2.11) is not invariant under a local gauge transformation  
 437    since extra terms are created by the derivative. This then implies that the underlying physics of  
 438    such a theory depends on position in space-time. Thus local gauge invariance must be imposed.  
 439    In the case of the Dirac lagrangian, this is done by introducing additional terms to the Dirac  
 440    lagrangian which will cancel the extra terms introduced by the local gauge transformation. As  
 441    it turns out this results in the introduction of a new massless vector field that couples to  $\psi$ .

442     The new lagrangian then describes a spin- $\frac{1}{2}$  particle with mass  $m$  that interacts with a  
 443    free massless field. This new field can be identified as the electromagnetic field and the spin- $\frac{1}{2}$   
 444    particles are electrons and positrons. Thus the resulting lagrangian describes all interactions  
 445    that form part of quantum electrodynamics.

446     A similar procedure can be applied to the color quark model and obtain a description of  
 447    all QCD interactions. However requiring that the weak theory be a gauge theory (invariant  
 448    under local gauge transformation) encounters a problem since the weak bosons are known to  
 449    be massive. There must be some mechanism via which the  $W^\pm$  and  $Z^0$  obtain mass.

450     The Higgs mechanism posits the existence of a complex scalar field doublet that when  
 451    introduced into the electroweak Lagrangian results in the weak fields acquiring a mass term.  
 452    In other words the  $W^\pm$  and  $Z^0$  interact with the Higgs field and obtain a mass. An additional  
 453    consequence of introducing the Higgs field is the inclusion of a scalar boson particle, the the so-  
 454    called “Higgs boson”. Finally the Higgs field also couples to fermions via the Yukawa coupling  
 455    generating gauge invariant mass terms for the fermions as well.<sup>4</sup>.

456     The SM Lagrangian in its current form including the Higgs potential is shown in Equa-  
 457    tion 2.14. This expression describes all possible particle interactions that form part of the SM,  
 458    of particular interest are the fermion mass term which couples the fermion field ( $\psi$ ) to the  
 459    scalar Higgs field ( $\phi$ ) and the Higgs kinetic and potential terms.

---

<sup>4</sup>For a more complete description of the mathematical procedure see [11].

$$\begin{aligned}
\mathcal{L} = & - \underbrace{\frac{1}{4} W_{\mu\nu}^a W^{\mu\nu a}}_{\text{Weak Field}} - \underbrace{\frac{1}{4} B_{\mu\nu} B^{\mu\nu}}_{\text{EM Field}} - \underbrace{\frac{1}{4} G_{\mu\nu}^a G^{\mu\nu a}}_{\text{Strong Field}} \\
& + \underbrace{\bar{\psi} \not{D}_\mu \psi}_{\text{Fermion Kinetic}} + \underbrace{\lambda \bar{\psi} \psi \phi}_{\text{Fermion Mass}} \\
& + \underbrace{|D_\mu \phi|^2}_{\text{Higgs Kinetic}} - \underbrace{V(\phi)}_{\text{Higgs Potential}}
\end{aligned} \tag{2.14}$$

460 **Chapter 3**

461 **Top-quark physics**

462 The third generation of quarks was first proposed by Kobayashi and Maskawa in a paper pub-  
463 lished in 1973 [13] as a way to explain the  $CP$  violation observed in Kaon decays. The existence  
464 of the third generation was confirmed when the lighter of the two constituents, the  $b$  quark,  
465 was discovered in 1977 [23].

466 Due to its large mass, direct confirmation of the existence of the top quark required the  
467 construction of very powerful accelerators. The top quark was discovered by the CDF and D0  
468 experiments at Fermilab in 1995 [24, 25] and then observed at CERN in 2010 [26, 27].

469 The large mass of the top quark makes it a very interesting object of study. The current  
470 world average for the mass of the top quark is

$$m_t = 173.07 \pm 0.52(\text{stat.}) \pm 0.72(\text{syst.}) \text{ GeV} \quad (3.1)$$

471 based on results from Tevatron and the LHC [1].

472 Due to its mass the top quark has an extremely short lifetime  $\tau \approx 0.5 \times 10^{-24}$  s, too short to  
473 interact via the strong force and hadronize into a bound state [28]. Instead the top quark decays  
474 weakly producing a  $W$  boson and a  $b$  quark almost exclusively. This allows experimentalist  
475 to directly study the properties of a bare quark. An impossibility with the other quarks which  
476 bind with other quarks to form hadrons. Measurement of top quark properties (mass, charge,  
477 forward-backward asymmetry, couplings, etc...) forms a large part of high energy physics  
478 research. Measurement of these properties provide rigorous tests of the SM, point towards the  
479 existence of new physics or exclude some BSM theories.

480 From an experimental perspective, top quark decays can produce a very interesting sig-  
 481 nature which includes leptons, jets and transverse missing energy  $\cancel{E}_T$  due to the escaping  
 482 neutrino<sup>1</sup>. The study of top quark decays relies on all parts of a general purpose detector such  
 483 as ATLAS or CMS. In additional  $t\bar{t}$  pair production constitutes a background for many other  
 484 SM and BSM searches, as such understanding this process well is fundamental for almost all  
 485 areas of HEP research.

486 **3.1 Top quark production**

487 Top quarks can be produced in two manners, single top production and  $t\bar{t}$  pair production. In  
 488 the SM, the dominant top quark pair production mechanism proceeds via the strong force. The  
 489 production cross-section of  $pp \rightarrow t\bar{t}$  depends on the mass of the top  $m_t$ , the centre-of-mass  
 490 energy  $s = 4E_{beam}^2$  and the fraction of the momentum taken by the partons<sup>2</sup> of the colliding  
 491 protons.

492 In order to produce a  $t\bar{t}$  pair the total energy carried by the interacting partons must be  
 493 larger than twice the mass of the top. Let us define the effective centre of mass energy  $\hat{s}$   
 494 which reflects the true amount of energy available for interaction. Given two colliding partons,  
 495 denoted  $i$  and  $j$  carrying  $x_i$  and  $x_j$  fractions of the centre of mass energy  $\sqrt{s}$ , then

$$\hat{s} = x_i \sqrt{s} x_j \sqrt{s} = x_i x_j s \quad (3.2)$$

496 assuming that both partons carry the same fraction of the total energy, i.e.  $x_i \approx x_j$  then the  
 497 minimum value of  $x$  required for  $t\bar{t}$  production is

$$x \approx \frac{2m_t}{\sqrt{s}} \quad (3.3)$$

498 At the LHC the minimum threshold at  $\sqrt{s} = 7(14)\text{TeV}$  is approximately 0.05(0.025). At  
 499 such low values of  $x$  the fraction of proton momentum carried by the gluons is large [29] and  
 500 thus gluon fusion interactions dominate. Gluon fusion processes represent 80(90)% of the  
 501 total cross section at  $\sqrt{s} = 7(14)\text{TeV}$ , with the remainder contribution coming from quark

---

<sup>1</sup>Neutrinos do not interact with the detector material and thus escape without being detected, missing energy is described in more detail in Chapter 4

<sup>2</sup>Constituents of the hadrons, so quarks and gluons

pair annihilation. The feynman diagrams for these interactions are shown in Figure 3.1. The theoretical inclusive  $t\bar{t}$  production cross section at the LHC has been calculated at next-to-next-to-leading order (NNLO) to be  $\sigma(t\bar{t}) = 158^{-12.2}_{+13.5} \text{ pb}$  [30] at  $\sqrt{s} = 7\text{TeV}$  and at next-to-leading order (NLO)  $246 \pm 10 \text{ pb}$  for  $\sqrt{s} = 8\text{TeV}$ .

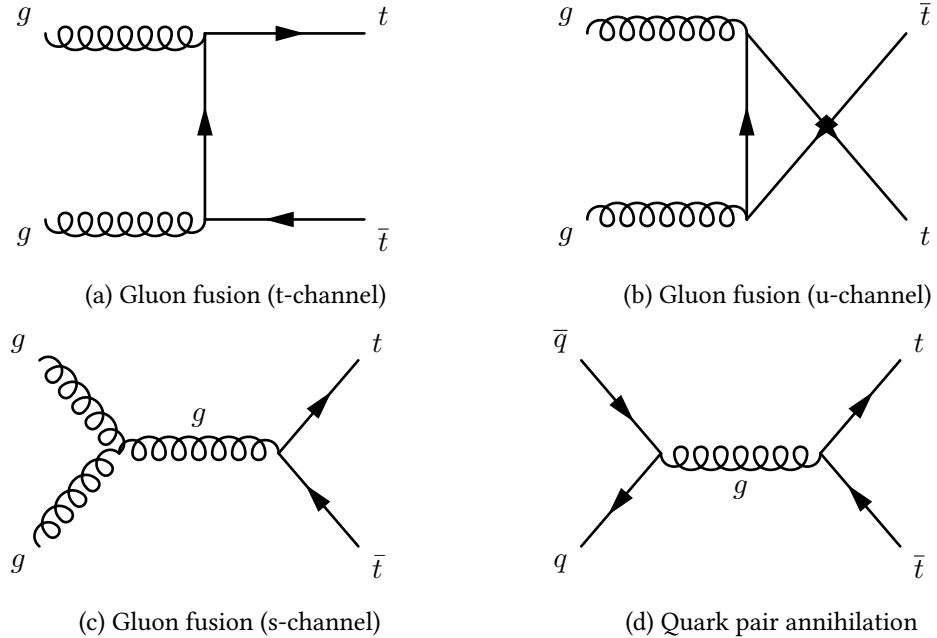


Figure 3.1: The leading order Feynman diagrams for  $t\bar{t}$  production.

Single top production occurs via the weak force almost exclusively through the  $Wtb$  vertex since  $|V_{tb}| \gg |V_{ts}|, |V_{td}|$ . At LO there are several production mechanisms for single-top events:

- Weak quark-antiquark annihilation forming a  $W$  which subsequently decays into a  $t\bar{b}$  (Figure 3.2a).
- The so-called  $tW$  production, where a  $b$  quark absorbs a gluon and decays to a  $t$  and  $W$  (Figure 3.2b).
- $b$  quark scattering off a  $W$  boson, where the  $b$  comes from gluon splitting (Figure 3.2c) or from the proton (Figure 3.2d).

As top quark pair production can proceed via the strong force it occurs overwhelmingly more often than single top production. The inclusive cross-sections for  $pp \rightarrow t\bar{t}$  and  $pp \rightarrow t+X$

<sup>516</sup> at the LHC have been estimated at NLO [2, 3]. As can be seen from Table 3.1 the production cross section of  $t\bar{t}$  is approximately two times larger than the single-top cross-section.

Process	$\sqrt{s} = 7\text{TeV}$	$\sqrt{s} = 8\text{TeV}$
Single top $\sigma(t\text{-chan}) [\text{pb}]$	$66 \pm 2$	$87 \pm 3$
Single top $\sigma(Wt) [\text{pb}]$	$15.6 \pm 1.2$	$22.2 \pm 1.5$

Table 3.1: Summary of the predicted SM single top production [2] and top pair production [3] cross sections at the LHC for  $\sqrt{s}=7$  and 8 TeV.

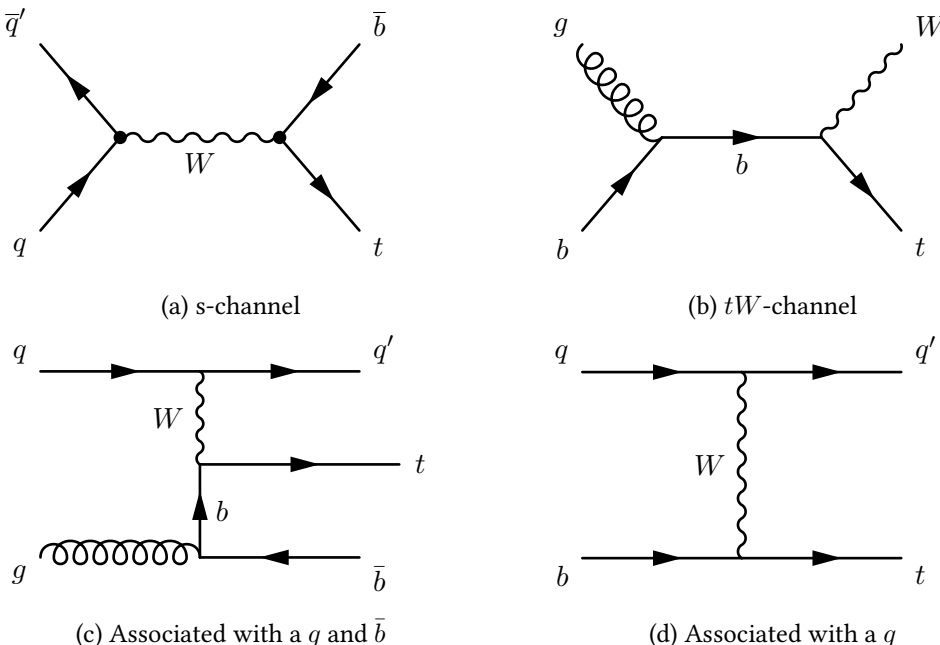


Figure 3.2: Example Feynman diagrams for single top quark at leading order.

<sup>517</sup>

## 3.2 Top quark decay modes

<sup>519</sup> The top quark decays almost exclusively into a  $W$  boson and a  $b$ -quark. The ratio of branching <sup>520</sup> ratios  $\Gamma(t \rightarrow Wb)/\Gamma(t \rightarrow Wq(q = b, s, d))$  is  $0.91 \pm 0.04$  [1].

<sup>521</sup> As the LHC collides proton-proton beams, the overwhelming majority of events produced <sup>522</sup> will feature multiple hadronic *jets*, a stream of particles resulting from the hadronization of <sup>523</sup> quarks in the detector, most of which will originate from “light” quarks<sup>3</sup>. Unlike light hadrons,

<sup>3</sup>The term light quarks usually refers to quarks in the first two generations. Light jets are those originating from those quarks

Decay	Branching ratio
$W \rightarrow e + \nu$	$(10.75 \pm 0.13)\%$
$W \rightarrow \mu + \nu$	$(10.57 \pm 0.15)\%$
$W \rightarrow \tau + \nu$	$(11.25 \pm 0.20)\%$
hadrons	$(67.60 \pm 0.27)\%$

Table 3.2: Branching ratios for the decay of  $W$  boson. Note that “hadrons” refers to a possible combination of  $q\bar{q}'$  where  $\bar{q}'$  denotes the antiquark of a flavour different to that of the first quark. [1]

524     *B* hadrons have a sufficiently large lifetime that they travel a certain distance within a before  
 525     deacying. Additional features such as the semi-leptonic decay of  $b$  quarks can be exploited to  
 526     determine the presence of such a quark in the detector. Collectively analysis techniques that  
 527     permit the detection of  $b$ -jets are known as *b-tagging*. Top quark events will produce two  $b$   
 528     quarks, making b-tagging techniques a central part of any  $t\bar{t}$  analysis.

529     The other part of the top decay, the  $W$  boson is used to classify  $t\bar{t}$  events. As discussed  
 530     in Section 2,  $W$  bosons can decay leptonically ( $\ell\nu_\ell$ ) or hadronically ( $W \rightarrow q\bar{q}'$ ) driven by the  
 531     CKM vertex element, since  $\Gamma \propto |V_{ij}|^2$ . The various branching ratios of  $W$  decays are presented  
 532     in Table 3.2.

533     Thus  $t\bar{t}$  events are labelled as “dilepton”, “all-hadronic” or “lepton + jets” depending on  
 534     the combination of  $W$  decays present. The probability for  $t\bar{t}$  event to be of a given type is  
 535     dependent on the branching-ratios of  $W$  decays shown a priori. As can be seen from Figure 3.3  
 536     the all-hadronic events dominate, followed by the lepton plus jets and dilepton. Each of these  
 537     types requires a very different analysis approach due to their distinct backgrounds, branching-  
 538     ratio, detector signature and reconstruction requirements.

539     The all-hadronic final state includes four light quarks which will hadronize to form four  
 540     Light Flavour (LF) jets and two  $b$  quarks leading to two  $b$  jets. Due to the large hadronic activity  
 541     the all-hadronic channel is very challenging. As mentioned before, hadronic collisions produce  
 542     events with a large number of quarks – and thus jets – in the final state. The background to the  
 543     all-hadronic channel are therefore very high. As shown in Figure 3.3, the all-hadronic channel  
 544     has the largest branching ratio of the three.

545     The dilepton final state includes two leptons, large  $\cancel{E}_T$  from two neutrinos which escape  
 546     the detector and two  $b$  jets. In contrast to the all-hadronic channel, dilepton events are very  
 547     clean due to the presence of leptons and  $\cancel{E}_T$ , however the branching ratio is very small and

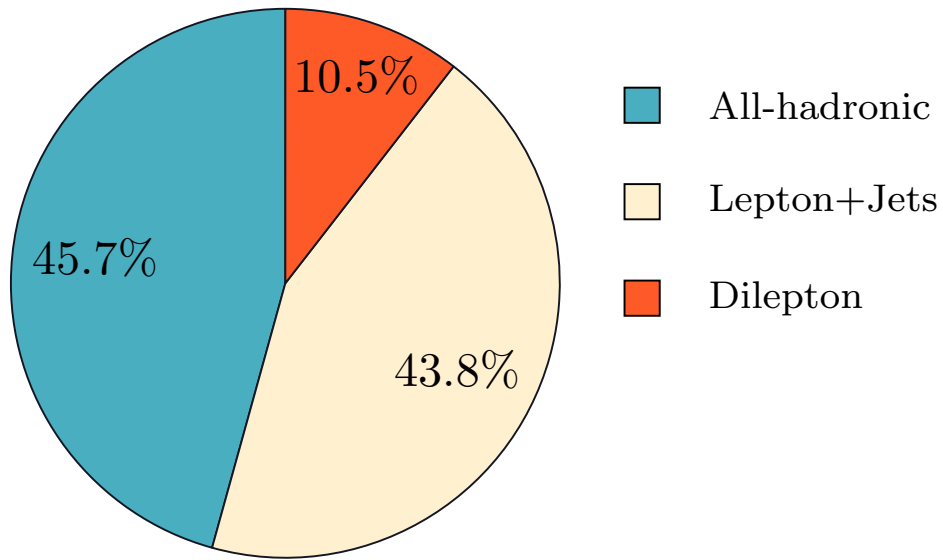


Figure 3.3: Branching ratios of all possible  $t\bar{t}$  decays. These probabilities are based on the branching-ratios of  $W$  decay shown in Table 3.2.

reconstruction of the top is challenging due to the presence of two neutrinos which escape the detector without interacting.

Finally, the lepton plus jets channel has a large branching ratio while having a distinct signature with a lepton and  $\cancel{E}_T$  as well as LF and  $b$  jets. Lepton plus jets analyses usually do not directly include  $\tau$  leptons as the signal lepton. The  $\tau$  lepton is unstable and decays primarily via the weak force producing hadrons in the final state. The reconstruction of  $\tau$  leptons is a complex task and  $\tau$  plus jet events are treated separately within dedicated analyses. An example of the full lepton plus jets chain is shown in Figure 3.5.

The lepton plus jets channel has the advantage of a more distinct signature than the all-hadronic event as well as a suffering from less background. Additionally the branching ratio of lepton plus jets event is approximately twice that of the dilepton channel. As a result the lepton plus jets channel has been chosen as the focus of this thesis.

### 3.3 Latest developments in top physics

This section discusses a few of the latest measurements in the area of top quark pair production with a focus on LHC results. As discussed top quark decays provide the only probe to study

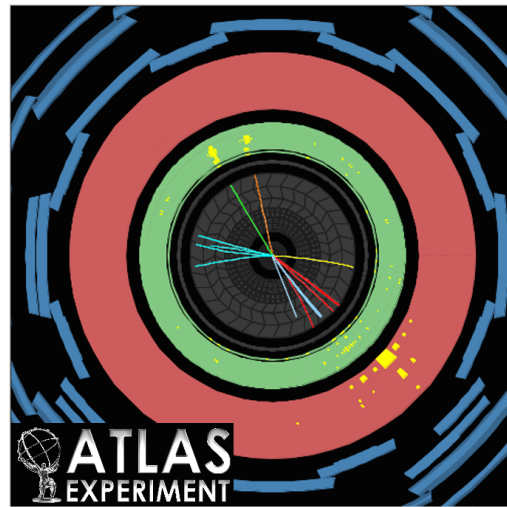


Figure 3.4: Example event display of a dilepton  $t\bar{t}$  event recorded by ATLAS.

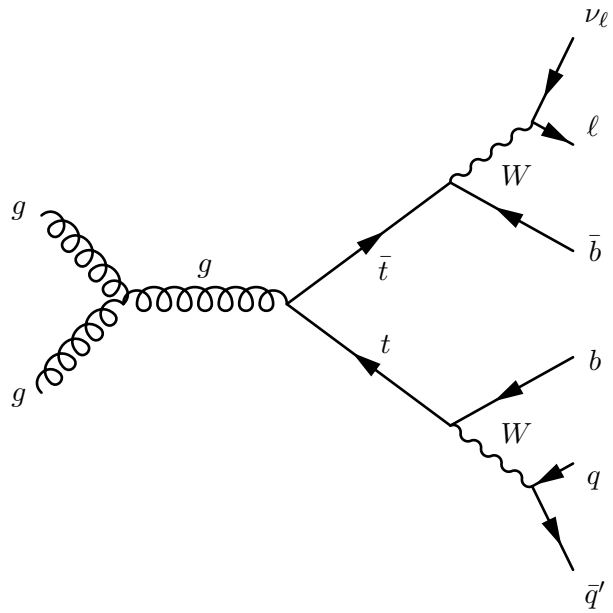


Figure 3.5: The feynman diagram of lepton plus jets channel including  $t\bar{t}$  production via gluon fusion and decay with a leptonically decaying  $W^+$ . Note that all other production mechanisms are also considered and the final state where the  $W^-$  is decayed leptonically is also taken into account.

563 the properties of a bare quark. Measurements of its properties provide a stringent test of the  
 564 SM and could show hints of new physics from BSM theories. Moreover, due to its final state  
 565 signature, top quark pair production, particularly in the lepton + jets channel, form the back-  
 566 ground to many searches for new physics. Additionally all parts of the detector are utilized  
 567 in the reconstruction of  $\ell$ +jets events and as such it is possible to use these events to tune or  
 568 *calibrate* many analysis and reconstruction techniques.

569 **Cross-section measurement**

570 Measurement of the cross-section of the top quark is a benchmark test of the SM. Any statisti-  
 571 cally significant deviation from the predicted value could point to the presence of new physics.  
 572 Some BSM theories posit the existence of particles which could decay to produce a  $t\bar{t}$  pair. If  
 573 such theory is correct this would be observed in an increase in the cross section measured away  
 574 from the predicted SM value.

575 Experimentally measurement of the cross-section is vital when attempting to reduce and  
 576 estimate the amount of top quark background present in other analyses. Searches for the Higgs  
 577 boson exploit many different channels such as  $t\bar{t}H \rightarrow t\bar{t}b\bar{b}$  which have  $t\bar{t}$  events as a back-  
 578 ground. The type of events predicted by the BSM theory, Supersymmetry (SUSY) include a  
 579 large amount of  $\cancel{E}_T$ , leptons and jets in the final state. Top quark pair events mimick these  
 580 processes and constitute a large background.

581 A summary of all  $t\bar{t}$  cross section measurements from the LHC is shown in Figure 3.6 and  
 582 a comparison against the Tevatron measurement at  $\sqrt{s} = 1.96$  TeV is shown in Figure 3.7.

583 **Top mass measurement**

584 The mass of the top  $m_t$  is a fundamental parameter of the SM. Make sure to fill this in!!!

585 **Mass asymmetry measurement**

586 As discussed, in Section 2.3, the charge ( $C$ ) and parity ( $P$ ) symmetries are both violated in weak  
 587 interactions. The CPT symmetry which includes time reversal ( $T$ ) is the last remaining sym-  
 588 metry which no interaction appears to violate. Any deviations from this symmetry would have  
 589 major implications on particles physics [31] and could manifest itself as differences between

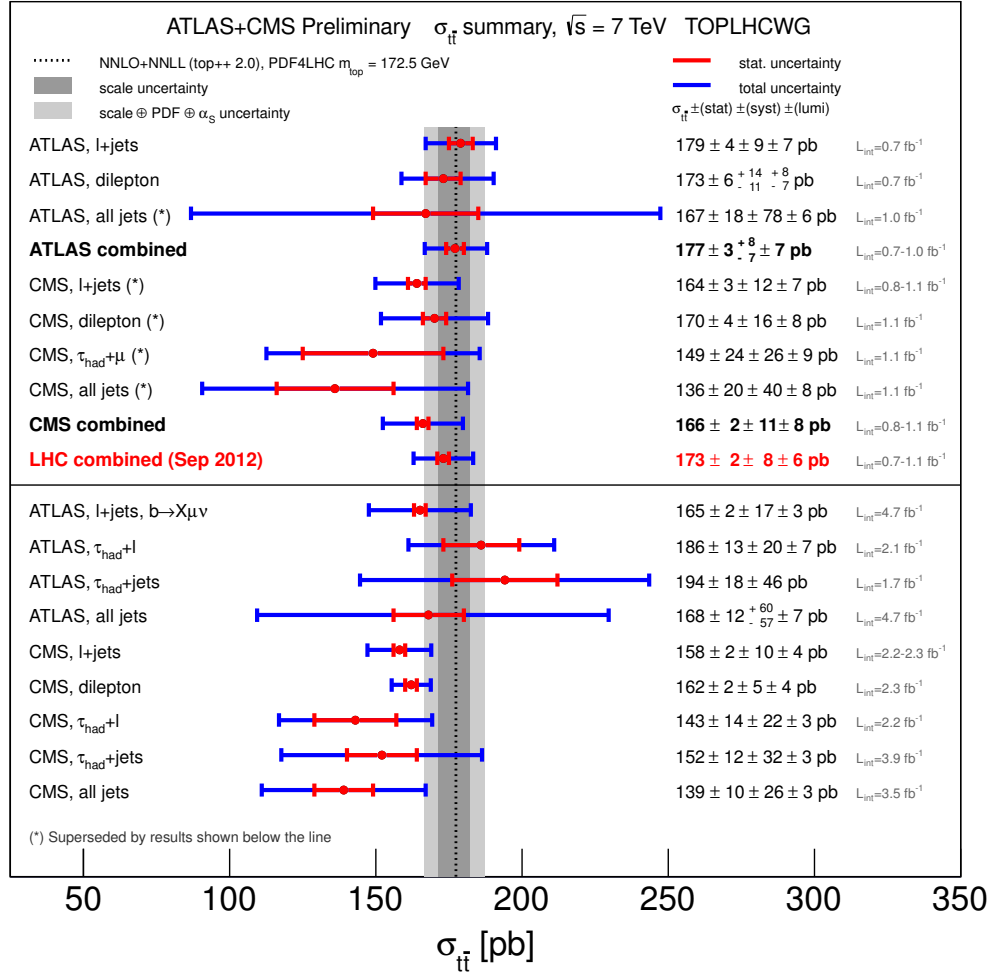


Figure 3.6: A summary of all  $t\bar{t}$  production cross section measurements performed at the LHC at  $\sqrt{s} = 7 \text{ TeV}$ . Note the theory prediction shown as a dotted black line with its associated uncertainties as grey bands. The results shown above the black line have been statistically combined, producing the results labelled as **combined**. Many of these analyses have been superseded and the results are shown below the line. Other analyses performed but not included in the combination are also shown below the line.

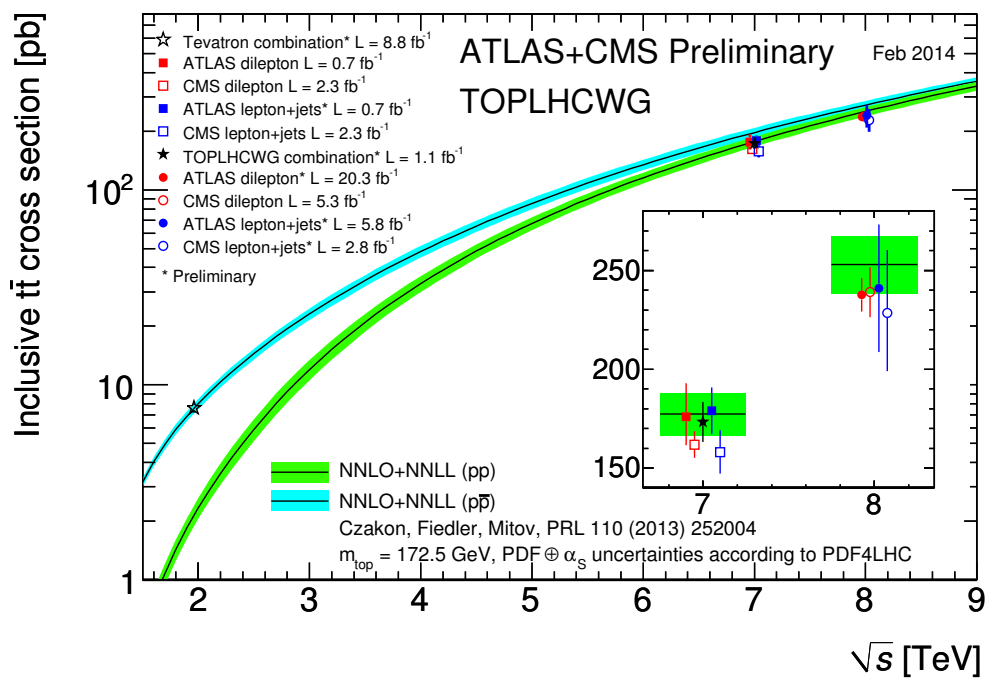


Figure 3.7: A summary of the most precise  $t\bar{t}$  production cross section measurements performed at the LHC at  $\sqrt{s} = 7$  and 8 TeV and the Tevatron at  $\sqrt{s} = 1.96$  TeV compared to the theoretical prediction. Note that the Tevatron results should be compared against the prediction for  $p\bar{p}$  collisions while the LHC against the  $pp$  collision predictions.

590 matter and antimatter particles. As the only quark which can be studied directly, measurement  
591 of  $\Delta m \equiv m_t - m_{\bar{t}}$  could hint at any such deviation produced by new physics. Such a  
592 measurement was conducted by the ATLAS [32] experiment yielding the result:

$$\Delta m_t = -0.44 \pm 0.46(\text{stat.}) \pm 0.27(\text{syst.}) \text{ GeV} \quad (3.4)$$

593 and by the CMS [33] experiment yielding the result:

$$\Delta m_t = 0.67 \pm 0.61(\text{stat.}) \pm 0.41(\text{syst.}) \text{ GeV} \quad (3.5)$$

594 which are both consistent with the SM prediction and imply CPT invariance.

595 **Boosted top searches**

596 **Chapter 4**

597 **The LHC and the ATLAS Detector**

598 **4.1 The Large Hadron Collider**

599 The Large Hadron Collider (LHC) [34] is a proton ring collider located at the European Centre  
600 for Nuclear Research (CERN). The main LHC ring is housed in the tunnel which previously  
601 contained the Large Electron-Positron collider. The LHC ring is 27 km in circumference and  
602 located approximately 175 m underground. The LHC services four different experiments lo-  
603 cated at four interaction points around the beam-pipe (Figure 4.1). A toroidal LHC apparatus  
604 (ATLAS, the experiment used for this thesis), the compact muon solenoid (CMS), a large ion  
605 collider (ALICE) experiment and the LHC beauty (LHCb) experiment.

606 ATLAS and CMS are general purpose detectors designed to support a varied physics pro-  
607 gramme, from SM physics like top quark measurements to BSM searches such as supersym-  
608 metry. ALICE and LHCb are more specialized experiments which focus on heavy ions and  $b$   
609 physics, respectively.

610 The LHC accelerates two beams of protons in opposite directions and then collides the two  
611 beams at the four interaction points where the experiments are located. The protons come  
612 from hydrogen gas where the orbiting electron is removed by an electric field, leaving behind  
613 a bare proton. The beam acceleration occurs in several stages exploiting smaller experiments  
614 present at CERN. During 2010 and 2011 protons were accelerated to a beam energy of 3.5 TeV,  
615 creating a centre-of-mass energy of 7 TeV and then 4 TeV per beam in 2012 for a centre-of-  
616 mass energy of 8 TeV. Each beam is made of multiple bunches of protons, with as many as  
617 hundreds of billions of protons in each bunch. Bunches are grouped into *bunch trains* with a

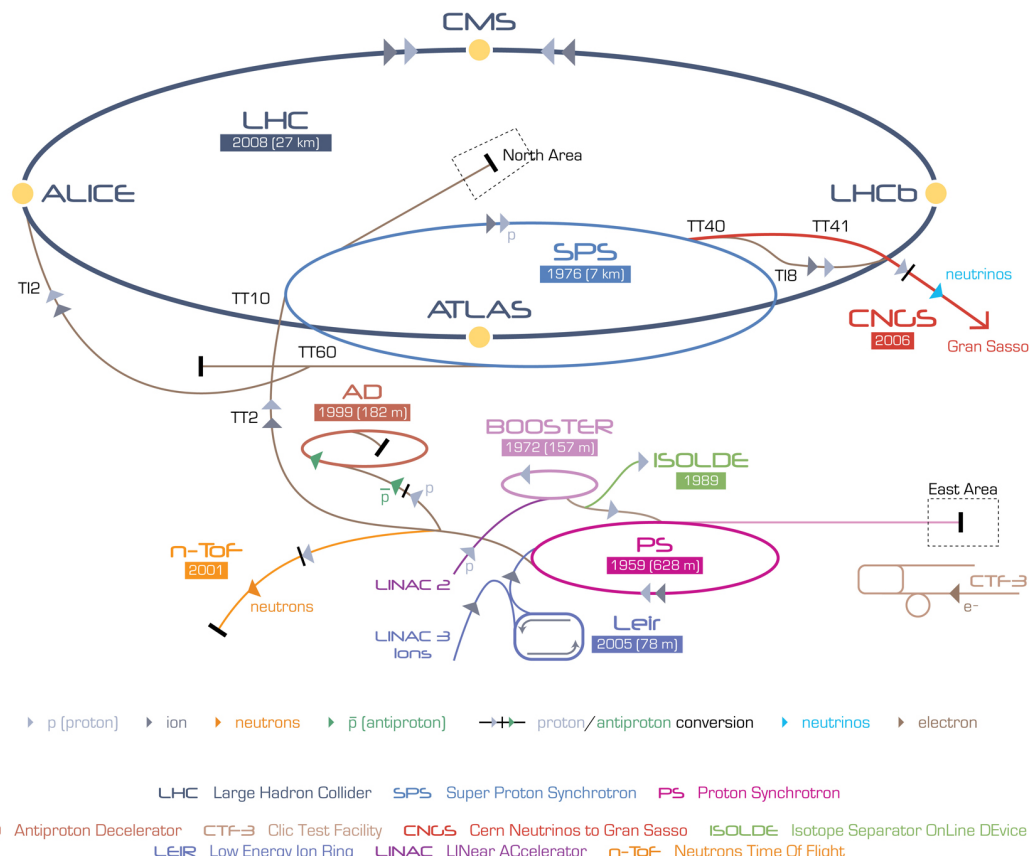
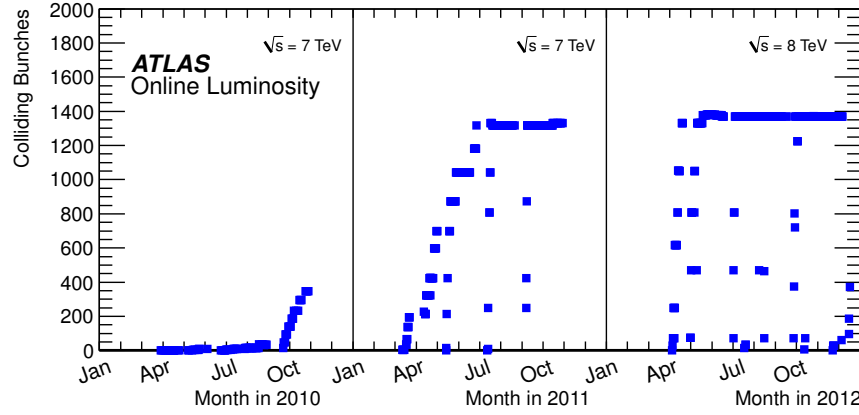
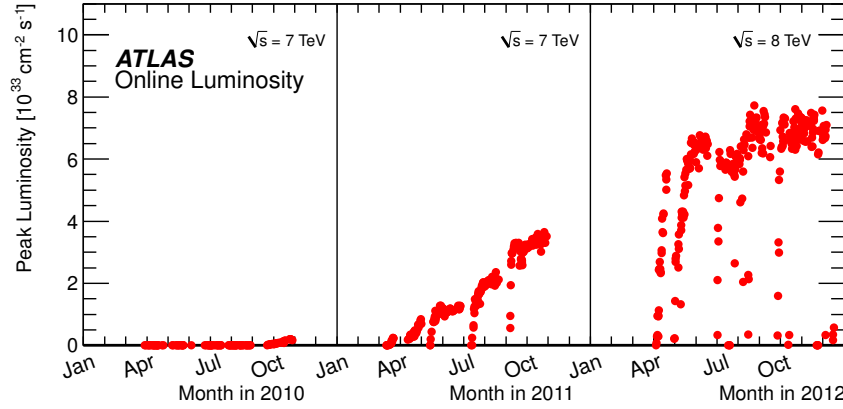


Figure 4.1: The layout of CERN complex of experiments, note the main four LHC experiments located at different points around the ring.

618 designed *bunch spacing* of 25 ns between each of the bunches that compose a single train. Note  
 619 that the bunch spacing and size of the bunch can be altered to adjust the amount of collisions  
 620 and the time between collisions. The variation in the number of colliding bunches is shown in  
 621 Figure 4.2a.



(a) The number of bunches colliding per unit time at the LHC for the 2010, 2011 and 2012  $pp$  collision periods.



(b) The peak luminosity per unit time at the LHC for the 2010, 2011 and 2012  $pp$  collision periods.

Figure 4.2: Shown in (a) is the number of bunches colliding at the LHC and (b) the peak luminosity per unit time.

622 The acceleration of the proton beams occurs in several stages, within several different ac-  
 623 celerators. The beams are first accelerated in a linear collider (LINAC 2) to an energy of 50 MeV  
 624 before being injected into the proton synchotron booster (PSB). The beams are then boosted  
 625 to 1.4 GeV by a varying magnetic field in the circular PSB. The beams are then passed into the  
 626 proton synchrotron (PS) and then the super proton syncrotron (SPS) where the beam energy  
 627 increases to 26 GeV and then 450 GeV. At this stage the beam is injected into the LHC and

628 then accelerated to the final desired energy. The design energy is 7 TeV per beam for a total  
 629 of 14 GeV centre-of-mass energy. From injection of the protons into LINAC 2 to stable beam  
 630 conditions in the LHC, the whole process can take a couple of hours.

631 As bunches overlap the protons that make up the bunches interact, these interactions are  
 632 known as events. The number of events is proportional to the instantaneous luminosity  $\mathcal{L}$  of  
 633 the collider.  $\mathcal{L}$  is a measure of the flux of particles per unit area per unit time can be defined as:

$$\mathcal{L} = f n_b \frac{N_1 N_2}{A} \quad (4.1)$$

634 where  $f$  is the frequency of revolution of the beam,  $n_b$  the number of colliding pairs of bunches  
 635 in the beam,  $N_1$  and  $N_2$  are the number of particles in each colliding bunch and  $A$  is the cross-  
 636 section of the beam [35]. The peak luminosity evolution at the LHC is shown in Figure 4.2b.  
 637 Note that the operational  $\sqrt{s}$  of the LHC was 7 TeV for 2010/11 and 8 TeV for 2012.

638 The total amount of data collected is measured by the integrated luminosity  $\mathcal{L}_{\text{int}}$  defined  
 639 as the time integral of  $\mathcal{L}$ . Integrated luminosity has units of inverse area, usually expressed in  
 640 terms of barns (b)<sup>1</sup>. The probability for a given process to occur is expressed as the cross-section  
 641  $\sigma$  and the total number of events which proceed via said process is defined as:

$$\sigma \int \mathcal{L} dt \quad (4.2)$$

642 The integrated luminosity delivered by the LHC and collected by the ATLAS detector in  
 643 2011 and 2012 is shown in Figure 4.3. The ATLAS detector does not record all data delivered  
 644 by the LHC; approximately 6.5% was not recorded.

#### 645 4.1.1 Pileup

646 Due to the large number of interactions and the short time between collisions, multiple events  
 647 can overlap into a single event. This has detrimental effects on physics analyses and is a de-  
 648 termining factor in setting the instantaneous luminosity with which to perform data collection.  
 649 This overlapping effect is collectively known as pileup and is categorized into two types: in-  
 650 time pileup, where multiple  $pp$  collisions occur during the same bunch crossing; and out-of-  
 651 time pileup, where the electric signals produced by a previous collision is still present in the

---

<sup>1</sup>  $1 b^{-1} = 10^{-28} m^{-2}$

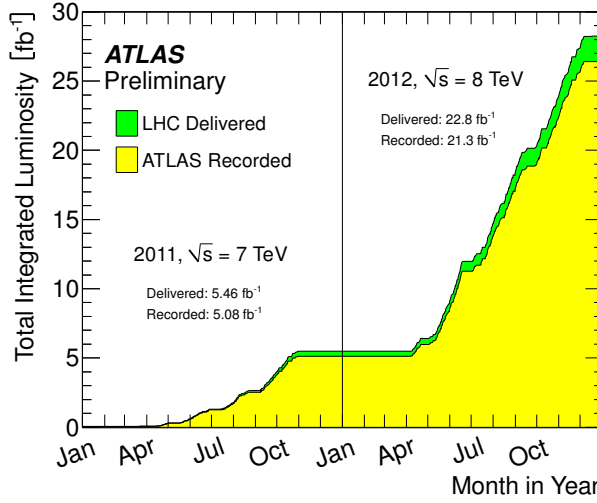


Figure 4.3: Distribution of the total integrated luminosity delivered by the LHC and the recorded by ATLAS for the 2011 and 2012  $pp$  collision period. Note the  $\sqrt{s}$  changing from 7 TeV to 8 TeV between 2011 and 2012.

652 detector. The number of interactions per crossing  $\mu$  is shown in Figure 4.4, note that on average  
 653 approximately thirty interactions occurred per bunch crossing in 2012. In comparison, in 2011  
 654 the average interactions per bunch crossing  $\langle \mu \rangle$  varied from  $\langle \mu \rangle = 5$  in early 2011 to  
 655  $\langle \mu \rangle = 15$  at the end of the year. The large number of overlapping events has a detrimental  
 656 effect on physics analyses and thus is an important factor when setting the operational  $\mathcal{L}$  of  
 657 the collider.

## 658 4.2 The ATLAS detector

659 The ATLAS [4] experiment is a general-purpose detector which wraps around the IP providing  
 660 large angular coverage. ATLAS is approximately cylindrical with a diameter of 25 m, a total  
 661 length of 44 m and weighs 7000 t. The detector is made of several layers of instrumentation  
 662 located at successively increasing radii as shown in Figure 4.5:

- 663 1. **Inner Detector:** Located nearest to the beam-pipe and designed to measure the track of  
 664 charged-particles.
- 665 2. **EM Calorimeter:** Used for identification and measurement of electrons and photons.
- 666 3. **Hadronic Calorimeter:** Used for the measurement of hadronic activity from hadroniz-

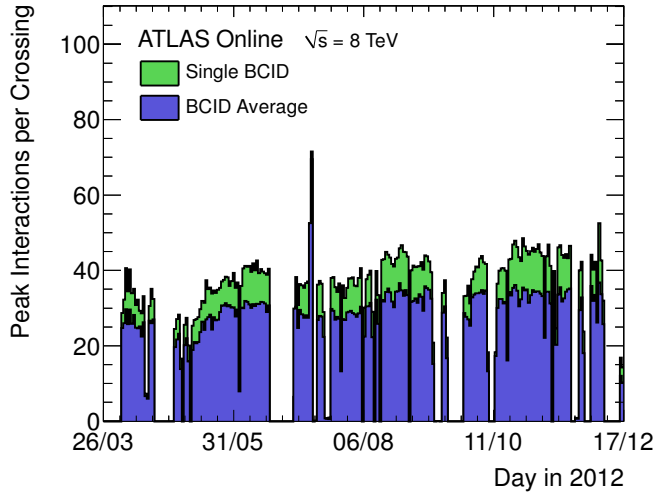


Figure 4.4: Number of interactions per bunch for the 2012  $pp$  data-taking period at ATLAS per day. Note that both the average number of interactions for all bunches and the maximum number of interactions are shown.

667 ing partons and missing transverse energy.

668 **4. Muon Spectrometer:** The outermost detection layer, used for muon identification and  
669 measurement.

670 Between these detection layers are magnets responsible for bending the path of the charged  
671 particles for the purpose of momentum measurement and particle identification. Additionally  
672 triggering and data acquisition (DAQ) systems form part of the detector for the purposes of  
673 recording the data signals coming from the aforementioned tracking and measurement sys-  
674 tems. A brief description of these systems is provided in the coming sections. For a more  
675 detailed technical description of the detector and all subsystems see [36].

676 Semi-leptonic  $t\bar{t}$  events produce a final state that includes hadronic activity, electrons,  
677 muons and missing energy and thus all elements of the detector are used in the reconstruction  
678 of such events. Additionally the match  $\chi^2_{\text{match}}$ -tagger which is central to this thesis relies on the  
679 reconstruction and fitting of inner detector tracks and muon spectrometer tracks. A detailed  
680 description of this algorithm is provided in the Chapter 6.

681 A cylindrical coordinate system as used by all ATLAS publications has been adopted here.  
682 The coordinate system is constructed so that the  $z$ -axis is parallel to the beam axis. The  $x$ -axis  
683 is positive in the direction going from the IP to the centre of the LHC ring, and the positive

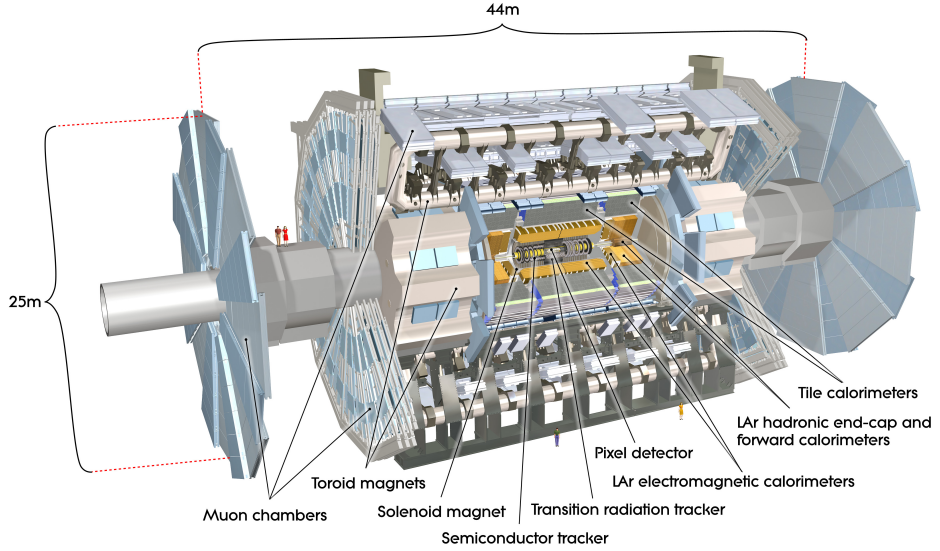


Figure 4.5: An overview diagram of the ATLAS experiment. Shown are all detection and tracking systems and the toroid magnet which encompasses them. Note also the muon system on the outside of the detector.

684  $y$ -axis points upwards. Thus the  $x - y$  plane is transverse to the beam direction. All transverse  
 685 variables such as the transverse momentum  $p_T$ , transverse energy  $E_T$  and missing transverse  
 686 energy  $\cancel{E}_T$  are measured along this plane. The azimuthal angle  $\phi$  is measured around the beam  
 687 axis, and the polar angle  $\theta$  is the angle from the beam axis. The pseudorapidity is defined as  
 688  $\eta = -\ln \tan(\theta/2)$ . The distance in the  $\phi$ - $\eta$  plane between two objects is denoted by  $\Delta R$  and  
 689 defined as  $\Delta R = \sqrt{\Delta\phi^2 + \Delta\eta^2}$ . Finally side A of the detector is defined as the positive  $z$  side  
 690 and side C is the negative  $z$ .

#### 691 4.2.1 Inner Detector

692 The inner detector (ID) is a tracking detector located closest to the beam-pipe and used for  
 693 momentum and impact parameter measurement, vertex and track reconstruction and particle  
 694 identification. The ID is designed to provide hermetic, high-resolution tracking in the range  
 695  $|\eta| < 2.5$ . All components of the ID subsystem are shown in Figure

696 The entire ID is contained within the central solenoid (CS) that generates a 2 T magnetic  
 697 field for the purpose of momentum measurement. The trajectory of a charged particle is bent  
 698 in the presence of a magnetic field. The str by a magnitude dependent on the momentum of  
 699 the particle. By reconstructing this trajectory the momentum can be measured.

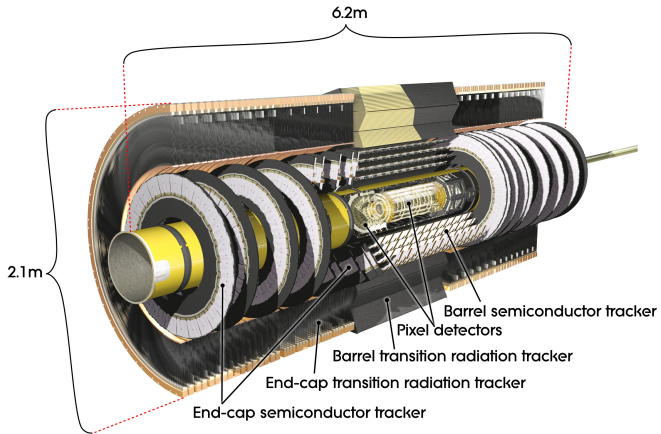


Figure 4.6: caption

700     The reconstruction of interaction vertices is of paramount importance, particularly when  
 701    considering the large amount of pile-up observed at ATLAS. Interaction vertices are recon-  
 702    structed by fitting all reconstructed tracks to a point. The primary vertex (PV) is then defined  
 703    as the vertex with the largest amount of momentum associated with it. In addition the recon-  
 704    struction of secondary interaction vertices is used for the identification of short-lived particles  
 705    such as  $B$ -hadrons and  $\tau$ .

706     The ID is made of three separate tracking and detection systems located at increasing radii  
 707    away from the beam-pipe, the full arrangement can be seen in Figure 4.8 and a plane-view is  
 708    shown in Figure 4.9.

### 709   **Pixel detector**

710     The pixel detector is located nearest to the beam-pipe and provides high-granularity and pre-  
 711    cision for secondary vertex reconstruction. It consists of three silicon pixel sensors layers in  
 712    the barrel region located at approximately 5 cm, 9 cm and 12 cm from the IP, and three disks  
 713    at each side located at constant  $R$  providing coverage up to  $|\eta| < 2.5$ . The barrel modules are  
 714    overlapped in a turbine pattern to provide hermetic coverage. In the barrel region the modules  
 715    provide an intrinsic resolution of  $10 \mu\text{m}$  in  $R - \phi$  and  $115 \mu\text{m}$  in  $z$ . The disk sections have an  
 716    intrinsic resolution of  $10 \mu\text{m}$  ( $R - \phi$ ) and  $115 \mu\text{m}$  ( $R$ ).

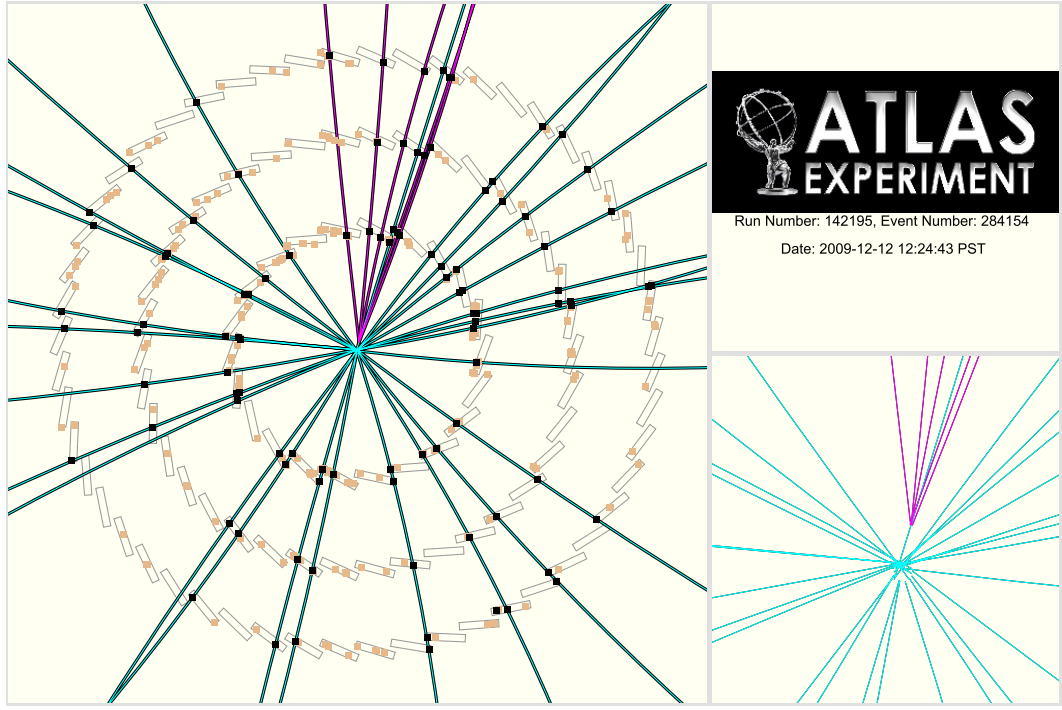


Figure 4.7: An event-display of an event as reconstructed by the ATLAS inner detector. Shown are the results of the vertexing algorithm where each line represents a track. the purple tracks have been fitted to a secondary vertex.

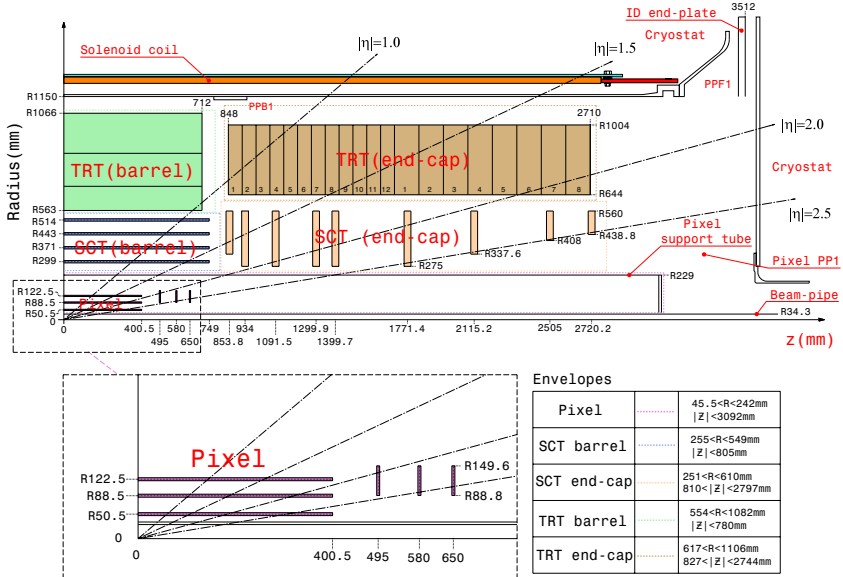


Figure 4.8: Plan-view of a quarter-section of the ATLAS ID showing the major detector elements with its active dimensions and envelopes. Note also the  $\eta$  markers showing the maximum coverage up to  $\eta = 2.5$ .

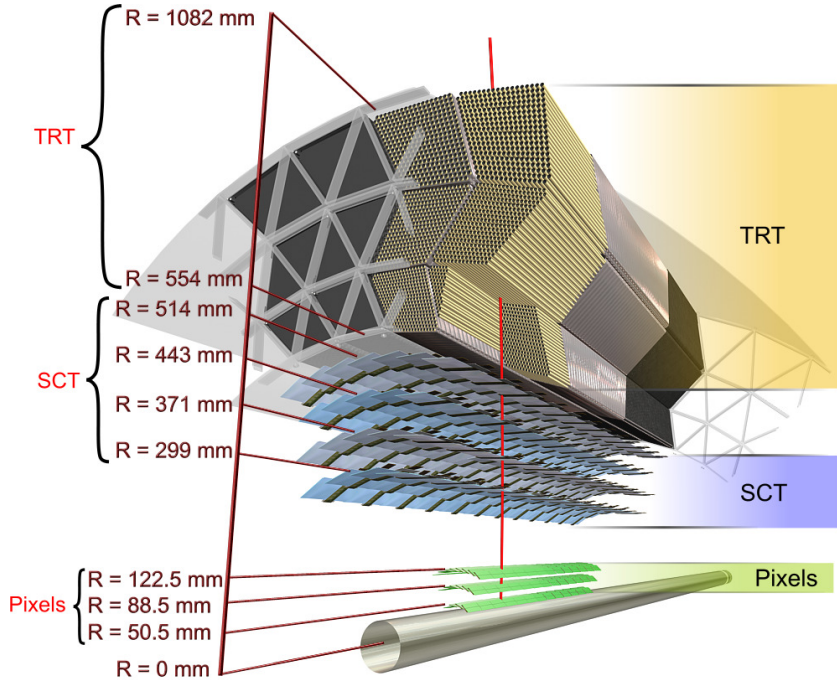


Figure 4.9: A drawing of in the transverse plane of the ATLAS ID showing all major detection elements in the barrel regions. Note the charged particle track marked in red traversing all the detector elements.

#### 717 Semiconductor tracker

718 The semiconductor tracker (SCT) located in the intermediate radius range is designed to pro-  
719 vide eight hits per track contributing to the measurement of momentum, impact parameter  
720 and vertex position. The SCT is made of four layers of stereo-pair silicon micro-strip sensors  
721 in the barrel region at increasing radii with an intrinsic resolution of  $17 \mu\text{m}$  ( $R - \phi$ ) and  $580 \mu\text{m}$   
722 ( $z$ ). At the end-caps nine disks of silicon microstrip modules provide large  $\eta$  coverage with a  
723 resolution of  $17 \mu\text{m}$  ( $R - \phi$ ) and  $580 \mu\text{m}$  ( $R$ ).

#### 724 Transition radiation tracker

725 The transition radiation tracker (TRT) is the outermost tracking layer that forms the inner  
726 detector. The TRT is designed to provide up to 36 hits per track using straw-tube sensors. In  
727 the barrel the 144 cm long straw-tubes are arranged in modules which contain between 329  
728 and 793 straws. The end-cap disks are made of radially distributed 36 cm long straw-tubes.  
729 Each straw-tube provides an intrinsic resolution of  $130 \mu\text{m}$  along its length. The combination  
730 of a large number of hits over a large radius allows for measurements in the TRT to be made

<sup>731</sup> with an accuracy that can complement those made by the pixel detector.

<sup>732</sup> **4.2.2 Calorimetry**

<sup>733</sup> The ATLAS calorimeter is responsible for the measurement of the energy of particles that  
<sup>734</sup> emerge from the event. Sampling calorimeters are used for this purpose, layers of absorber  
<sup>735</sup> material (passive) are placed in the path of the particles forcing them to interact and shower.  
<sup>736</sup> The amount of energy lost by the incident particle depends on the type of material the particle  
<sup>737</sup> traverses, the energy of the particle and the type. At high energies electrons lose energy pre-  
<sup>738</sup> dominantly via Bremsstrahlung, while photons lose energy via pair production. The character-  
<sup>739</sup> istic length associated with this energy loss is a material characteristic known as the radiation  
<sup>740</sup> length  $X_0$ .

<sup>741</sup> For electrons the energy as a function of material traversed is

$$E = E_0 e^{-x/X_0} \quad (4.3)$$

<sup>742</sup> where  $E$  is the energy of the incident particle,  $E_0$  is the original energy and  $x$  is the distance  
<sup>743</sup> traversed. As an electron traverses one  $X_0$  of material, its energy is reduced by a factor of  $1/e$ .  
<sup>744</sup> For photons the average number of photons traversing through a material length  $x$  is reduced  
<sup>745</sup> exponentially by a factor of  $\frac{7}{9}X_0$ .

<sup>746</sup> The energy of the resulting shower is then measured by some sampling material (active)  
<sup>747</sup> located behind the absorbers, this energy is proportional to the energy of the incident particle.

<sup>748</sup> The type and thickness of material used is varied through the pseudorapidity range to  
<sup>749</sup> improve energy measurement and reduce punch-through of particles into the muon systems  
<sup>750</sup> behind. Due to the large amount of intense radiation produced during collisions, radiation  
<sup>751</sup> hardness is also a driving factor in material choice.

<sup>752</sup> The ATLAS calorimeter consists of the electromagnetic (EM) calorimeter, designed to mea-  
<sup>753</sup> sure photons and electrons covering the pseudorapidity region  $|\eta| < 3.2$ ; the hadronic calorime-  
<sup>754</sup> ter (HCal), designed to measure hadronic activity covering the pseudorapidity region  $|\eta| < 3.2$ ;  
<sup>755</sup> and the forward calorimeter (FCal) which provides energy measurement capability in the very  
<sup>756</sup> high pseudorapidity region  $3.1 < |\eta| < 4.9$ . As can be seen in Figure 4.10 the calorimetry  
<sup>757</sup> envelopes the ID and CS providing hermetic coverage symmetric in  $\phi$ . This is particularly im-

758 portant for the measurement of  $E_T$  resulting from weakly interacting particles escaping the  
 759 detector.

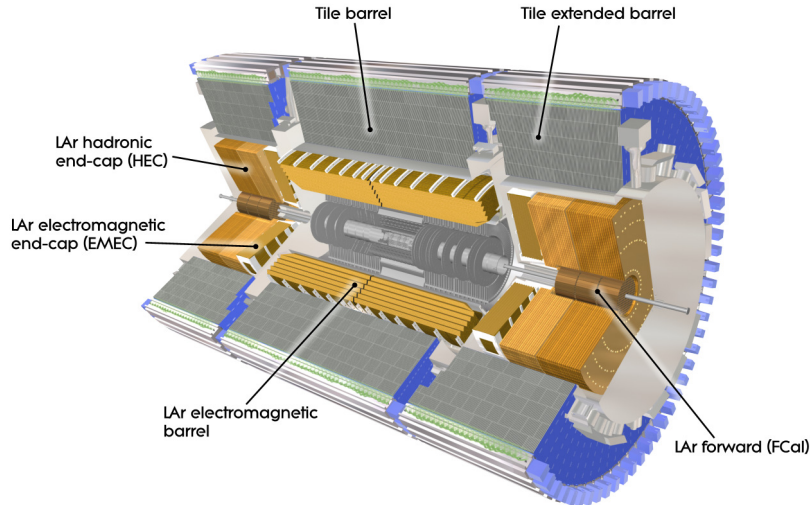


Figure 4.10: A cut-away diagram of the ATLAS detector highlighting the calorimetry system. Shown are the ECal barrel and end-cap, the HCal barrel and end-cap and the FCal end-cap.

#### 760 Electromagnetic calorimeter

761 The EM calorimeter is made of a barrel section ( $|\eta| < 1.475$ ) and two end-caps ( $1.375 <$   
 762  $|\eta| < 3.2$ ). The EM barrel consists of two half-barrels separated by a 4 mm gap at  $z = 0$ .  
 763 The end-caps consist of two coaxial wheels, the outer ring covering the pseudorapidity range  
 764  $1.375 < |\eta| < 2.5$  and the inner ring covering the range  $2.5 < |\eta| < 3.2$ . The pseudorapidity  
 765 region  $1.37 < |\eta| < 1.52$  is not used for precision physics due to the large amount of material,  
 766 this is known as the “crack” region.

767 The EM calorimeter employs liquid Argon (LAr) as the active material due to its intrinsic  
 768 radiation hardness and response over time, and lead as the passive material arranged in an  
 769 accordion geometry for full  $\phi$  symmetry. Particles interact with the lead absorbers creating a  
 770 shower which ionizes the layers of liquid Argon. A potential is applied across the LAr mate-  
 771 rial allowing for signal readout via Kapton/copper electrodes. The total thickness of the EM  
 772 calorimeter is  $> 24X_0$  in the barrel and  $> 26X_0$  in the end-caps. The amount of material is  
 773 optimized in pseudorapidity to enhance energy resolution.

774 In the region devoted to precision physics the EM calorimeter is divided into three seg-

Table 4.1: Design energy resolution of all ATLAS calorimeter components. The resolution is made of a sampling term ( $1/\sqrt{E}$ ) associated with the choice of passive and active materials and construction of the layers and a constant term associated with the depth of the detector, cracks and dead material.

Section	Resolution
EM Barrel	$\frac{10\%}{\sqrt{E}} \oplus 0.7\%$
EMEC	$\frac{10\%}{\sqrt{E}} \oplus 0.7\%$
HEC	$\frac{100\%}{\sqrt{E}} \oplus 10\%$
FCAL	$\frac{100\%}{\sqrt{E}} \oplus 10\%$

ments as shown in Figure 4.11, the strip layer is designed to improve particle identification and pseudorapidity position measurement. The design energy resolution for all components of the calorimeter are shown in Table 4.1.

### Hadronic calorimeter

The hadronic calorimeter uses different types of passive and active material to accomodate for the varying conditions in different regions of the detector. The materials used and structure of the detector must provide good energy resolution, full symmetric coverage for the purpose of  $E_T$  measurement, full containment of all hardonic activity to prevent punch-through to the muon system and be sufficiently radiation hard.

The hadronic calorimeter consists of two parts a scintillator tile calorimeter in the barrel region, and a LAr calorimeter in the end-cap.

The tile calorimeter is located directly outside the EM calorimeter. The barrel portion of the calorimeter covers the region  $|\eta| < 1.0$  and the two extended barrels cover the range  $0.8 < |\eta| < 1.7$ . The tile calorimeter uses steel as the passive material and scintillating tiles as the active material. The resulting hadronic showers enter the scintillating tiles and produce photons which are passed to photomultiplier tubes (PMTs). The total detector thickness which is tile-instrumented is 9.7 interaction lengths ( $\lambda$ ) at  $\eta = 0$ .

The hadronic end-cap (HEC) uses LAr technology due to its radiation-hardness in this challenging high pseudorapidity region. The HEC consists of two independent wheels per end-cap covering the range  $1.5 < |\eta| < 3.2$  overlapping the tile calorimeter at low pseudorapidity range and the forward calorimeter located at high pseudorapidity.

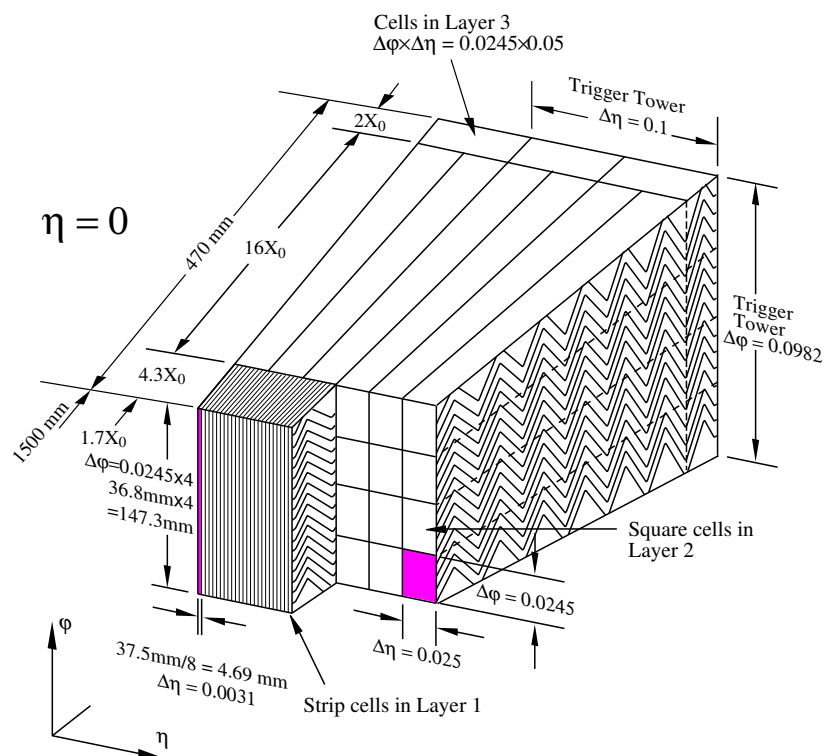


Figure 4.11: Cut-away diagram of the EM calorimeter barrel at  $\eta = 0$ . Shown are the three different layers with varying cell structures. The strip section is designed to enhance particle identification and position measurement in  $\eta$ .

796 **Forward calorimeter**

797 The forward calorimeter (FCal) is responsible for energy measurement in the very-high pseu-  
 798 dorapidity range  $3.1 < |\eta| < 4.9$  of both electromagnetic and hadronic activity. Due to the  
 799 large amount of radiation in this  $\eta$  region, LAr is employed as the active material. The FCal con-  
 800 sists of three layers, the first made primarily of copper, designed mostly for the measurement  
 801 of electromagnetic activity while the two outer tungsten layers are responsible for hadronic  
 802 activity measurement.

803 **4.2.3 Muon spectrometer**

804 The muon spectrometer (MS) is the outer most layer of the ATLAS detector (Figure 4.12) and  
 805 is responsible for the precision measurement of  $p_T$  of charged-particles that pass-through the  
 806 ATLAS calorimetry. Muon tracking performance is vital to the SMT tagger described in Sec-  
 807 tion 6.1, as it relies on the precise reconstruction of muon tracks in the ID and MS. Inner detector  
 808 tracks and Muon spectrometer tracks are fitted to form a *combined* muon track, the quality of  
 809 the fit is at the core of the SMT algorithm.

810 Due to their larger mass, muons tend to have a larger tranverse momentum and as such  
 811 do not lose as much energy through the emission of photons in the calorimetry. As a result,  
 812 muons tend to traverse the hadronic calorimeter and escape the detector volume. The muon  
 813 system provides measurement of these particles up to  $|\eta| < 2.7$  and triggering up to  $|\eta| < 2.4$ .  
 814 Measurement of  $p_T$  is facilitated by the magnetic field generated by the large toroid magnet  
 815 in the barrel region  $|\eta| < 1.4$  and two smaller end-cap magnets in  $1.6 < |\eta| < 2.7$ . In the  
 816 transition region ( $1.4 < |\eta| < 1.6$ ) deflection is provided by the barrel and end-cap fields.

817 The structure of the MS is delimited by the magnet system. In the barrel region three  
 818 cylindrical layers of precision-tracking chambers are located in and on the coils of the barrel  
 819 toroid magnet at radii of 5 m, 7.5 m and 10 m. End-cap region coverage is provided by three  
 820 chamber planes perpendicular to the  $z$ -axis located in front and behind the end-cap toroid  
 821 magnet at distances  $|z| \approx 7.4$  m, 10.8 m, 14 m and 21.5 m from the interaction point.

822 The MS contains four different types of chambers responsible for precision-tracking and/or  
 823 triggering in various pseudorapidity ranges as shown in Table 4.2. The arrangement of these  
 824 chambers is shown in Figure 4.13.

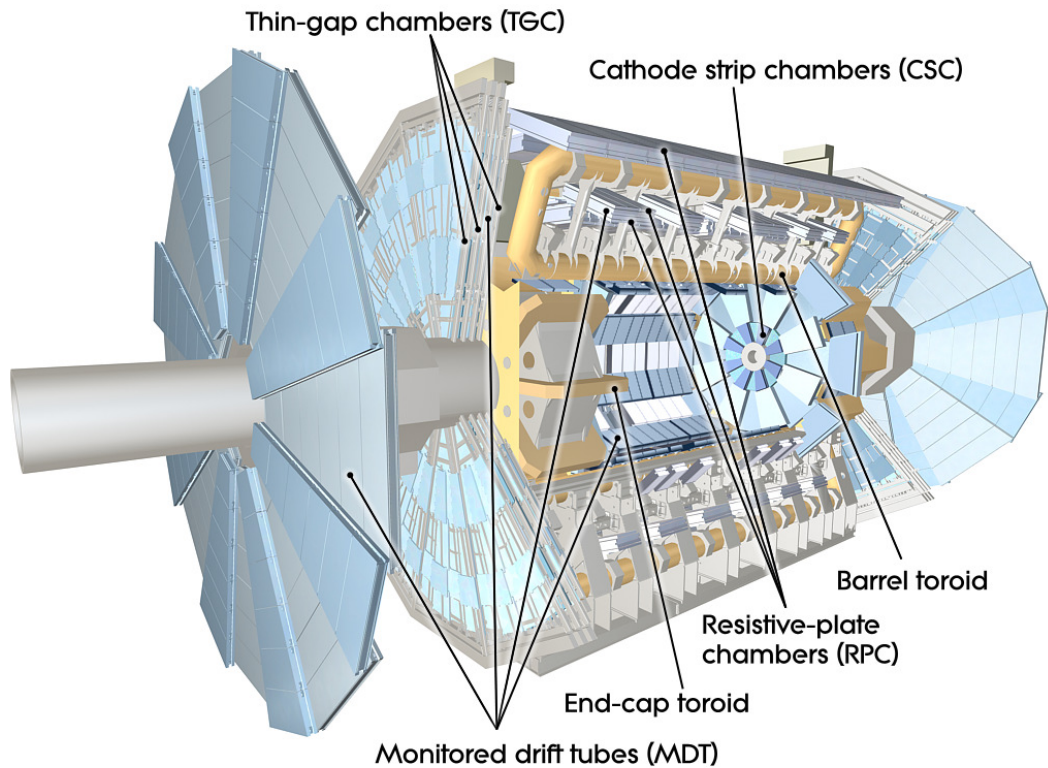


Figure 4.12: Cut-away drawing of the ATLAS muon system.

<b>Monitored drift tubes</b>	<b>MDT</b>
<ul style="list-style-type: none"> <li>- Coverage</li> <li>- Number of chambers</li> <li>- Function</li> </ul>	$ \eta  < 2.7$ (innermost layer: $ \eta  < 2.0$ ) 1150 Precision tracking
<b>Cathode strip chambers</b>	<b>CSC</b>
<ul style="list-style-type: none"> <li>- Coverage</li> <li>- Number of chambers</li> <li>- Function</li> </ul>	$2.0 <  \eta  < 2.7$ 32 Precision tracking
<b>Resistive place chambers</b>	<b>RPC</b>
<ul style="list-style-type: none"> <li>- Coverage</li> <li>- Number of chambers</li> <li>- Function</li> </ul>	$ \eta  < 1.05$ 606 Triggering, second coordinate
<b>Thin gap chambers</b>	<b>TGC</b>
<ul style="list-style-type: none"> <li>- Coverage</li> <li>- Number of chambers</li> <li>- Function</li> </ul>	$1.05 <  \eta  < 2.7$ (2.4 for triggering) 3588 Triggering, second coordinate

Table 4.2: Main parameters of the muon system.

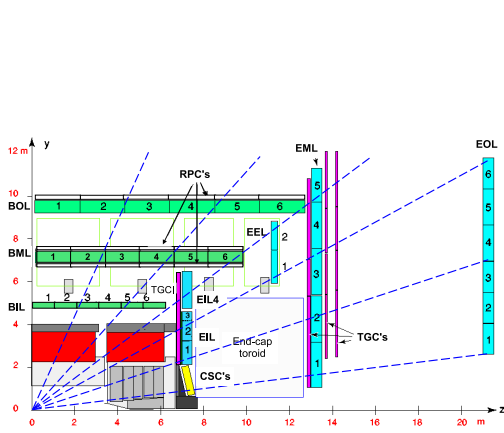


Figure 4.13: Plan view of quarter-section of the ATLAS muon spectrometer.

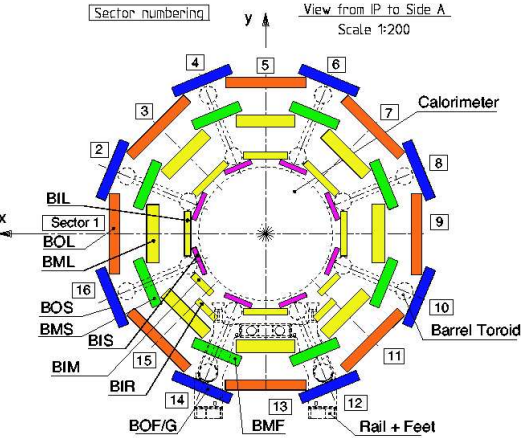


Figure 4.14: Transverse view of the muon system. Shown are the

825 In the barrel region, precision-measurement is performed by monitored drift tubes (MDT)  
 826 chambers. These chamber consist of three to eight pressurised aluminium drift tubes, each  
 827 containing a tungsten-rhenium wire anode and a mixture of argon and carbon dioxide gas. An  
 828 average spatial resolution of  $80 \mu\text{m}$  per tube and  $35 \mu\text{m}$  per chamber is achieved.

829 The end-cap region is instrumented with cathode-strip chambers (CSC) due to their higher  
 830 rate capability and time resolution. CSCs are multiwire chambers with cathode planes seg-  
 831 mented into strips in orthogonal directions. This allows for both coordinates to be measured  
 832 simultaneously. The resolution of a chamber is  $40 \mu\text{m}$  in the bending plane ( $R - z$ ) and  $5 \text{ mm}$   
 833 in the transverse plane.

834 Triggering on muon tracks is another essential role of the muon spectrometer. To this end,  
 835 each precision-measurement chamber is complemented with fast triggering chambers. As with  
 836 the measurement layers, two different types of chambers are used for the barrel and end-cap  
 837 regions. In the barrel region ( $|\eta| < 1.05$ ) resistive plate chambers (RPC) are used attached to the  
 838 same support structure as the MDTs. The RPCs are made of two resistive plates,  $2 \text{ mm}$  apart,  
 839 between which a potential difference is applied. The gap between the plates is filled with a  
 840 mixture of  $\text{C}_2\text{H}_2\text{F}_4/\text{Iso-C}_4\text{H}_{10}/\text{SF}_6$ . The signal is read out via metallic strips mounted to the  
 841 outer faces of the resistive plates. The end-cap region ( $1.05 < |\eta| < 2.4$ ) is populated with  
 842 thin gap chambers (TGC). TGCs multiwire chambers like those used in the CSC, however the  
 843 distance between the wire and the cathode is smaller in the TGC. A summary of the spatial  
 844 and temporal resolution for the measurement and triggering layers is shown in Table 4.3.

Type	$R/z$	$\phi$	time
MDT	35 $\mu\text{m}$ ( $z$ )	–	–
CSC	40 $\mu\text{m}$ ( $R$ )	5 mm	7 ns
RPC	10 mm ( $z$ )	10 mm	1.5 ns
TGC	2-6 mm ( $R$ )	3-7 mm	4 ns

Table 4.3: Summary of spatial and temporal resolutions per chamber for all chamber types used in the the ATLAS muon spectrometer. Adapted from [4].

#### 845 4.2.4 Magnet system

846 The structure of the ATLAS detector is defined by the large magnet system. The ATLAS magnet  
 847 system, shown in Figure 4.15, consists two sets of magnets. The central solenoid and three air-  
 848 core toroids.

849 The central solenoid located nearest to the beam, provides a 2 T magnetic field for the ID  
 850 for the purpose of tracking, particle identification and  $p_{\text{T}}$  measurement.

851 The barrel toroids extend to  $|\eta| < 1.4$  and are made of eight coils, generating a 0.5 T  
 852 magnetic field for the MS. In the high pseudorapidity range, magnetic deflection is provided  
 853 by two end-cap toroids extending from  $1.6 < |\eta| < 2.4$ . As in barrel, the end-cap toroids are  
 854 made of eight coils offset by  $22.5^\circ$  with respect to the barrel coils. Each end-cap generates a 1 T  
 855 magnetic field for the MS. The so-called transition region between the two magnets is covered  
 856 by an overlap of the end-cap and barrel fields.

#### 857 4.2.5 Triggering and DAQ

858 At the design luminosity of  $10 \times 10^{34} \text{ cm}^{-2} \text{ s}^{-1}$  it is expected that the amount of data produced  
 859 is approximately  $1 \text{ PB s}^{-1}$ . Clearly it is impossible to store

### 860 4.3 Athena Control Framework and ROOT Framework

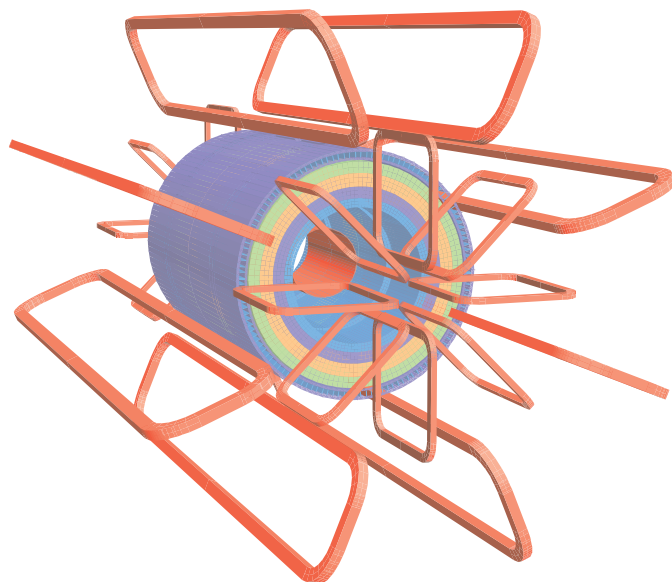


Figure 4.15: Diagram of the ATLAS toroid magnet system. The red central solenoid is located closest to the beam surrounded by layers of tile calorimetry. The eight barrel toroid magnets are shown along with the offset end-cap toroids at each end.

## <sup>861</sup> Chapter 5

# <sup>862</sup> Calibration of the Soft Muon Tagger <sup>863</sup> for 2012 ATLAS Data

<sup>864</sup> High-energy physics relies heavily on the use of simulated data to inform the development of  
<sup>865</sup> analysis techniques. It is thus paramount that the simulation reflect nature as closely as pos-  
<sup>866</sup> sible. However the simulation does not accurately predict conditions within the detector and  
<sup>867</sup> the effects on the muon reconstruction and the quality of the fit between the inner detector  
<sup>868</sup> tracks and muon spectrometer tracks which is represented in the  $\chi^2_{\text{match}}$ . Instead the difference  
<sup>869</sup> between simulation and data is quantified and taken into account. This process is known as  
<sup>870</sup> calibration. In the case of the muon reconstruction method and the  $\chi^2_{\text{match}}$  tagger it is impor-  
<sup>871</sup> tant that the difference in efficiency between MC and data be accounted for. This is done by  
<sup>872</sup> constructing a scale factor, defined in this case by:

$$\kappa_{\chi^2_{\text{match}}} = \frac{\epsilon_{\chi^2_{\text{match}}}^{\text{Data}}}{\epsilon_{\chi^2_{\text{match}}}^{\text{MC}}} \quad (5.1)$$

<sup>873</sup> One of the advantages of using the  $\chi^2_{\text{match}}$  tagger over other forms of tagging is that the  
<sup>874</sup> presence of a jet is not required to measure the  $\chi^2_{\text{match}}$  of a muon. This means that the calibration  
<sup>875</sup> can be performed on isolated muons such as those from  $J/\psi \rightarrow \mu\mu$  or  $Z \rightarrow \mu\mu$  using the so  
<sup>876</sup> called tag and probe method. This calibration relies on muons with low  $p_T$  from  $J/\psi$  decays.  
<sup>877</sup> As the  $\chi^2_{\text{match}}$  is a characteristic of combined and therefore reconstructed muons,  
<sup>878</sup> The tag and probe method used in this calibration is defined as follows. One reconstructed

combined muon is designated as the Tag, this muon must pass a stringent set of cuts implying that this is indeed a muon from a  $J/\psi$ . The second muon which is designated as the Probe is constructed from an inner detector (ID) only. To ensure that the Probe is the second muon from the  $J/\psi$  decay, the invariant mass of the combined tag and probe system is required to be within a mass window centered around the true  $J/\psi$  mass. The complete selection used in the calibration is detailed in Section 5.1. These Probes are then used to measure the reconstruction efficiency and the  $\chi^2_{\text{match}}$  tagger efficiency as described in Sections 5.2 and 5.3.

The tag and probe method used here is based on a previous calibration of the  $\chi^2_{\text{match}}$  tagger performed on 2011 ATLAS collision data outlined in This analysis differs from the 2011 calibration in several ways these will be highlighted and explained.

### 5.0.1 Software, Collision Data and Simulated samples

The tag and probe method used here was implemented using the ROOT analysis framework.

The calibration was performed on a dataset made of those luminosity blocks selected by the recommended standard Good Runs List (GRL) which corresponds to all  $pp$  collision periods in 2012. The GRL selects only those luminosity blocks where detector conditions are appropriate for physics data-taking. This includes all relevant detector components being operational and that stable beam conditions have been achieved. The datasets are part of the 2013 summer reprocessing (processing tag p1328) corresponding to data taken in periods A through to L, excluding periods F and J.

The efficiency scale factor is measured against a sample containing almost 10 million  $J/\psi \rightarrow \mu\mu$  events. At event generation filters are applied so the sample only contains events where both muons have a transverse momentum of at least 4 GeV and they must lie within the pseudorapidity range  $|\eta| < 2.5$ . This selection matches the object selection used by most analyses as recommended by the Muon Combined Performance (MCP) group.

## 5.1 Tag and Probe Selection

A tag and probe method was chosen to measure the efficiency of muon reconstruction and the  $\chi^2_{\text{match}}$  tagger. The tag and probe method allows for the measurement of the performance of selection criteria or algorithms by exploiting well known decays. By creating a sample

907 of objects, in this case muons, on which to apply the aforementioned selection criteria, it is  
 908 possible to study these algorithms.

909 The muon reconstruction algorithm examines various Inner Detector (ID)tracks and Muon  
 910 Spectrometer (MS) tracks and makes a determination as to whether said track is produced by  
 911 muon or not. To measure the performance of the muon reconstruction algorithm a sample of  
 912 ID tracks which originate from the  $J/\psi$  decay and are thus very likely to be a real muon is  
 913 constructed. This is done in the following way:

914 First, require the presence of a combined STACO muon which passes a very stringent selec-  
 915 tion. This strongly implies that this is a real muon and thus is labelled as the Tag. Additionally  
 916 a very loose selection is applied to all ID tracks. These are known as candidate Probes. Pairs  
 917 of tag and probes are then formed by requiring that the combined invariant mass lie within a  
 918  $J/\psi$  mass window and the pair pass additional pairing cuts. This then implies that the Probe  
 919 is likely the other muon from the  $J/\psi$  decay and as such is a suitable test-bed to measure the  
 920 performance of the muon reconstruction algorithm. Note that all selection criteria are detailed  
 921 and explained in Section 5.1.2

922 After selecting a sample of probes the performance of the algorithm is estimated by mea-  
 923 suring the proportion of probe candidates which are selected by the algorithm. In other words  
 924 the performance is estimated by counting the number of muons which are reconstructed given  
 925 that the ID track is very likely to be a real muon. Probes which are reconstructed into combined  
 926 STACO muons are labelled as muon probes. The performance of the  $\chi^2_{\text{match}}$  tagger is estimated  
 927 in a similar manner, by measuring the proportion of combined muon probes which pass the  
 928 SMT selection.

### 929 5.1.1 Trigger requirements

930 In order for an event to be included in the analysis it must pass at least one of the trigger chains  
 931 listed in Appendix A. For the sake of brevity only the primary trigger (EF\_mu6\_Trk\_Jpsi\_loose)  
 932 which contributes the majority of events is described here.

933 As stated in the trigger name this is an Event Filter trigger which requires the presence of  
 934 a muon with a momentum of at least 6 GeV and an ID track whose combined invariant mass lies  
 935 within a  $J/\psi$  mass window of  $2.6 \text{ GeV} < m_{\text{inv}} < 3.6 \text{ GeV}$ . This loose mass window contains the  
 936 entirety of the  $J/\psi$  peak in all examined  $p_T$  and  $\eta$  ranges as well as additional side bands to

allow for background removal. Note the omission of double muon triggers to avoid introducing a bias by specifically selecting events with two good muons.

Also note that while all triggers are operational in all periods, most are heavily prescaled and the prescale is period dependent. This does not have a first-order effect on the measurement since only ratios are compared between collision data and MC.

### 5.1.2 Selection Cuts

The selection criteria for tags, probes, muon probes and SMT muons are listed and detailed below. Note that all cuts are applied on the kinematic properties measured in the ID due to its improved resolution unless it is not possible as in the case of the  $\chi^2_{\text{DoF}}$  which is a combined MS and ID property. Also note that all objects must pass a selection criteria collectively referred to as MCP cuts. These are tracking quality cuts which require a certain number of detector elements be active to ensure good tracking. These cuts are listed in

The muon tag selection criteria are defined in the list below:

- MCP cuts
- STACO collection
- Combined muon
- $p_T > 4 \text{ GeV}$
- $|\eta| < 2.5$
- $|d_0| < 0.3 \text{ mm}$  and  $|z_0| < 1.5 \text{ mm}$
- $|d_0/\sigma_{d_0}| < 3$  and  $|z_0/\sigma_{z_0}| < 3$
- Fired at least one of the relevant triggers (see Appendix A)

Included are cuts on the muon impact parameter (IP)  $d_0$  and  $z_0$ . These are defined as the distance of closest approach of the ID track to the primary interaction vertex in the transverse and longitudinal planes, respectively. Additionally cuts on the absolute values of IP significances are also implemented. The significance of the impact parameter is defined as  $d_0/\sigma_{d_0}$  where  $\sigma_{\text{IP}}$  is the standard deviation of the impact parameter. These cuts are designed to ensure that the

963 muon selected originates near the primary vertex and thus from a prompt  $J/\psi$  from the pri-  
 964 mary collision. Note that non-prompt  $J/\psi$  can be produced in the decay of  $b$  hadrons. Finally  
 965 note that the tag muon must match the trigger object which selected this event.

966 The probe selection is a subset of the tag selection and only requires an ID track with  
 967  $|\eta| < 2.5$  and  $p_T < 4 \text{ GeV}$ . The pairing cuts are shown below:

- 968     •  $2 \text{ GeV} \leq m_{\text{inv}} \leq 4 \text{ GeV}$
- 969     • Probe charge is opposite the tag charge
- 970     •  $0.4 < \Delta R(\text{tag}, \text{probe}) < 3.5$
- 971     •  $\Delta z_0(\text{tag}, \text{probe}) < 0.2 \text{ mm}$

972 The probe and the tag are required to be fairly well separated to avoid the momentum of  
 973 the tag from entering the isolation cone of the probe. In the 2011 calibration analysis the track  
 974 of the tag and the probe are refit to a common vertex and the quality of the refit, expressed by  
 975 the  $\chi^2$  is a part of the pairing criteria. This criteria is present to reduce the effects of pile-up  
 976 on the measurement, by ensuring both objects have a common origin. Since the data format  
 977 used for this analysis is a derived form of that used in 2011 it is not possible to perform such a  
 978 refit. Instead the difference between the  $z_0$  of the tag and the probe is used.

979 The STACO reconstruction efficiency is not measured by applying the algorithm on the  
 980 probe collection but rather a probe is said to be a muon probe if it matches a combined muon  
 981 from the STACO collection. This is done by requiring the angular separation between the probe  
 982 and the STACO muon be less than 0.001. Probes which are matched become the numerator of  
 983 the reconstruction efficiency and the denominator is defined as the number of probes:

$$\epsilon = \frac{N_{\text{muon probe}}}{N_{\text{probe}}}$$

984 A muon probe is said to be an SMT muon if it passes the following selection, which matches  
 985 the muon cuts defined in Section 6.1. Note in particular the main component of the soft muon  
 986 tagger, the cut on  $\chi^2_{\text{match}}/N_{\text{dof}} < 3.2$ , the distribution of the  $\chi^2_{\text{DoF}}$  is shown in Fig. 5.1

- 987     •  $|d_0| < 3 \text{ mm}$
- 988     •  $|z_0 \sin(\theta)| < 3$

- 989 •  $\chi^2_{\text{match}}/N_{\text{dof}} < 3.2$

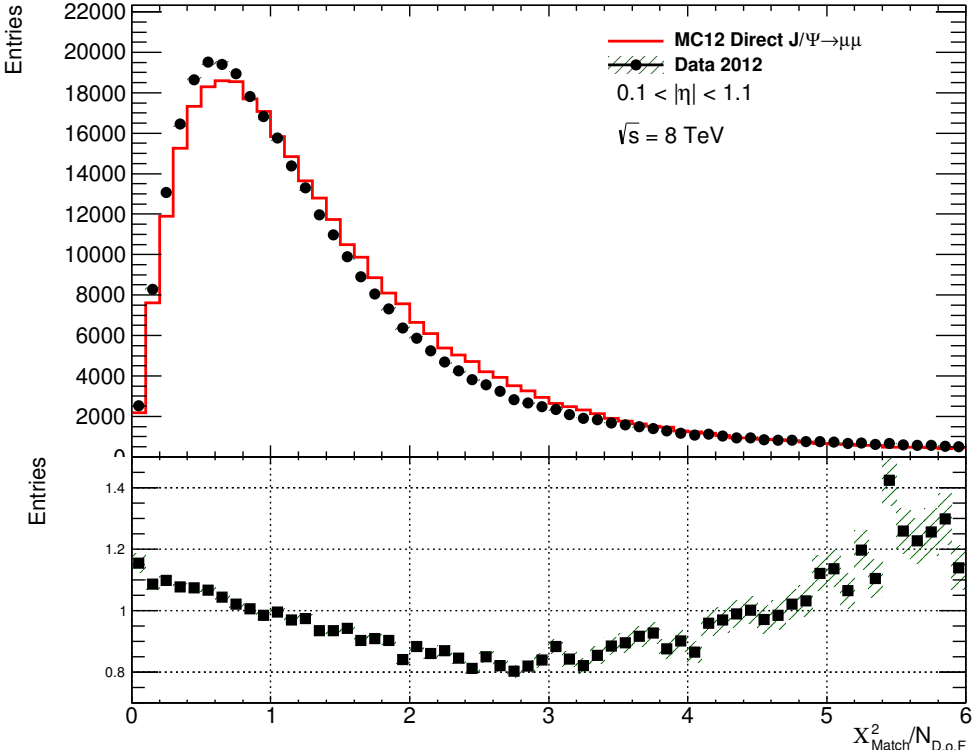


Figure 5.1: The distribution of  $\chi^2_{\text{match}}/N_{\text{dof}}$  for all muon probes for ATLAS collision data and prompt  $J/\psi$  Monte Carlo simulation.

990 Those muon probes which pass the SMT selection are the numerator of the SMT efficiency  
 991 and the denominator is defined as the number of muon probes:

$$\epsilon = \frac{N_{\text{SMT}}}{N_{\text{muon probe}}}$$

## 992 5.2 Invariant mass fitting

993 The pairing criteria are very effective at selecting  $J/\psi$  events, however non- $J/\psi$  background  
 994 events are also pass the selection. These include combinatorial background where the wrong  
 995 tag and probe pair is constructed and Drell-Yan which appears as a continuum below the  $J/\psi$   
 996 peak.

997 The number of probes is extracted from a fit to the invariant mass of the dimuon system  
 998 using a composite function to accomodate for the background and the gaussian-like  $J/\psi$  peak.

999     The invariant mass peak of the  $J/\psi$  is modelled by a gaussian distribution while the back-  
 1000    ground distribution is modelled by a quadratic. The invariant mass distribution is fit by a sum  
 1001    of the two functions.

1002     To avoid the first-order effects of signal mis-modelling from the fit of the  $J/\psi$  peak, the  
 1003    yield is obtained from the integral of the measured invariant mass distribution subtracting  
 1004    the background contribution from the integral of the fit to the background. The integration is  
 1005    performed in a window with a width based on the width of the fitted  $J/\psi$  peak. The integration  
 1006    window marked in Fig. 5.2 corresponds to three times the width of the peak or simply  $3\sigma$ .  
 1007    Additionally note the composite fit line as well as the background-only distribution and the  
 1008    implied signal gaussian peak.

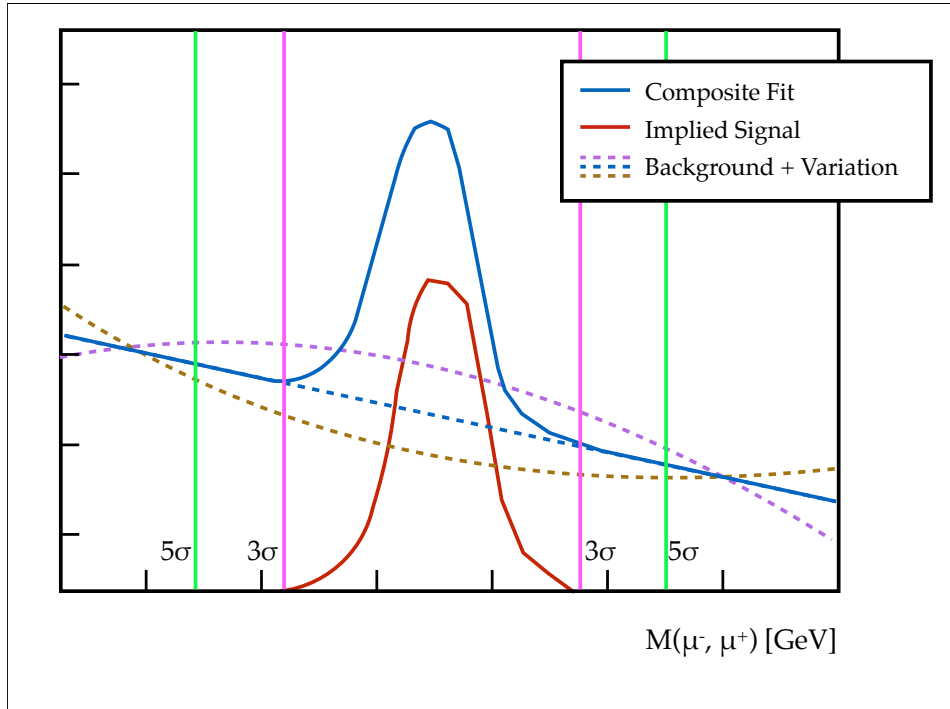


Figure 5.2: A diagram of the various components of the fit procedure. The composite fit is shown along with the corresponding implied signal and background. The two variations of the background shape are also shown.

1009 **5.2.1 Uncertainty Measurement**

The uncertainty on the efficiency is made of three components. First, the statistical uncertainty on the efficiency is estimated as a Binomial error,

$$\delta\epsilon = \sqrt{\frac{\epsilon \times (1 - \epsilon)}{N}}$$

1010 where  $\epsilon$  is the measured efficiency and  $N$  is, in this case the denominator of the efficiency  
1011 measured.

1012 Secondly, an uncertainty is associated with the fit to the background. This is done by taking  
1013 the largest upward and downward fluctuations of the background by the uncertainty on the fit  
1014 parameters of the background, and obtaining the maximum upward and downward effects on  
1015 the efficiency. After the fit of the composite function is carried out, a downward variation of  
1016 the background is defined as:

$$f(x) = a_{\min}x^2 + b_{\max}x + c_{\min}, \text{ where } p_{\max/\min} = p_{\text{central}} \pm \sigma_p$$

where the maximum and minimum of a parameter is obtained by varying the central value by the uncertainty obtained from the fit. The upward variation of the background fit is thus the opposite, defined as:

$$f(x) = a_{\max}x^2 + b_{\min}x + c_{\max}$$

1017 These background variation then result in the maximum deviation from the nominal  
1018 integral. Again Fig. 5.2 shows these two variations<sup>1</sup>. The uncertainty on the efficiency is then  
1019 determined by obtaining the maximum efficiency in both directions. If the nominal efficiency  
1020 is defined as:

$$\epsilon_{\text{nominal}} = \frac{N_{\text{numerator}}}{N_{\text{denominator}}}$$

Then the variations are defined as follows:

$$\epsilon_{\text{up}} = \frac{N_{\text{numerator}}^{\text{down}}}{N_{\text{denominator}}^{\text{nominal}}}, \quad \epsilon_{\text{down}} = \frac{N_{\text{numerator}}^{\text{nominal}}}{N_{\text{denominator}}^{\text{up}}}$$

---

<sup>1</sup>The variation shown in the diagram is very exaggerated and meant for illustration purposes

Finally the uncertainty on the background is given by adding the differences between  $\epsilon_{\text{up}}$  and  $\epsilon_{\text{down}}$  and the nominal efficiency, in quadrature:

$$\sigma_{\text{bkg}} = \sqrt{|\epsilon_{\text{up}} - \epsilon|^2 + |\epsilon_{\text{down}} - \epsilon|^2}$$

The final component of the uncertainty is constructed by varying the integration window. The nominal value is defined as  $3\sigma$  away from the center of the fitted gaussian, where again  $\sigma$  is the FWHM of the same fitted gaussian. An uncertainty is constructed by measuring the efficiency with a wide integration window corresponding to  $5\sigma$ . The integration window uncertainty is defined as:

$$\sigma_{\text{window}} = |\epsilon_{5\sigma} - \epsilon_{3\sigma}|$$

1021 Finally, the total uncertainty on the efficiency is given by the sum in quadrature of the all  
 1022 uncertainty components. The uncertainty on the efficiency is then carried over to the scale  
 1023 factor determination.

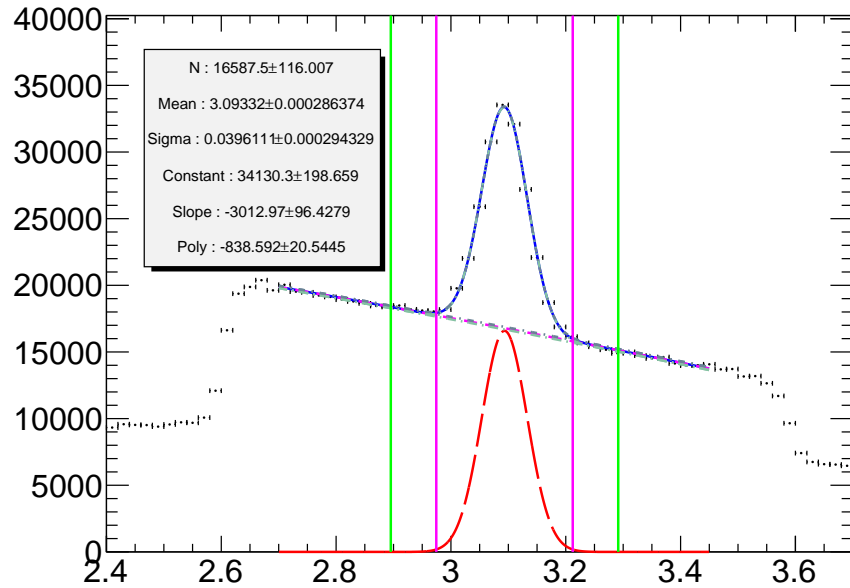
1024 An example of the fitting procedure applied is shown in Fig. 5.3 for both tag and probes at  
 1025 probe level and at muon probe level. Note that as expected the muon probe contains far less  
 1026 background.

## 1027 5.3 Efficiencies

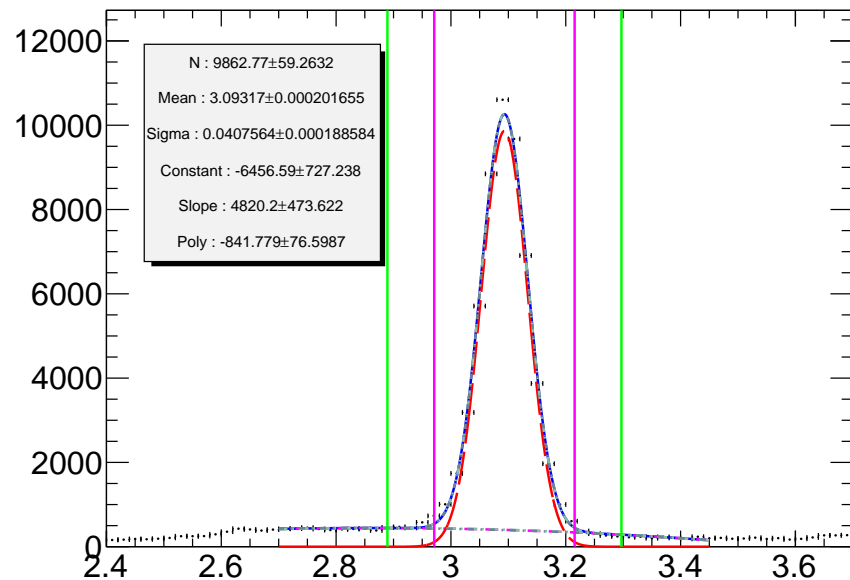
1028 The efficiency is monitored as a function of a variety of kinematic variables, including isolation  
 1029 variables, transverse momentum and angular position of the probe.

### 1030 5.3.1 Isolation dependence

1031 The muons from  $J/\psi$  used in this calibration are produced in isolation, there is very little en-  
 1032 ergetic activity surrounding them in the detector. In contrast muons from semileptonic decay  
 1033 of  $b$ -quarks in  $t\bar{t}$  events are produced amongst the numerous components of the  $b$ -jets. Thus it  
 1034 is important to ensure that the performance of the  $\chi^2_{\text{match}}$  tagger is not affected by the isolation  
 1035 of the muon for a calibration on  $J/\psi$  events to be applicable. In this calibration as, in the 2011  
 1036 analysis nine isolation variables are considered. The so-called etcone20, 30 and 40 correspond  
 1037 to the transverse energy surrounding the muon in a cone of size  $\Delta R=0.2, 0.3$  and  $0.4$  respec-



(a) Probe level



(b) Muon probe level

Figure 5.3: Invariant mass distributions of tag and probe pairs at a) probe level and at b) muon probe level in collision data. Note the various components of the fit as well as the variations on the background fits and the  $3\sigma$  and  $5\sigma$  integration windows used for systematics. Note the fit parameters and their respective uncertainties

tively. Additionally ptcone20, 30 and 40 and nucone20, 30 and 40 correspond to the sum of transverse momentum and the number of tracks surrounding the muon, respectively. All nine isolation variables exclude the muon itself in a cone of size 0.1 and include various corrections for known energy losses, momentum leakages between adjacent clusters in the detector and the effects of pile-up.

As in the 2011 analysis there appears to be no dependence of the scale factor on any of the isolation variables examined as can be seen from Figures 5.4, 5.5 and 5.6.

The dependence on each isolation variable is measured in a range dictated by the available statistics. Given the isolated nature of muons in  $J/\psi$  events limits the number of muons available at higher pt/et/nucone values.

### 5.3.2 2011 Calibration

#### 5.3.3 Efficiency Binning

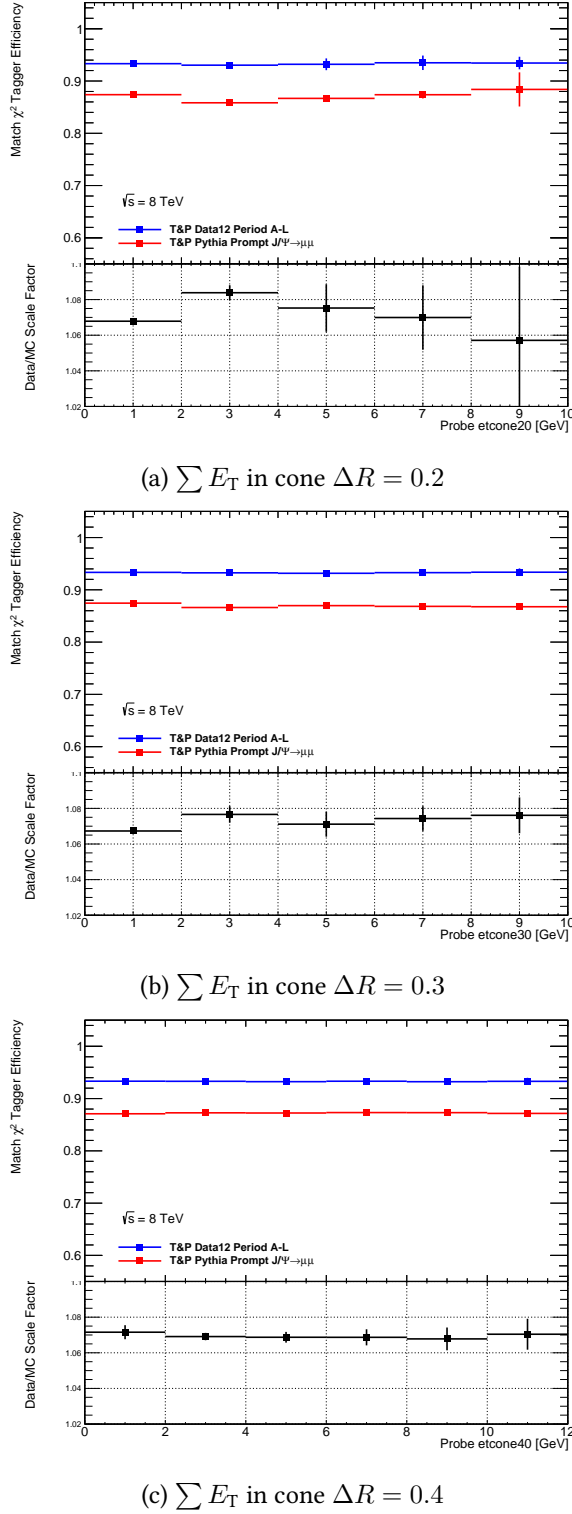
The efficiencies are measured with respect to pseudorapidity and across the  $|\eta|$  range of the ATLAS detector in regions defined in Table 5.1. Note that the pseudorapidity regions are labeled A and C to denote the positive and negative  $\eta$  sections of the detector. The binning in other variables is determined by the amount of statistics available to allow for the fitting procedure to produce good and stable results. The binning in  $p_T$  was chosen as: 4–5, 5–6, 6–7, 7–8, 8–10, 10–12, 12–14, 14–16 and 16–20 GeV.

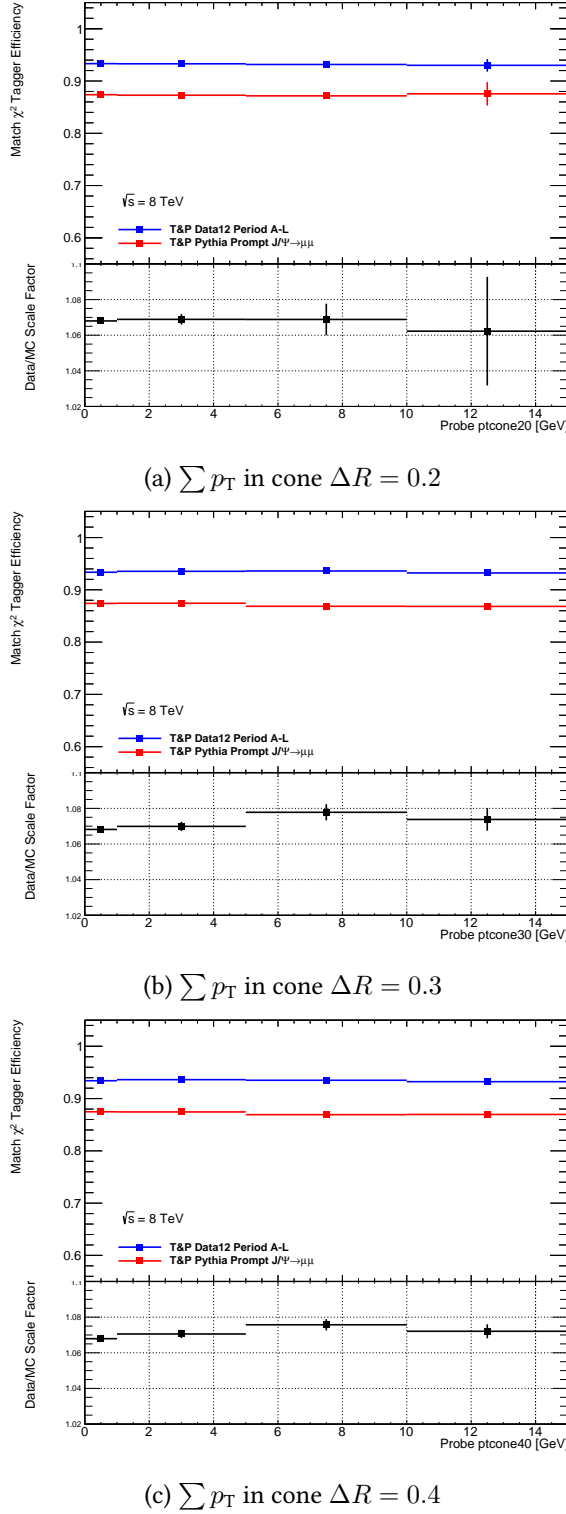
Table 5.1: Pseudorapidity regions of the ATLAS detector

$ \eta $ range	Name
$0.0 <  \eta  < 0.1$	Crack
$0.1 <  \eta  < 1.1$	Barrel
$1.1 <  \eta  < 1.3$	Transition
$1.3 <  \eta  < 2.0$	Endcap
$2.0 <  \eta  < 2.5$	Forward

#### 5.3.4 Results

The efficiency is presented as a function of  $\eta$ ,  $\phi$  and  $p_T$ . Figure 5.7 shows the  $\chi^2_{\text{match}}$  efficiency with respect to the spatial variables of the probe. Note that as with the 2011 analysis the efficiency exhibits no dependence on  $\phi$  and an asymmetric dependence on  $\eta$  particularly in

Figure 5.4:  $\chi^2_{\text{Dof}}$  efficiencies and scale factor with respect to  $\sum E_T$ .

Figure 5.5:  $\chi^2_{\text{DoF}}$  efficiencies and scale factor with respect to  $\sum p_T$ .

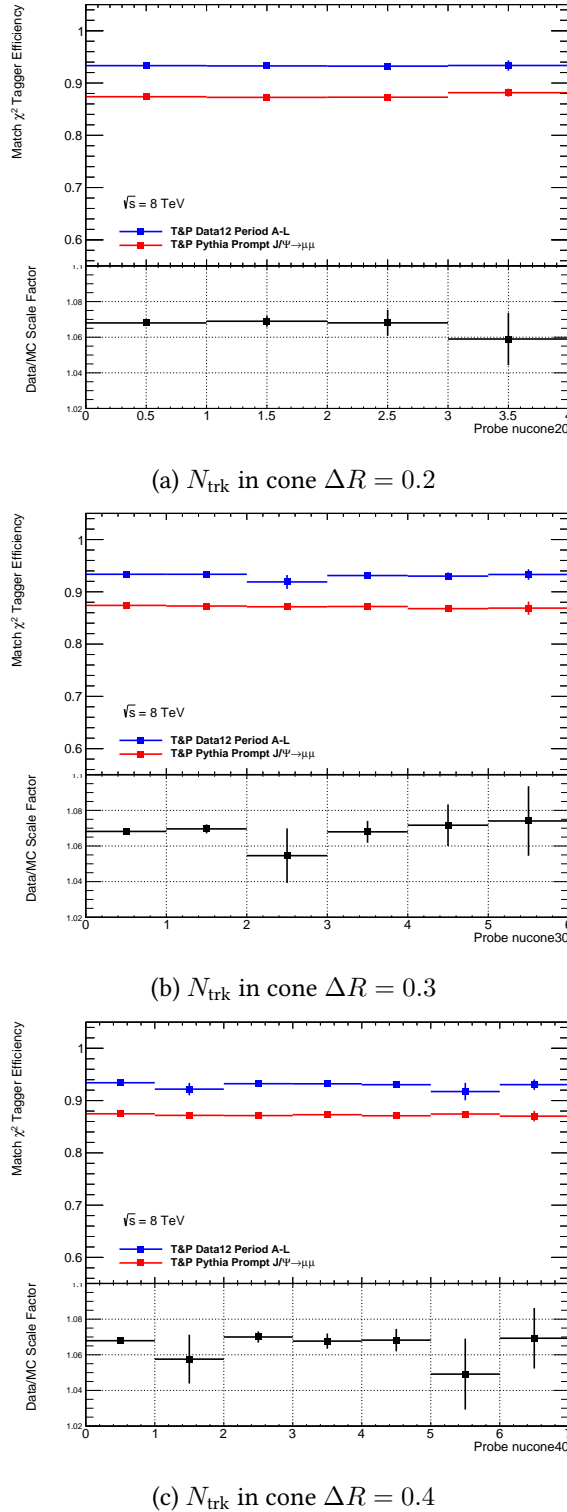


Figure 5.6:  $\chi^2_{\text{DoF}}$  efficiencies and scale factor with respect various isolation variables.

1060 the Forward regions of the detector. Note that as expected there is a strong dependence on  
 1061 the transverse momentum of the muon probe as shown in Fig.5.8. As in the 2011 analysis it  
 1062 was decided to bin the scale factor as a function of  $\eta$  and  $p_T$ . The scale factors and efficiencies  
 1063 are presented in the next pages. The scale factors and their uncertainties are summarized in  
 1064 Table 5.2.

Table 5.2: Data/MC Scale Factors for 2012 Data in all five regions of the detector as a function of  $p_T$ . The uncertainties include systematic and statistical components as described in Section 5.2.1

Side A (Positive $\eta$ )					
$p_T$ range	Crack A	Barrel A	Transition A	Endcap A	Forward A
4-5 GeV	$1.051 \pm 0.016$	$1.053 \pm 0.005$	$1.046 \pm 0.019$	$1.061 \pm 0.011$	$1.090 \pm 0.018$
5-6 GeV	$1.050 \pm 0.007$	$1.058 \pm 0.004$	$1.057 \pm 0.019$	$1.062 \pm 0.011$	$1.103 \pm 0.020$
6-7 GeV	$1.068 \pm 0.008$	$1.065 \pm 0.003$	$1.070 \pm 0.015$	$1.065 \pm 0.008$	$1.134 \pm 0.019$
7-8 GeV	$1.061 \pm 0.018$	$1.063 \pm 0.006$	$1.064 \pm 0.017$	$1.061 \pm 0.010$	$1.140 \pm 0.024$
8-10 GeV	$1.061 \pm 0.014$	$1.063 \pm 0.007$	$1.068 \pm 0.016$	$1.052 \pm 0.014$	$1.167 \pm 0.023$
10-12 GeV	$1.060 \pm 0.042$	$1.070 \pm 0.006$	$1.064 \pm 0.026$	$1.058 \pm 0.016$	$1.175 \pm 0.038$
12-14 GeV	$1.061 \pm 0.050$	$1.064 \pm 0.010$	$1.067 \pm 0.037$	$1.057 \pm 0.021$	$1.190 \pm 0.057$
14-16 GeV	$1.062 \pm 0.087$	$1.068 \pm 0.015$	$1.078 \pm 0.054$	$1.067 \pm 0.031$	$1.218 \pm 0.064$
16-20 GeV	$1.062 \pm 0.087$	$1.068 \pm 0.015$	$1.078 \pm 0.054$	$1.067 \pm 0.031$	$1.218 \pm 0.064$

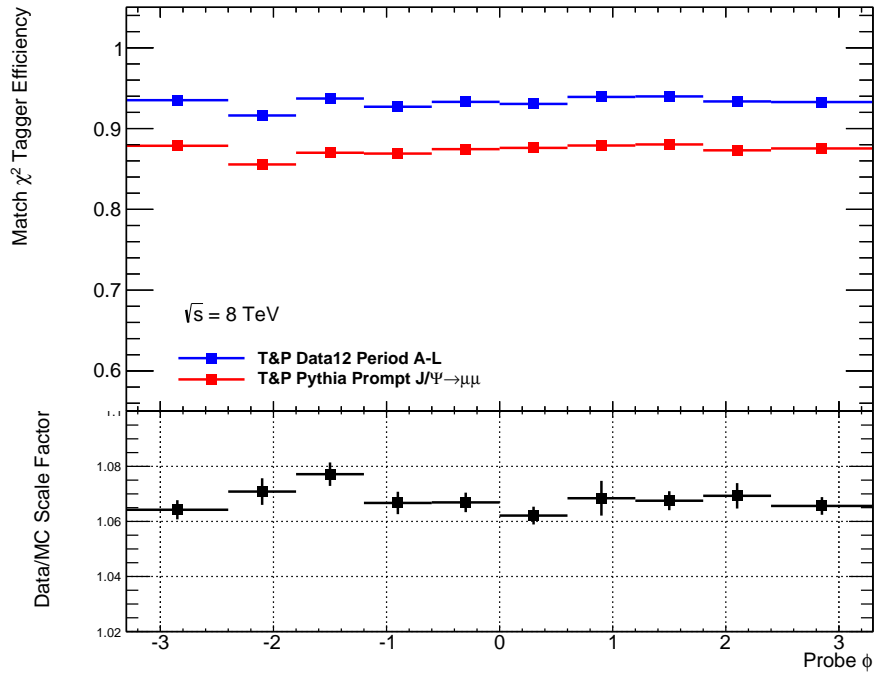
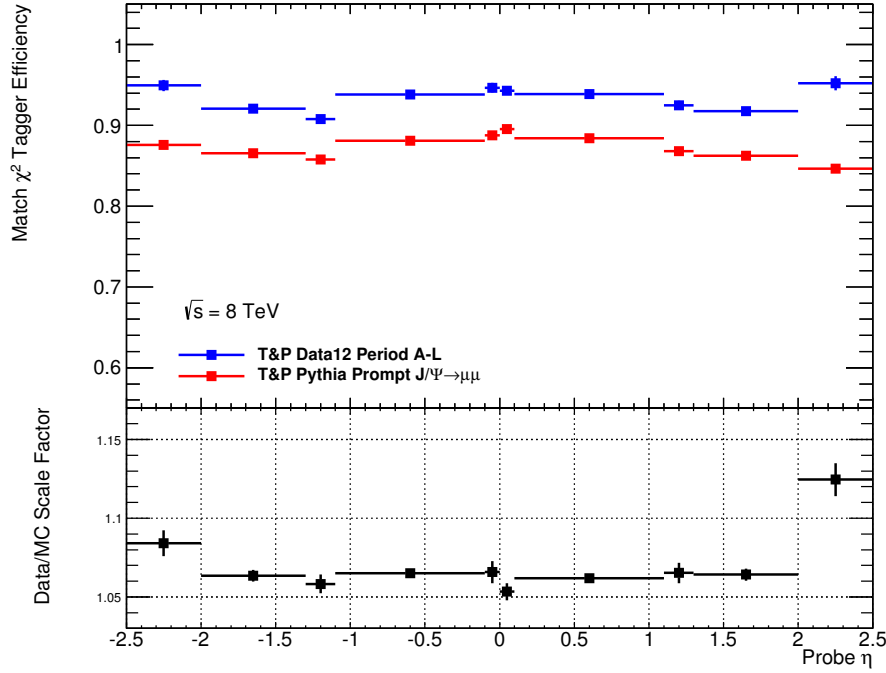
(a) For the positive  $\eta$  regions

Side C (Negative $\eta$ )					
$p_T$ range	Crack	Barrel	Transition	Endcap	Forward
4-5 GeV	$1.044 \pm 0.016$	$1.055 \pm 0.005$	$1.054 \pm 0.017$	$1.056 \pm 0.009$	$1.068 \pm 0.018$
5-6 GeV	$1.069 \pm 0.013$	$1.057 \pm 0.004$	$1.050 \pm 0.016$	$1.062 \pm 0.010$	$1.084 \pm 0.020$
6-7 GeV	$1.080 \pm 0.016$	$1.068 \pm 0.004$	$1.065 \pm 0.008$	$1.066 \pm 0.008$	$1.089 \pm 0.018$
7-8 GeV	$1.064 \pm 0.021$	$1.068 \pm 0.004$	$1.063 \pm 0.016$	$1.066 \pm 0.010$	$1.095 \pm 0.022$
8-10 GeV	$1.071 \pm 0.015$	$1.067 \pm 0.005$	$1.045 \pm 0.015$	$1.061 \pm 0.009$	$1.107 \pm 0.022$
10-12 GeV	$1.084 \pm 0.030$	$1.073 \pm 0.007$	$1.085 \pm 0.022$	$1.061 \pm 0.015$	$1.113 \pm 0.036$
12-14 GeV	$1.098 \pm 0.067$	$1.069 \pm 0.010$	$1.059 \pm 0.031$	$1.040 \pm 0.024$	$1.108 \pm 0.055$
14-16 GeV	$1.063 \pm 0.101$	$1.073 \pm 0.015$	$1.076 \pm 0.046$	$1.061 \pm 0.030$	$1.099 \pm 0.057$
16-20 GeV	$1.073 \pm 0.149$	$1.088 \pm 0.006$	$1.099 \pm 0.028$	$1.054 \pm 0.012$	$1.117 \pm 0.043$

(b) For the negative  $\eta$  region

### 1065 Dependence on $d_0$

1066 The dependence on the impact parameter  $d_0$  was examined and no direct dependence is ob-  
 1067 served. From Fig. 5.14 the scale factor shows no structure with respect to  $d_0$  when binned in  
 1068  $p_T$ . Since the scale factors are already binned in  $\eta$  and  $p_T$  the correlation of  $d_0$  and  $p_T$  is already

(a)  $\chi^2_{\text{match}}$  efficiency and scale factor as a function  $\phi$  of the probe muon(b)  $\chi^2_{\text{match}}$  efficiency and scale factor as a function  $\eta$  of the probe muonFigure 5.7:  $\chi^2_{\text{match}}$  efficiencies and scale factor with respect to the (a)  $\phi$  and (b)  $\eta$

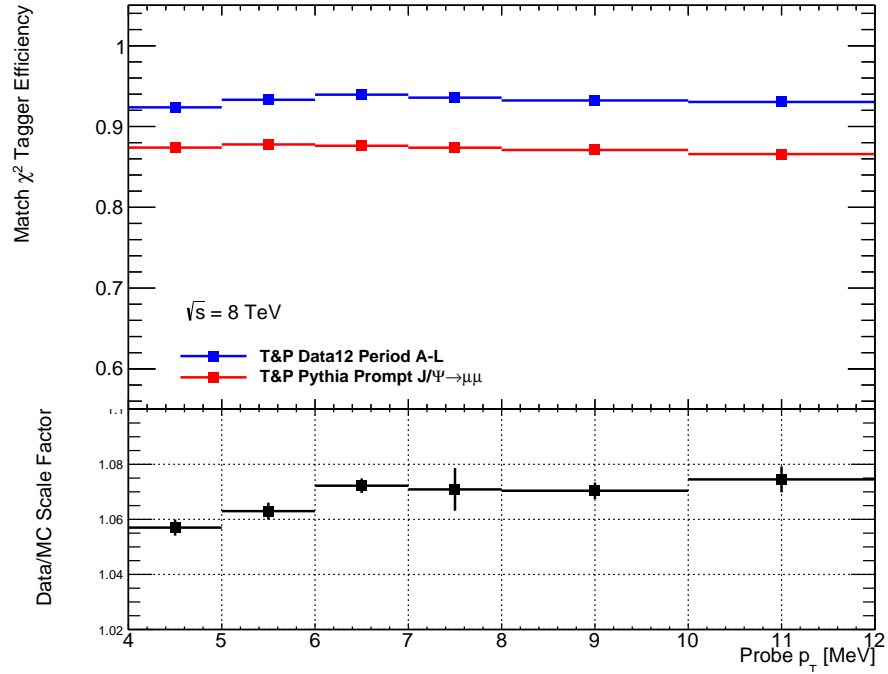


Figure 5.8:  $\chi^2_{\text{match}}$  efficiencies and scale factor with respect to the transverse momentum of the muon probe

$^{1069}$  taken into account.

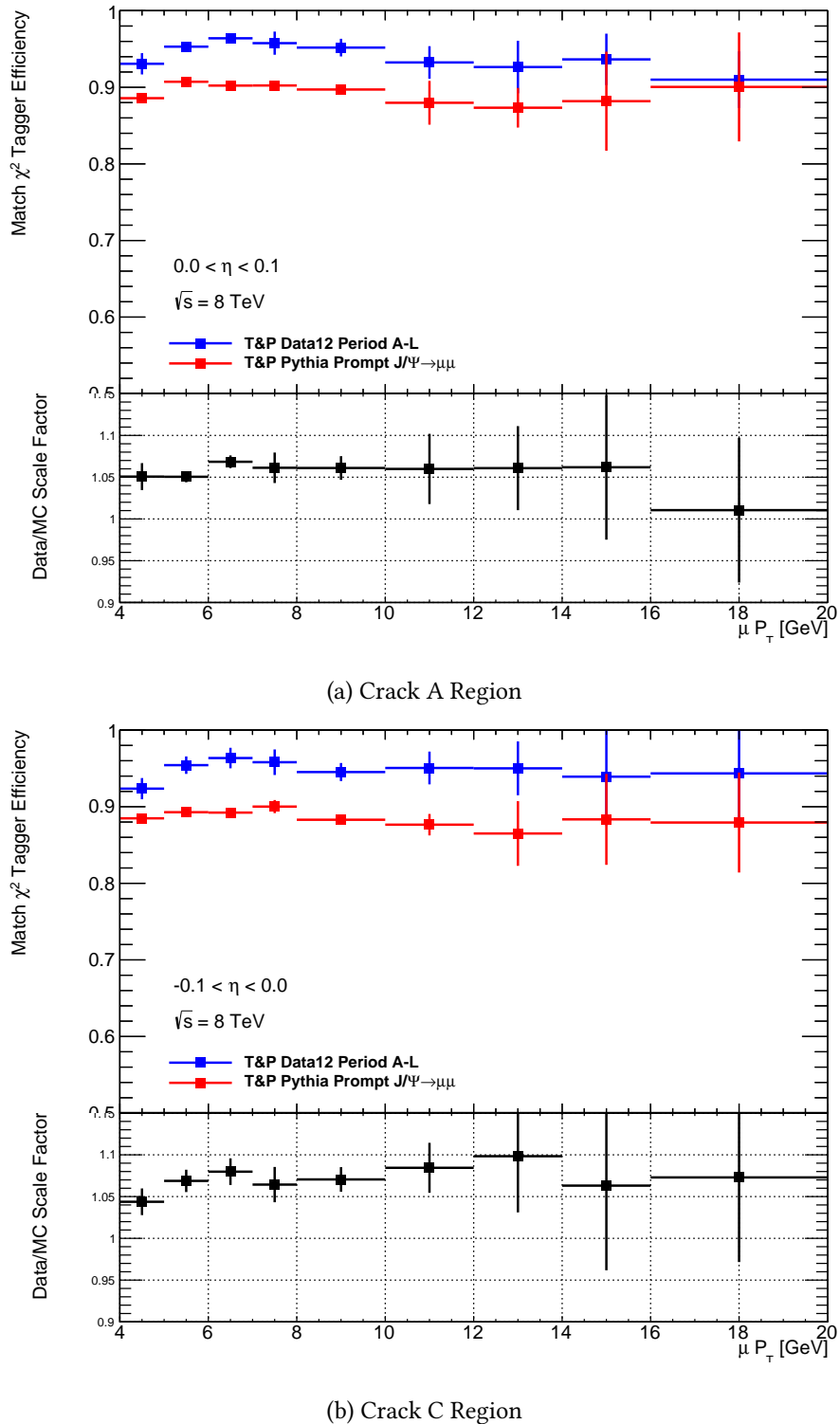


Figure 5.9:  $\chi^2_{\text{match}}$  efficiencies and scale factors in the crack region of the detector for side (a) A and (b) C

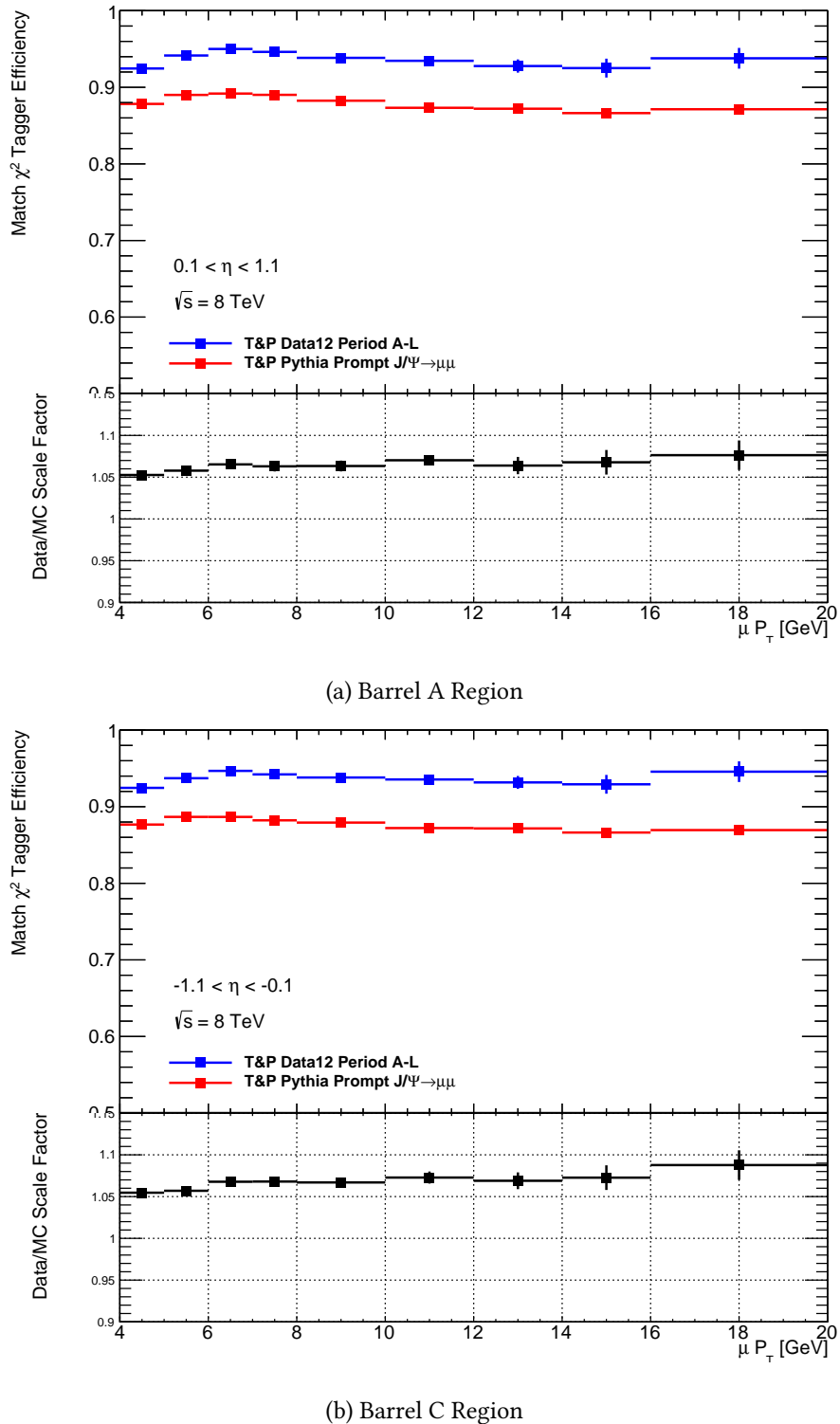


Figure 5.10:  $\chi^2_{\text{match}}$  efficiencies and scale factors in the barrel region of the detector for side (a) A and (b) C

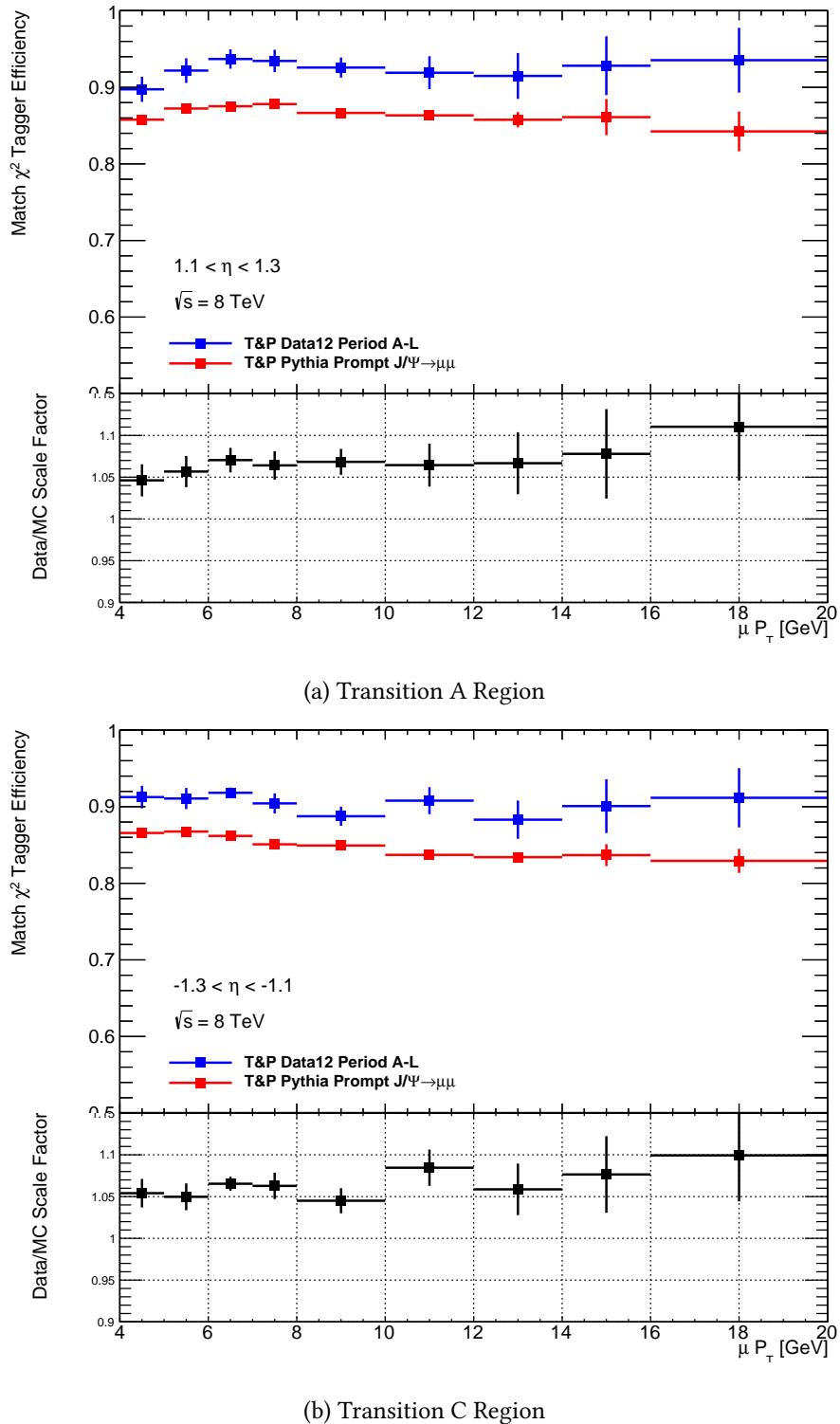


Figure 5.11:  $\chi^2_{\text{match}}$  efficiencies and scale factors in the transition region of the detector for side (a) A and (b) C

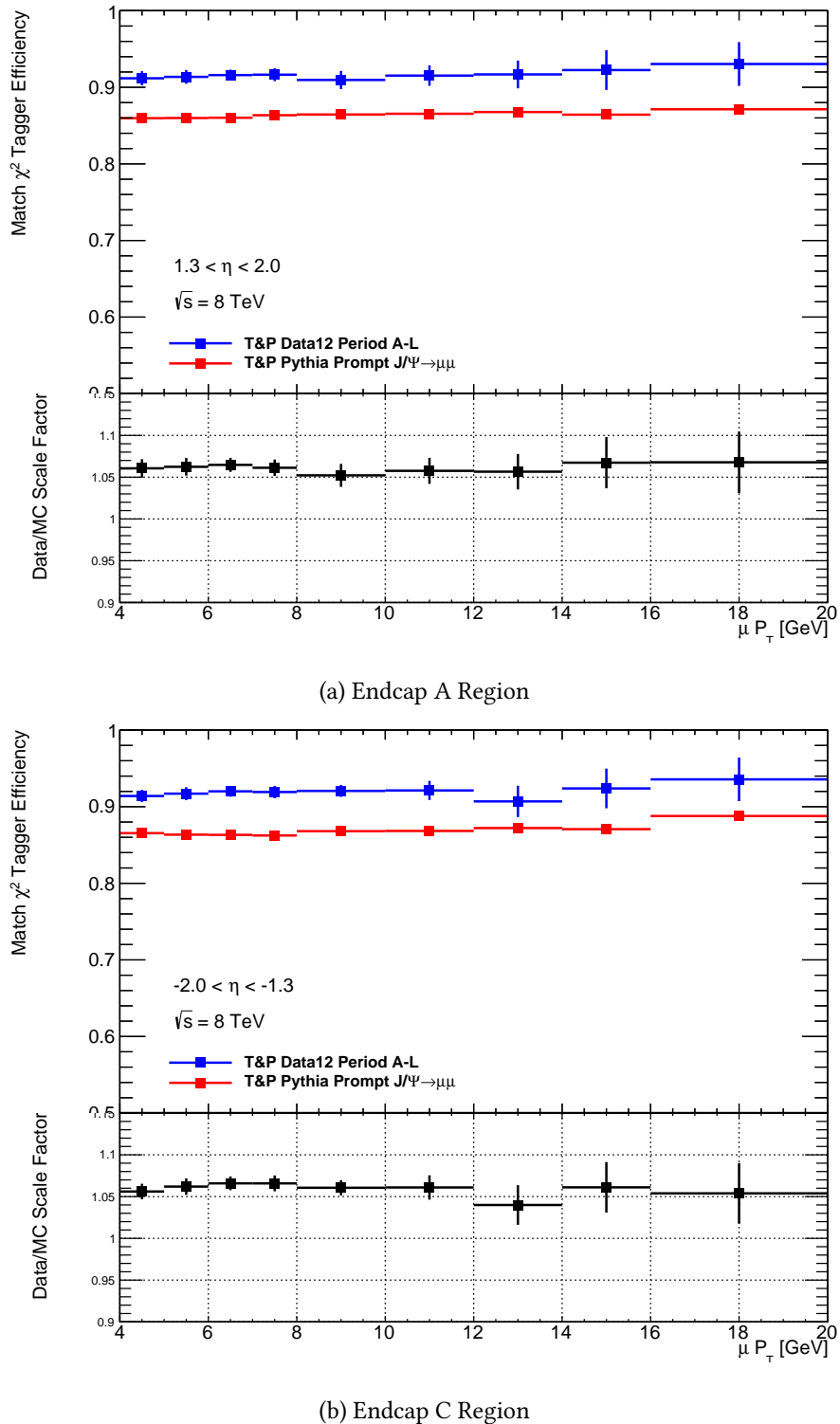


Figure 5.12:  $\chi^2_{\text{match}}$  efficiencies and scale factors in the endcap region of the detector for side (a) A and (b) C

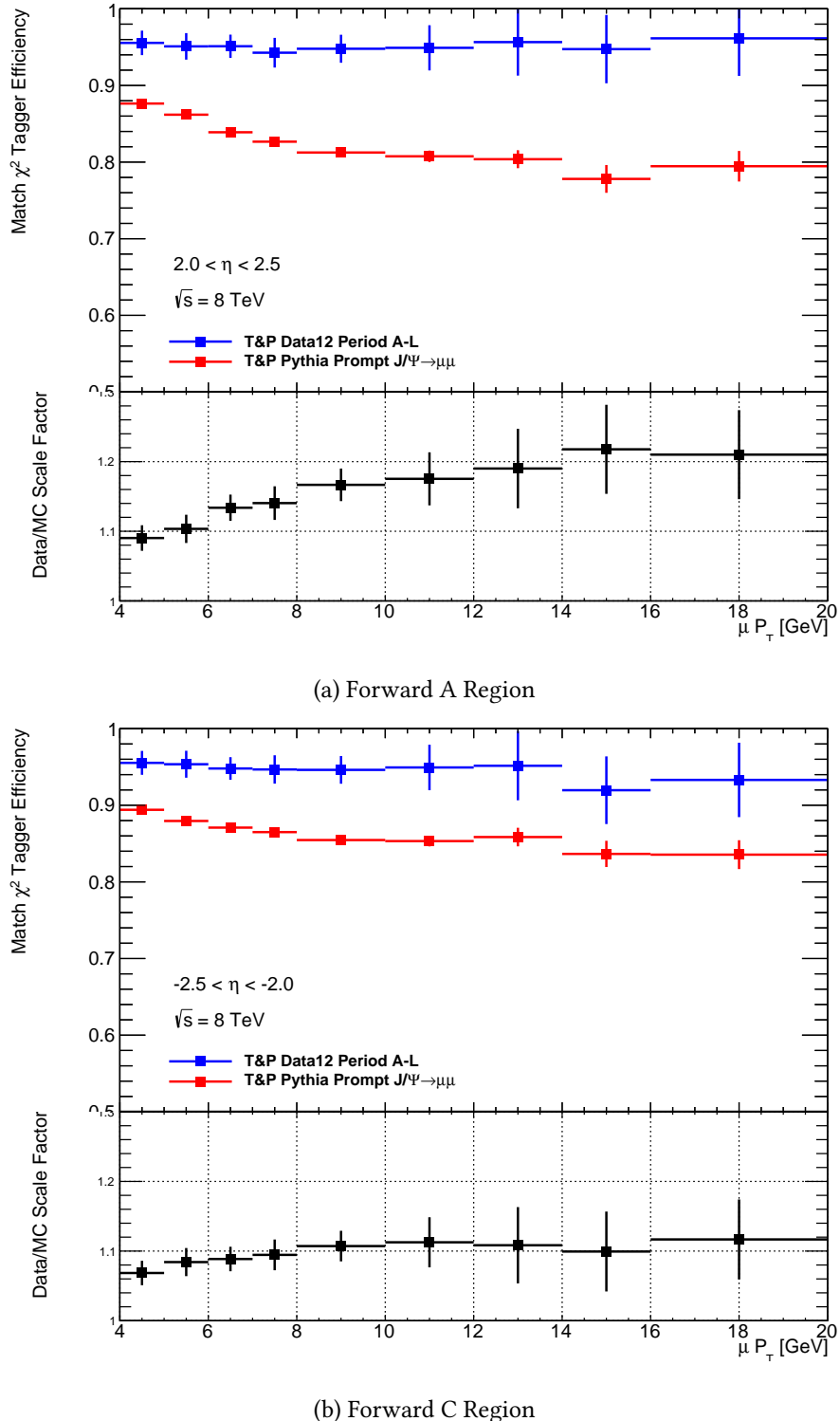


Figure 5.13:  $\chi^2_{\text{match}}$  efficiencies and scale factors in the forward region of the detector for side (a) A and (b) C

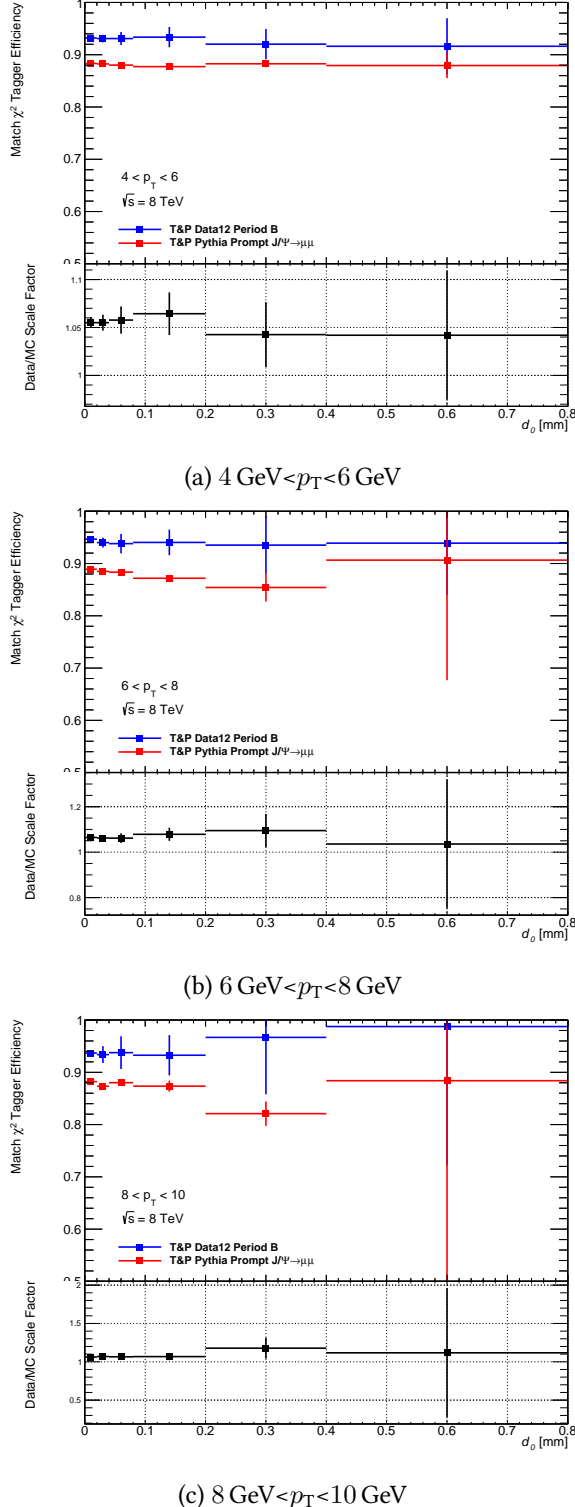


Figure 5.14:  $\chi^2_{\text{match}}$  efficiencies and scale factor with respect to impact parameter  $d_0$  for muon probes with  $p_T$  in the range (a) 4–6 GeV, (b) 6–8 GeV and (c) 8–10 GeV. The measurement was carried out only on Period B of 2012 ATLAS collision data.

1070 **Chapter 6**

1071 **Measurement of the  $t\bar{t}$  cross-section  
1072 in the  $\ell$ +jets channel using SMT**

1073 This section describes a  $t\bar{t}$  cross-section measurement carried out the joint RHUL-QMUL SMT  
1074 group.

1075 Measurement of the  $t\bar{t}$  production cross-section is important for two reasons. First, the  
1076 value of the  $t\bar{t}$  cross-section is a powerful test of the SM and perturbative QCD. Additionally,  
1077  $t\bar{t}$  events constitute a background to other analyses such as SUSY searches and Higgs boson  
1078 searches and properties studies. Presented here is a measurement of the top-pair production  
1079 cross-section at  $\sqrt{s} = 7\text{TeV}$  in the lepton plus jets channel, with at least one of the  $b$ -quarks in  
1080 the event decaying semileptonically producing a soft muon.

1081 **6.1 Soft Muon Tagger**

1082 **6.2 Data and Monte Carlo samples**

1083 **6.3 Object selection and event selection**

1084 The selection criteria used in this analysis are based on the nominal  $\sqrt{s} = 7\text{TeV}$  selections  
1085 constructed by the ATLAS top group. Some alterations have been implemented to adapt to the  
1086 usage of the  $\chi^2_{\text{match}}$ -tagger instead of the standard MV1 method for  $b$ -jet tagging.

1087 **6.4 Background estimation**

1088 Semi-leptonic  $t\bar{t}$  events have a varied final state signature that includes a lepton, multiple jets  
 1089 including  $b$ -jets and missing energy. As a result  $t\bar{t}$  analyses must take into account many dif-  
 1090 ferent types of background including diboson,  $W$ +jets,  $Z$ +jets, single-top and multijet. Data-  
 1091 driven methods are used for the dominant multijet and  $W$ +jets backgrounds while MC is used  
 1092 to estimate the smaller  $Z$ +jets, diboson and single-top.

1093 **6.4.1 Multijet in the electron channel**

1094 The multijet background is a difficult background to reduce and estimate. Measurement of  
 1095 multijet events depends very strongly on detector conditions, which in turn depend on external  
 1096 factors which cannot be simulated. Multijet events that pass the event selection include non-  
 1097 isolated or misidentified electrons from photon conversion or charged hadrons. As a result,  
 1098 data-driven methods must be employed when estimating the amount of multijet background.  
 1099 This analysis makes use of two different methodologies, The so-called matrix method is used for  
 1100 the central value of the estimate and the ABCD method for verification and use as a systematic.

At pretag level the multijet content in the signal region is estimated by using the matrix method. In addition to the standard electron selection a looser selection is defined. Events are categorized by whether they pass the loose or standard selection. The number of events in each category is the sum of events with “real” electrons and “fake” electrons as follows:

$$N^{\text{loose}} = N_{\text{real}}^{\text{loose}} + N_{\text{fake}}^{\text{loose}}$$

$$N^{\text{std}} = rN_{\text{real}}^{\text{loose}} + fN_{\text{fake}}^{\text{loose}}$$

where  $r$  and  $f$  are the “real” and “fake” efficiencies for the loose event to also pass the standard selection. Given a measured  $N^{\text{std}}$  and  $N^{\text{loose}}$  and if  $f$  and  $r$  are known the number of events with a fake electron that passes the standard selection can be calculated as

$$N_{\text{fake}}^{\text{std}} = fN_{\text{fake}}^{\text{loose}} = f \frac{N^{\text{std}} - rN^{\text{loose}}}{(f - r)}$$

1101 The relative efficiency  $r$  is measured from an inclusive sample of  $Z \rightarrow ee$  events and  $f$   
 1102 is measured from a sample of events with exactly one loose electron, at least one jet with a

<sup>1103</sup>  $p_T > 25 \text{ GeV}$  and  $\cancel{E}_T < 20 \text{ GeV}$ . An uncertainty of 50% is assigned to the pretag estimate to  
<sup>1104</sup> cover the respective uncertainties on  $f$  and  $r$ .

<sup>1105</sup> To derive the tagged estimate the pretag estimates are scaled by the probability of SMT  
<sup>1106</sup> tagging an event. The tagging probability of multijet events  $R_{\text{SMT}}^{\text{multijet}}$  is derived from control  
<sup>1107</sup> regions defined by the isolation of the electron and the  $\cancel{E}_T$  cut that forms part of the event  
<sup>1108</sup> selection, as shown in Figure 6.1.

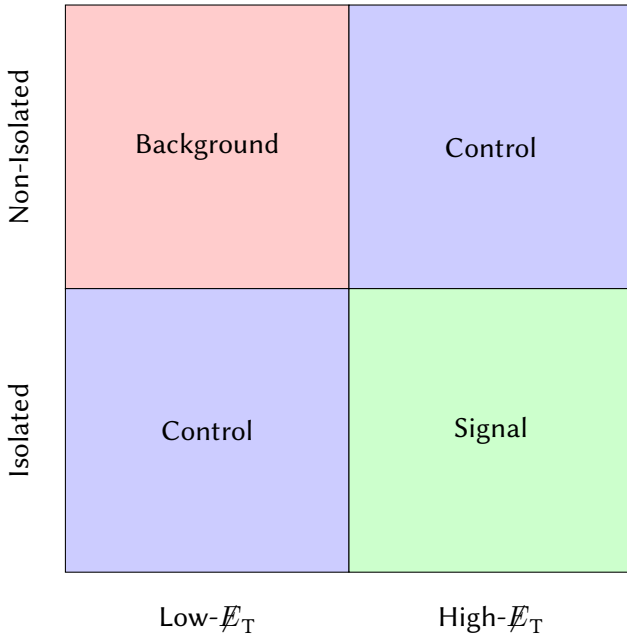


Figure 6.1: A diagram of the  $\cancel{E}_T$ -isolation phase space. Shown are the four regions as defined by the event selection.

These four regions can be identified as a background-dominated region, containing events with low- $\cancel{E}_T$  and a non-isolated electron; a signal region, with events that pass the event selection; and two control regions, containing events with high- $\cancel{E}_T$  or an isolated electron. The events in each of the regions then represent a different type of phenomenon. The tagging rate is simply defined as

$$R_{\text{SMT}} = \frac{N_{\text{Tagged}}}{N_{\text{Pretag}}}$$

where  $N$  is the number of events in the region. Contributions from other processes such as  $W+\text{jets}$ ,  $Z+\text{jets}$ ,  $t\bar{t}$ , single-top and diboson events are subtracted using MC simulation. Thus

the yield in each region is defined as

$$N^{\text{multijet}} = N^{\text{data}} - N^{W+\text{jets}} - N^{Z+\text{jets}} - N^{\text{diboson}} - N^{t\bar{t}} - N^{\text{single-top}}$$

1109     The contribution from  $t\bar{t}$  is initially based on the theoretical cross-section, an estimate  
 1110    for the multijet contribution is determined using this cross-section and a new measured cross-  
 1111    section is obtained. The measured cross-section is used to rescale the  $t\bar{t}$  contribution and a new  
 1112    cross-section is obtained. This process is repeated until the measured cross-section stabilizes  
 1113    after two iterations.

1114     The uncertainty on the tagging-rate contains statistical and a systematic contributions.  
 1115    The systematic uncertainty includes the uncertainty on the cross-section of the  $t\bar{t}$  and  $W+\text{jets}$   
 1116    samples, uncertainty arising from the SMT tagger and finally uncertainties arising from the BR  
 1117    re-weighting described a priori.

1118     The final tagging-rate is the unweighted average of all the regions. The uncertainty is  
 1119    the difference between regions A and C, as this is larger than any regional uncertainty. The  
 1120    tagging-rate and subsequently the tagged multijet background estimate is measured on a per-  
 1121    jet bin basis. The tagging-rates per region for each jet-bin are shown in Table 6.1.

Jet-bin	$R_A^{\text{SMT}}$	$R_B^{\text{SMT}}$	$R_C^{\text{SMT}}$	$R_{AVG}^{\text{SMT}}$
1	$0.91 \pm 0.03$	$0.82 \pm 0.10$	$0.51 \pm 0.05$	$0.64 \pm 0.07$
2	$1.8 \pm 0.1$	$2.0 \pm 0.2$	$1.3 \pm 0.1$	$1.5 \pm 0.1$
3	$2.8 \pm 0.1$	$2.5 \pm 1.1$	$2.5 \pm 0.5$	$2.6 \pm 1.0$
$\geq 3$	$3.84 \pm 0.09$	$3.7 \pm 1.3$	$3.0 \pm 0.8$	$3.2 \pm 1.2$
$\geq 4$	$3.2 \pm 0.1$	$3.7 \pm 1.3$	$3.0 \pm 0.8$	$3.2 \pm 1.2$

Table 6.1: Multijet SMT event taggin-rate(in percent) in regions A) inverted- $E_T$ , non-isolated,  
 B) High- $E_T$ , non-isolated and C) low- $E_T$ , isolated.

Jet-bin	Pretag	Tagged
1	$51000 \pm 26000$	$330 \pm 160$
2	$26000 \pm 13000$	$400 \pm 200$
3	$8100 \pm 4100$	$210 \pm 130$
$\geq 3$	$10800 \pm 5400$	$330 \pm 210$

Table 6.2: Multijet estimates in the e+jets obtained by the jet-electron method. The uncertainties are combined statistical and systematics. A systematic uncertainty of 50% is used on the jet-electron pretag event yields [5] in addition to e uncertainties obtained on  $R_{WGT}^{\text{SMT}}$ .

1122 **The ABCD method**

1123 The ABCD method relies on a pair of uncorrelated variables to extrapolate the amount of mul-  
 1124 tijet events from a set of control regions into the signal region. First a two-dimensional phase-  
 1125 space is constructed, in this case the same two variables, missing energy and isolation are used.  
 1126 If these two variables are uncorrelated then the following relation holds

$$N_D^{\text{multijet}} = \frac{N_B^{\text{multijet}} * N_C^{\text{multijet}}}{N_A^{\text{multijet}}} \quad (6.1)$$

1127 where  $N_X^{\text{multijet}}$  is the number of multijet events in region X.

1128 This allows for an estimation of the number of multijet events that pass the event selection  
 1129 by extrapolating from the background region into the signal region. As with the matrix method,  
 1130 event contributions from other processes are removed using MC. The uncertainty on the final  
 1131 estimate includes statistical contributions from the yield in each region and the systematic  
 1132 uncertainty on the  $W+\text{jets}$  and  $t\bar{t}$  samples as described.

1133 **6.4.2 Multijet background in the muon channel**

1134 Multijet events contaminate the signal region by producing “fake” isolated muons which are  
 1135 misidentified as signal muons. The main sources of fake muons are semileptonic decay of  
 1136 heavy quarks ( $b/c$ ), muons from the decay in flight of pions and kaons and “punch-through”  
 1137 of hadrons not fully absorbed by the hadronic calorimeter and produce a signal in the muon  
 1138 system.

1139 The procedure in the muon channel is similar to that used for the electron channel. A pretag  
 1140 estimate of the multijet fraction in the signal region is obtained using the matrix method. The  
 1141 “real” muon selection efficiency  $r$  is measured from an inclusive sample of  $Z \rightarrow \mu\mu$  events.  
 1142 The “fake” muon selection efficiency  $f$  is obtained from data using two different methods:

- 1143 • a control region where the  $\cancel{E}_T + \text{ensuremath}m_{T,W}$  cut is inverted and an additional cut  
 1144 of  $\text{ensuremath}m_{T,W} < 20\text{GeV}$  is applied,
- 1145 • and a fit to the transverse impact parameter significance  $\sigma_{d_0}$  distribution where both  
 1146  $\cancel{E}_T + \text{ensuremath}m_{T,W}$  and  $\cancel{E}_T$  cuts are inverted.

1147 The central value of the pretag estimate is obtained from an average of these two regions.  
 1148 A uncertainty of 20% is assigned to the final estimate to account for the uncertainty associated  
 1149 with each region and the difference between them.

1150 The SMT event tagging rate is obtained from two control regions, defined by

- 1151 • inverting the  $\cancel{E}_T$  and  $\cancel{E}_T + \text{ensuremath}_{T,W}$  cuts,  
 1152 • and by inverting the muon isolation requirement.

1153 The sources of uncertainty are the same as those considered in the electron channel.

1154 **6.4.3  $W+\text{jets}$  background**

1155 The  $W+\text{jets}$  background is the most dominant background since these events contain a real  
 1156 lepton and  $\cancel{E}_T$  from the escaping neutrino. Events can be classified into  $W+\text{HF}$ , which is the  
 1157 largest contribution; and  $W+\text{LF}$  where a LF jet is mis-tagged. Due to the significant uncertainty  
 1158 on the overall normalization of  $W+\text{jets}$  and the presence of a mis-tagged LF jet, a data-driven  
 1159 method, known as  $W$  charge asymmetry [37], is used to estimate this background.

1160 The  $W$  charge asymmetry method relies on the observation that the ratio of positive to  
 1161 negative  $W$  bosons suffers from small theoretical uncertainty and thus can provide an overall  
 1162 normalization. Thus the overall normalization is by

$$\begin{aligned} N_{W^+} + N_{W^-} &= \frac{N_{W^+}^{\text{MC}} + N_{W^-}^{\text{MC}}}{N_{W^+}^{\text{MC}} - N_{W^-}^{\text{MC}}} (D^+ - D^-) \\ &= \frac{r_{\text{MC}} + 1}{r_{\text{MC}} - 1} (D^+ - D^-) \end{aligned} \quad (6.2)$$

where  $r_{\text{MC}}$  is the ratio in MC of events with a positive lepton to those with a negative lepton and  $D^\pm$  are the number of events in data with a positive or negative lepton. Contributions from other charge asymmetric processes, namely single-top and diboson are removed using MC simulation. This results in an overall normalization for the  $W+\text{jets}$  background at the pretag level. For the tagged level an event tagging rate is obtained for the  $W+\text{HF}$  and  $W+\text{LF}$  components separately:

$$W_{\text{tag}} = R_{\text{tag}}^{\text{LF}} W_{\text{pretag}}^{\text{LF}} + \sum_{\text{HF}}^{\text{HF}=c,cc,bb} R_{\text{tag}}^{\text{HF}} W_{\text{pretag}}^{\text{HF}}$$

1163 where  $R_{\text{tag}}^{\text{LF}}$  is defined as the probability to mistag a LF event and  $R_{\text{tag}}^{\text{HF}}$  is the probability to  
1164 correctly tag a HF event. The tagging rates are obtained from simulation with the SMT scale  
1165 factors and BR reweighting applied to each tagged jet.

1166 **6.5 Systematic uncertainties**

1167 **6.6 Results and conclusion**

1168 The final cross-section is determined by a cut-and-count method. Finally the cross-section is  
1169 calculated as

$$\sigma_{t\bar{t}} = \frac{N_{\text{data}} - N_{\text{bkg}}}{\int L dt \times \epsilon \times \text{BR}(\text{noFullHad})} \quad (6.3)$$

1170 The cross-section measured in the electron

1171 **Chapter 7**

1172 **Muon Tagging in a boosted  $t\bar{t}$**   
1173 **environment**

1174 The large center-of-mass energies at which collisions occur at the LHC allows for the produc-  
1175 tion of very high mass particles. Several Beyond the SM (BSM) theories predict the existence of  
1176 high mass particles which decay primarily top quark pairs. An example of hypothetical model  
1177 which predict high mass  $t\bar{t}$  resonances is the topcolor assisted technicolor model (TC2), which  
1178 predicts the existence of a leptophobic  $Z'$  boson. The resultant top quark pair provides a well  
1179 understood probe to search for such hypothetical particles.

1180 The  $Z'$  could potentially have a mass on the order of several TeV. As a result their decay  
1181 product would be produced in the detector with very large momentum. These top quarks are  
1182 said to be boosted. In terms of the subsequent top decay, the resultant bottom quark and  $W$   
1183 boson are expected to emerge in a collimated cone. The events thus appear as two large back-  
1184 to-back jets. If the  $W$  decays leptonically, the  $W$  lepton is expected to lie very close to or within  
1185 the  $b$ -jet. If the  $W$  decays hadronically all three jets will appear to merge into a single *fat* jet.

1186 In this chapter the results of a feasibility study conducted to determine the viability of using  
1187 the  $\chi^2_{\text{match}}$  tagger to tag  $W$  muons from boosted top-quark decays is presented and discussed.  
1188 Note that this is in contrast to the cross-section analysis detailed in a previous chapter where  
1189 the muon tagged came from the semileptonic decay of  $b$ -quarks. The boost is expected to be  
1190 related to the mass of the  $Z'$  produced, so a higher mass  $Z'$  would decay into more collimated  
1191 jets. The environment that results is thus very similar to that of a semileptonic  $b$ -decay, a muon

1192 buried inside of a  $b$ -jet.

1193 No evidence for such a resonance has been observed and limits have been placed on the  
1194 production rate of these resonance for various benchmark models. A leptophobic topcolor  $Z'$   
1195 of mass less than 1.74 TeV has been excluded using  $4.7 \text{ fb}^{-1}$  of  $pp$  collision data collected by  
1196 ATLAS with a center-of-mass energy  $\sqrt{s} = 7 \text{ TeV}$  [38]. Additionally a more recent analysis  
1197 using  $14.3 \text{ fb}^{-1}$  of  $\sqrt{s} = 8 \text{ TeV}$  data collected at ATLAS excluded a  $Z'$  with a mass less than  
1198 1.8 TeV at 95% confidence level [39]. The analysis detailed here is based on the 7 TeV analysis.  
1199 Similar analyses performed with data collected by CMS have excluded  $Z'$  candidates for similar  
1200 benchmark models [40–42].

1201 The performance of SMT is compared to the contemporary method for selecting muons  
1202 known as mini-isolation. In addition a short performance study to determine the viability of  
1203 using SMT to tag  $b$ -jets in boosted top events is also presented. Firstly, a short examination of  
1204 the topology of a boosted event is presented.

## 1205 7.1 Data samples

1206 This measurement is based on simulated data generated for a  $Z'$  with a mass of 1.0, 1.3, 1.6,  
1207 2.0, 2.5 and 3.0 TeV. All Monte Carlo (MC) samples were generated using PYTHIA [43] with  
1208 CTEQ6LI [44] PDFs<sup>1</sup>. The width of the generated  $Z'$  is 3% of the mass.

1209 The analysis is based on the underlying event information created by the simulation soft-  
1210 ware. This includes the kinematic information of particles in the event as well as the child-  
1211 parent connection between particles. For example the  $Z'$  has two daughter particles associated  
1212 with it, the top and antitop. The decay chain continues with the  $W$  bosons and  $b$  quarks. By  
1213 navigating up or down this chain it is possible to ascertain the origin of a given particle. The  
1214 truth information represents the state of various particles without the effects of the detector,  
1215 that is the  $p_T$  of a given truth particle is not affected by detector resolution for example.

## 1216 7.2 Boosted event topology

1217 In order to perform an effective feasibility study, it is important to understand the signature  
1218 left by boosted events in the detector. There are certain expectations regarding the momentum

---

<sup>1</sup>Parton Distribution Function which describes the relative density of gluon and quarks in the colliding hadrons.

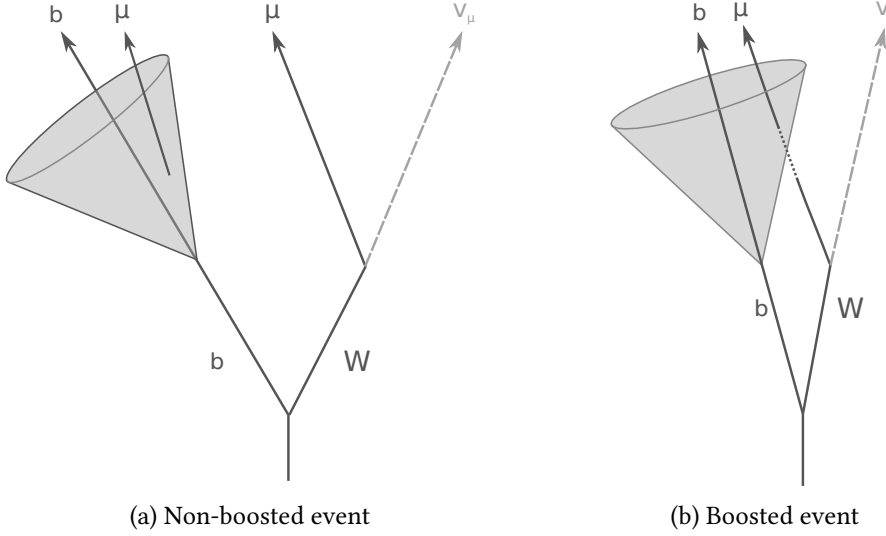


Figure 7.1: This figure shows a simple diagram for the possible configuration of final-state objects in a (a) boosted and (b) non-boosted events. Note that in both cases a muon is embedded within the  $b$ -jet

1219 distribution of the various product particles from the decay of the top as well as their angular  
 1220 separation. As with the cross-section analysis presented in Chapter 6, this study focuses on  
 1221 the semileptonic decays of top quark pairs.

1222 It is expected for events where the momentum of the top quarks higher to exhibit stronger  
 1223 collimation between the  $W$  muon and the  $b$ -quark. This results in a situation very similar to  
 1224 that exploited for muon tagging in Section 6 where a muon from the semileptonic decay of a  
 1225  $b$ -quark emerges from within the  $b$ -jet. Figure 7.1 illustrates the similarity of both scenarios.  
 1226 It is thus possible to use the  $\chi^2_{\text{match}}$ -tagger<sup>2</sup> to tag  $W$  muons in boosted events. As the tagger  
 1227 is designed to work in energetically “busy” sectors of the detector, it is ideally suited to probe  
 1228 highly boosted events where the decay products are collimated.

1229 As can be seen from Figure 7.2 the increase in boost does result in the  $W$  muon and  
 1230  $b$ -quark emerging closer. Note that the fraction of events below the SMT requirement of  
 1231  $\Delta R(\mu, \text{jet}) < 0.5$  increases with increased top-quark  $p_T$ . Additionally Figure 7.3 shows that  
 1232 the top  $p_T$  distribution peaks at just below half of the mass of the  $Z'$  boson, thus the large

<sup>2</sup>As signal muons are very hard, the tagger is now referred to as the  $\chi^2_{\text{match}}$ -tagger not soft muon tagger to reflect this difference

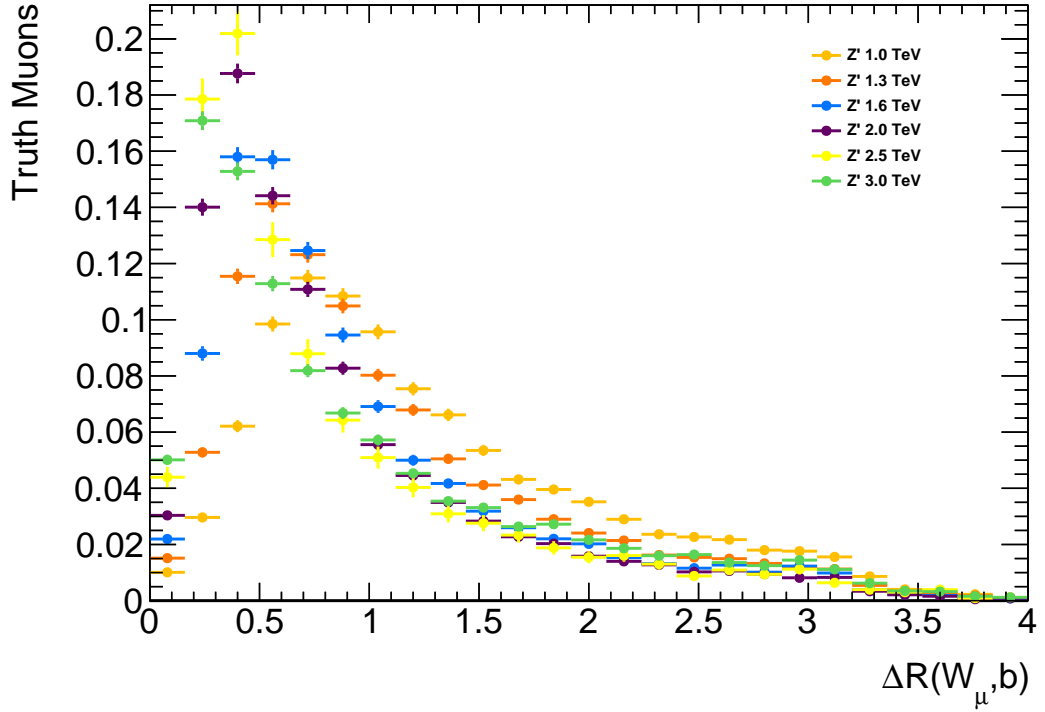


Figure 7.2: The angular separation ( $\Delta R$ ) between the truth  $W$  muon and the corresponding  $b$ -quark for all examined  $Z'$  mass points.

<sub>1233</sub> portion of the candidate muons in the sample will pass the aforementioned separation require-  
<sub>1234</sub> ment. The decay products of the top quark appear to emerge primarily back to back as seen in  
<sub>1235</sub> Figure 7.4. c..

### <sub>1236</sub> 7.3 Signal muon selection

#### <sub>1237</sub> 7.3.1 Muon selection

<sub>1238</sub> The nominal muon object selection includes an isolation requirement, which normally removes  
<sub>1239</sub> events where the signal lepton is found in a region of the calorimeter with large amounts of  
<sub>1240</sub> activity. Cutting on the amount of energy deposited in the calorimeter around the lepton is an  
<sub>1241</sub> example of one such requirement. Such a cut forms part of the object selection used in the top  
<sub>1242</sub> cross-section measurement described in Chapter 5.

<sub>1243</sub> However, as described a priori, boosted top events result in large collimated jets which  
<sub>1244</sub> include the products of the two top quarks. Thus the signal lepton can emerge within the cone

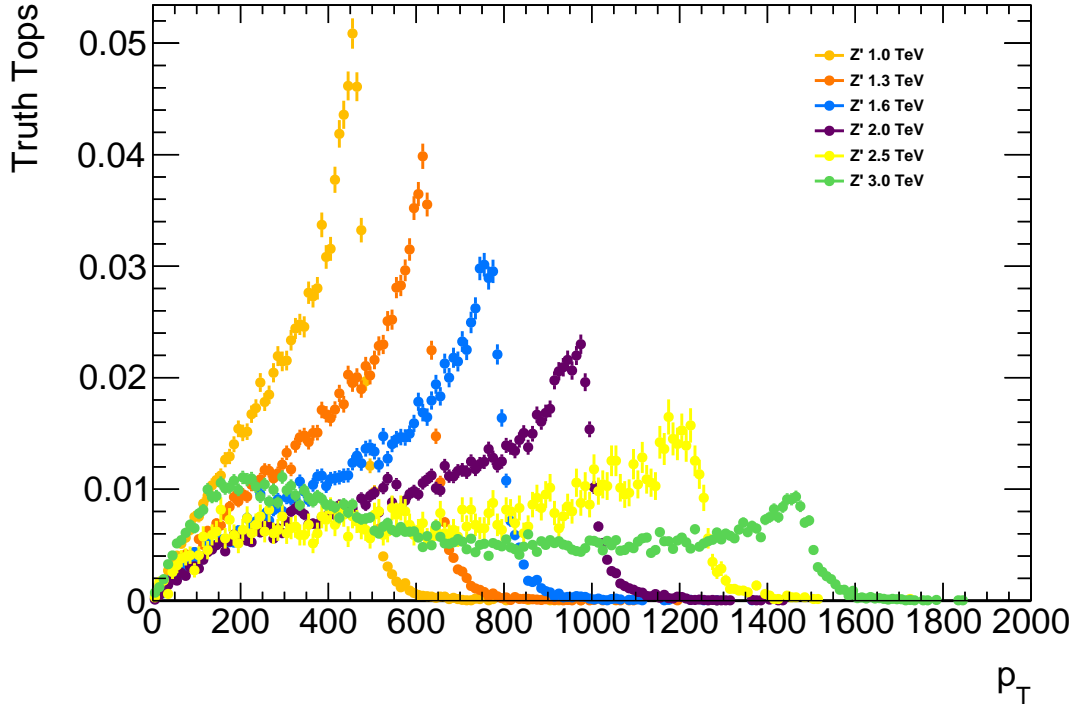


Figure 7.3: The transverse momentum of the top/anti-top quarks in the event for all examined  $Z'$  mass points.

1245 of the reconstructed jet from the  $b$ -quark.

1246 Note that the muon is not required to be isolated, instead the muon is tagged by the  $\chi^2_{\text{match}}$   
 1247 tagger. Selecting isolated muons would reduce significantly the number of muons available  
 1248 for tagging. Additionally, as explained a priori, events which exhibit stronger collimation are  
 1249 more likely to emerge from particles with higher masses. By requesting the muons be isolated,  
 1250 the ability to probe those higher mass events is diminished.

1251 Another candidate to replace the traditional isolation selection is the so-called mini-isolation.  
 1252 This variable takes into account the strong collimation of the top products with increasing  
 1253 boost. Mini-isolation is defined as the sum of the measured transverse momenta of all tracks  
 1254 in a cone of size of size  $\Delta R = k_T/p_T^\ell$  around the lepton, where  $k_T$  is an adjustable scale and  $p_T^\ell$   
 1255 is the momentum of the lepton in question. This is known as the absolute mini-isolation. This  
 1256 study uses the relative mini-isolation where the absolute value is scaled by the momentum of  
 1257 the lepton ( $MI/p_T^\ell$ ).

1258 In this analysis the performance of the  $\chi^2_{\text{match}}$  tagger is measured against mini-isolation

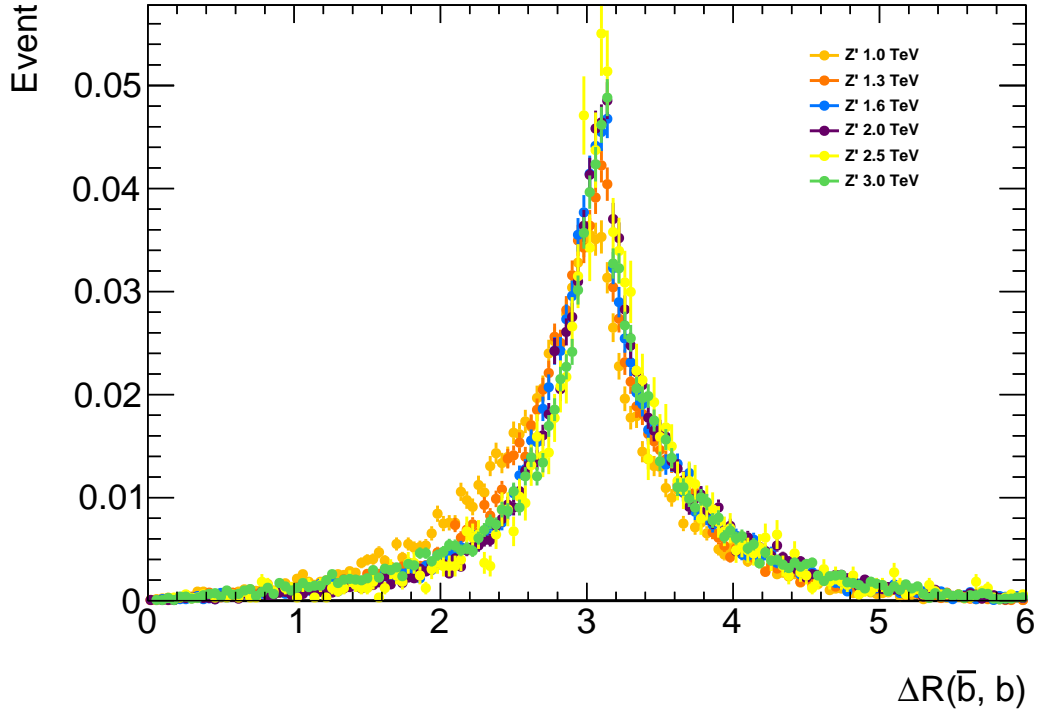


Figure 7.4: The angular separation ( $\Delta R$ ) between the  $b$  and  $\bar{b}$  in the event for all examined  $Z'$  mass points.

1259 using a  $k_T = 10$  and a lepton is deemed isolated if the  $p_T$  in the MI cone is less than 5% that of  
 1260 the lepton. The Muon Tagger operates with the same selection as used in Chapter 5, the cuts  
 1261 are  $|z_0| < 3.0$  mm,  $|d_0| < 3.0$  mm and finally  $\chi^2_{\text{DoF}} < 3.2$ .  
 1262 Thus two separate selections are applied, one for mini-isolation and one for SMT. Note  
 1263 that both methodologies have different muon reconstruction criteria, these are detailed in Ta-  
 1264 ble 7.1.

Table 7.1: Muon reconstruction selection used by Mini-Isolation and by Muon Tagging

Mini-Isolation	Muon-Tagging
MCP Cuts	
$p_T > 20\text{GeV}$	
$ \eta  < 2.5$	
MUID	STACO
$z_0 < 3.0$ mm	Is Combined Muon
IsEM Tight	

1265 The performance of both methodologies are then compared by measuring their efficiency.

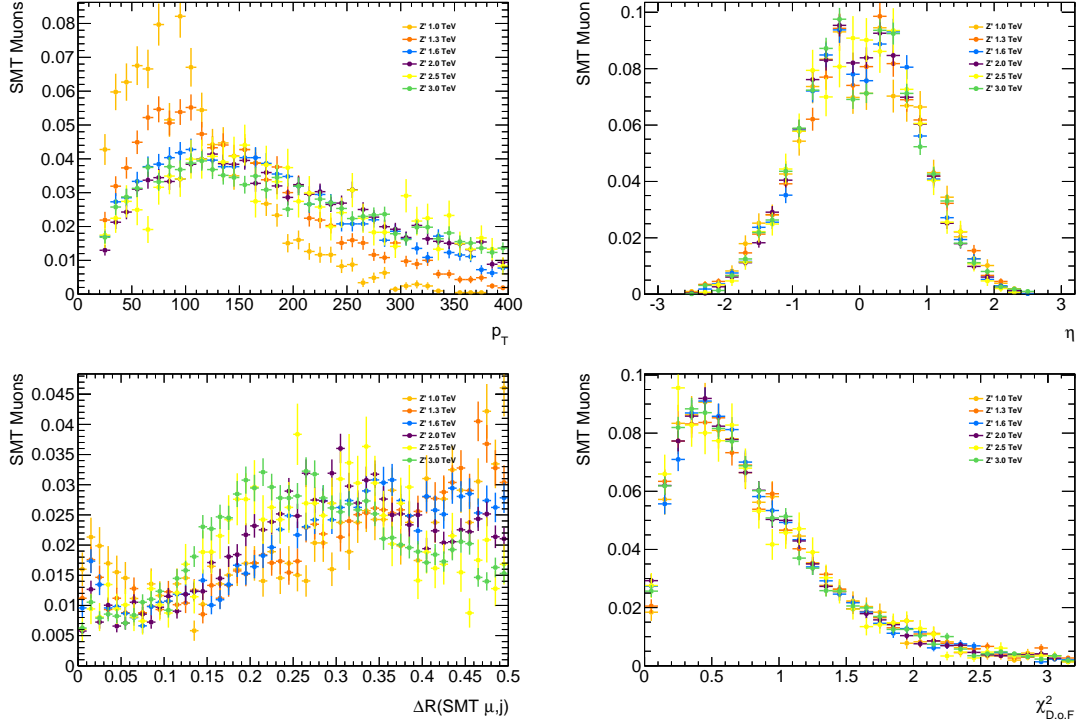


Figure 7.5: This figure shows the distribution of (a) transverse momentum and (b) pseudo-rapidity of muons which pass the SMT selection, the (c) angular separation between those muons and the nearest jet in the event and (d) the  $\chi^2_{\text{match}}$  used in the selection for all tested  $Z'$  mass points.

## 1266 7.4 Efficiency definition

1267 The efficiency measurement was designed to provide an accurate representation of the performance  
 1268 of the soft muon tagger and a valid comparison with mini-isolation. Additional sources  
 1269 of inefficiency such as muon reconstruction are separated out into an additional efficiency  
 1270 which is also quoted. See Figure 7.7 for a summary of the efficiency measurement.

1271 Firstly, events where a  $W$  decays into a muon are selected, this becomes the pool of events  
 1272 from which the efficiency is measured. The selections then diverge and the two sets of recon-  
 1273 struction cuts described in Table 7.1 are applied independently. The efficiency of each sets of  
 1274 reconstruction cuts are measured as:

$$\epsilon_{\text{reco}} = \frac{\text{Muons which pass selection}}{\text{All reconstructed muons}}$$

1275 These good reconstructed muons are then truth-matched to the truth  $\mu$  from the  $W$  if the

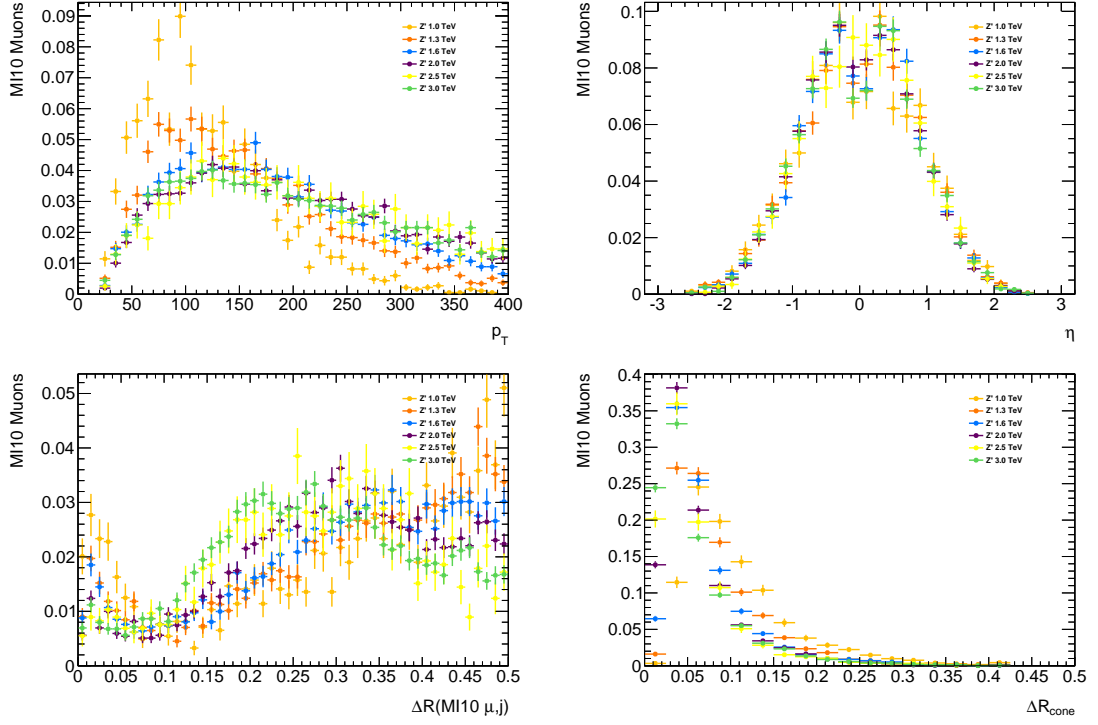


Figure 7.6: This figure shows the (a) transverse momentum and (b) pseudo-rapidity of muons which pass the MI10 selection, the (c) angular separation between those muons and the nearest jet in the event and (d) the cone size used in the selection for all tested  $Z'$  mass points.

1276 angular separate ( $\Delta R$ ) between them is less than 0.01. This has an efficiency associated with  
 1277 it, defined as:

$$\epsilon_{\text{match}} = \frac{\text{Muons matched to truth } W \text{ muon}}{\text{Muons which pass selection}}$$

1278 Note that at each stage the denominator is the numerator of the previous efficiency. This  
 1279 allows for a combination of all the efficiencies to obtain an inclusive measure which can be used  
 1280 to approximate the number of  $W$  muons which would be selected from collision data assuming  
 1281 that the simulation describes the data well.

1282 Next the muons are required to be within  $\Delta R < 0.5$  from a jet. The Muon Tagger requires  
 1283 that jets be near a jet, in addition the impetus behind the analysis is to probe highly boosted  
 1284 events exploiting the capabilities of  $\chi^2_{\text{match}}$  tagging. This selection ensures that the muons  
 1285 available for  $\chi^2_{\text{match}}$  tagging are indeed close to a jet. This selection also has an efficiency  
 1286 associated with it defined as:

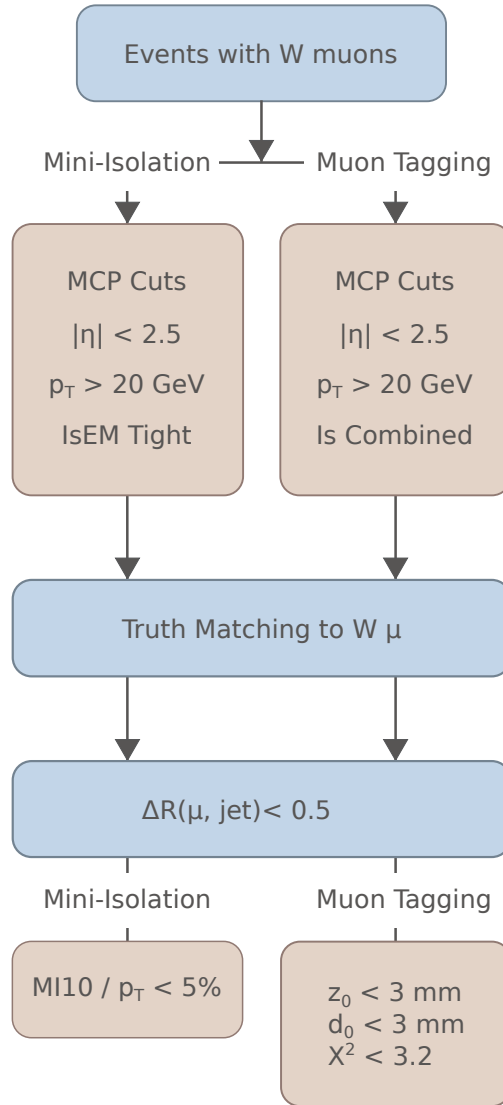


Figure 7.7: Structure of the efficiency measurement.

$$\epsilon_{\text{non-iso}} = \frac{\text{Muons with } \Delta R(\mu, \text{jet}) < 0.5}{\text{Muons matched to truth } W \text{ muon}}$$

<sup>1287</sup> The final step is the application of both the mini-isolation selection and the muon tagging  
<sup>1288</sup> selection discussed a priori. These selections are associated with the final and most interesting  
<sup>1289</sup> sets of efficiencies, defined as:

$$\epsilon_{\text{MT/MI10}} = \frac{\text{Muons which pass MT/MI10 selection}}{\text{Muons with } \Delta R(\mu, \text{jet}) < 0.5}$$

1290 Please note that the denominator in every efficiency is a subset of the previous denominator.

1291 In other words each selection is applied in sequence and the efficiencies are calculated out of  
1292 the remaining muons which passed the previous selection criteria.

1293 Note that in the nominal analysis described in [38] muons which are within  $\Delta R$  of 0.1 of  
1294 the jet would be removed. The impetus behind the analysis is to exploit the  $\chi^2_{\text{match}}$  tagger to  
1295 accept additional events where the signal muon emerges very close to the jet axis, thus overlap  
1296 removal is not part of the  $\chi^2_{\text{match}}$  tagging selection. In order to provide an accurate performance  
1297 comparison between the  $\chi^2_{\text{match}}$  tagger and mini-isolation, the overlap removal is applied only  
1298 for the mini-isolation selection at the end of the chain. The additional acceptance gained by  
1299 using  $\chi^2_{\text{match}}$  tagger is compared to the mini-isolation selection with overlap included:

$$\epsilon = \frac{\text{Muons that pass } \chi^2_{\text{match}} \text{ tagger - MI muons } \Delta R < 0.1}{\text{Total } W \text{ muons}} \quad (7.1)$$

## 1300 7.5 Results

1301 Mini-isolation is a very efficient method for selecting muons. Table 7.2 shows the efficiency  
1302 for the  $\chi^2_{\text{match}}$  tagger, mini-isolation and mini-isolation including overlap removal. Across the  
1303 used mass range, the efficiency of selection remains above 80% and in fact increases with a  
1304 increased  $Z'$  mass. When the  $Z'$  has a mass of 3 TeV the efficiency of selection with mini-  
1305 isolation is 92.5% with no overlap removal. In contrast the efficiency of the  $\chi^2_{\text{match}}$  tagger is  
1306 more consistent across the used mass range and higher than mini-isolation for a given mass.  
1307 For a  $Z'$  with a mass of 3 TeV the measured efficiency of the  $\chi^2_{\text{match}}$  tagger is 96.2%. When  
1308 applying the overlap removal the efficiency of mini-isolation falls to 85.0%. As can be seen  
1309 from Figure 7.8 the efficiency of mini-isolation dips for muons which are close to a jet however  
1310 this occurs below the threshold of the overlap removal. Finally the additional acceptance gained  
1311 as defined in 7.1 is 4.03%. The additional acceptance gained in all mass points is also included  
1312 in Table 7.2.

### 1313 7.5.1 Background

1314 A preliminary examination of the amount of background was performed. This was done on the  
1315 same sample of events but instead of selecting semileptonic events, the all-hadronic events are

$Z'$ Mass [TeV]	$\chi^2_{\text{match}}$	MI10	MI10 + Overlap
1.0	94.9%	83.1%	67.0%
1.3	95.8%	89.0%	79.2%
1.6	95.9%	90.4%	81.9%
2.0	96.0%	92.4%	85.7%
2.5	95.8%	92.8%	85.1%
3.0	96.2%	92.5%	85.0%

Table 7.2: Efficiency of selecting a muon by using the  $\chi^2_{\text{match}}$  tagger against mini-isolation. Note that ‘MI10 + Overlap’ is the efficiency of applying both the mini-isolation cut and overlap removal.

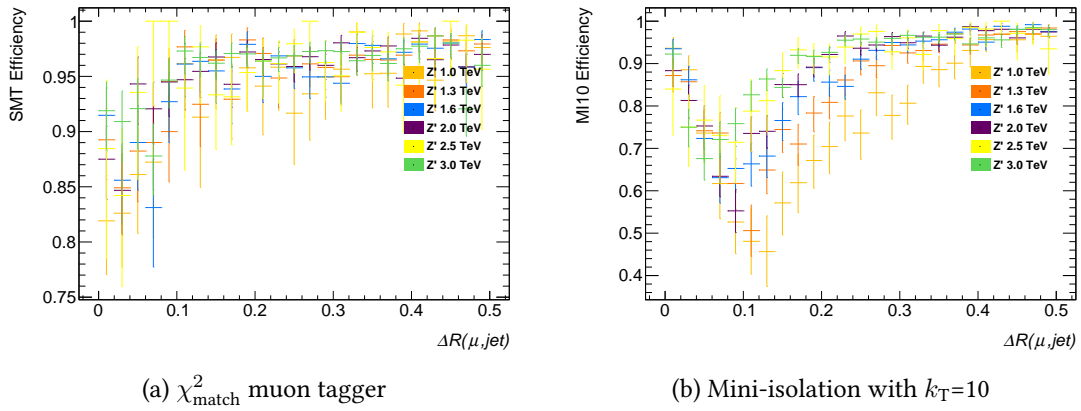


Figure 7.8: Efficiency of mini-isolation ( $k_T=10$ ) and  $\chi^2_{\text{match}}$  tagger as a function of the angular separation between the reconstructed muon and the nearest reconstructed jet. Note the dip in the mini-isolation efficiency at low  $\Delta R$ . In the nominal analysis an overlap removal between the jet and the muon is applied.

used as background. While these events do not perfectly mimic the true background, namely  $b\bar{b}$ , the lack of any real signal muons can provide a suitable preliminary substitute.

The lack of an isolation requirement is expected to result in a substantial increase in the amount of background selected. Additionally the semileptonic  $b$ -decays in  $b\bar{b}$  would result in muons that the  $\chi^2_{\text{match}}$  tagger will select. The analysis chain described in Section 7.4 is repeated on the same sample used a priori however the truth level selection of events with a  $W$  muon is reversed, thus at truth level both  $W$  bosons decay hadronically.

The results of this selection are presented in Table 7.3. As expected mini-isolation removes a substantial amount of background while maintaining very high signal efficiency. In comparison, removing the isolation requirement greatly increases the background acceptance when using the  $\chi^2_{\text{match}}$  tagger. A full treatment of the background would be required to account for

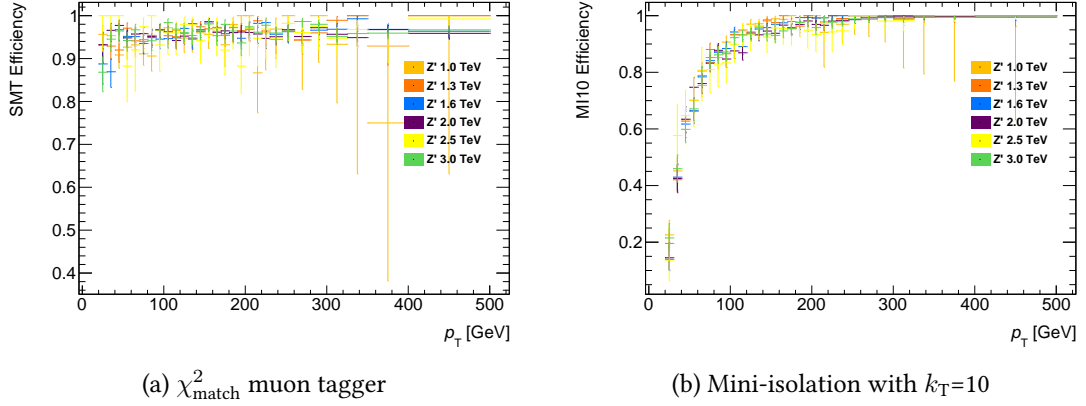


Figure 7.9: Efficiency of mini-isolation ( $k_T=10$ ) and  $\chi^2_{\text{match}}$  muon tagger as a function of the transverse momentum of the muon.

1327 the background present.

1328 The increase in signal acceptance does not make this methodology sufficiently advanta-  
1329 geous particularly when considering the large increase in fake rate. An examination of the  
1330  $b$ -tagging potential of the  $\chi^2_{\text{match}}$  tagger is presented in the next section.

Table 7.3: Fake rate of  $\chi^2_{\text{match}}$  tagger, mini-isolation and mini-isolation including overlap removal as measured using all  $Z'$  mass points.

$Z'$ Mass [TeV]	$\chi^2_{\text{match}}$	MI10	MI10 + Overlap
1.0	92.8%	4.10%	2.39%
1.3	92.4%	4.77%	3.66%
1.6	91.8%	5.46%	4.55%
2.0	91.1%	7.07%	6.09%
2.5	90.0%	6.40%	5.57%
3.0	90.1%	6.59%	5.68%

## 1331 7.6 B-tagging potential in boosted events

1332 As with the non-boosted  $t\bar{t}$  analysis,  $b$ -tagging is used to select boosted  $t\bar{t}$  events. By following  
1333 a similar methodology a sample of muons which likely come from the semileptonic decay of  
1334  $b$ -quarks was constructed. This pool of muons was then used to estimate the efficiency of the  
1335  $\chi^2_{\text{match}}$  tagger in selecting this soft muon.

1336 The analysis chain is designed to compensate for the lack of hadron truth information

Table 7.4: Summary of the number of muons remaining after each selection cut and the efficiency.

$Z'$ Mass [TeV]	CB Muons	Good Muons	$\Delta R(\mu, j) < 0.5$	$\chi^2_{\text{match}}$ -tagged
1.0	74551	25011 (33.5%)	10061 (40.2%)	9472 (94.2%)
1.3	92983	30452 (32.8%)	14995 (49.2%)	14083 (93.9%)
1.6	88722	28041 (31.6%)	15677 (55.9%)	14696 (93.7%)
2.0	108924	32252 (29.6%)	19951 (61.9%)	18572 (93.1%)
2.5	25696	7063 (27.5%)	4580 (64.8%)	4252 (92.8%)
3.0	113702	30959 (27.2%)	19240 (62.1%)	17832 (92.7%)

<sup>1337</sup> and the necessary navigation information<sup>3</sup> to correctly select the truth muon from  $b \rightarrow \mu$  or  
<sup>1338</sup>  $b \rightarrow c \rightarrow \mu$ .

<sup>1339</sup> Firstly jets are matched to the truth  $b$ -quarks in the event. The matching is done by a simple  
<sup>1340</sup>  $\Delta R$  requirement of 0.3. These jets are likely emerging from the  $b$ -quark.

Next the requirement that the muon be not isolated is applied. The nearest STACO muon within a  $\Delta R=0.5$  is selected as the possible soft muon candidate. Finally the SMT selection is applied and the efficiency of this selection is defined as

$$\epsilon_{SMT} = \frac{\text{Number of muons that pass the SMT selection}}{\text{Number of muons within } \Delta R(\mu, j) < 0.5}$$

<sup>1341</sup> The efficiency of  $\chi^2_{\text{match}}$ -tagger appears to decrease by 2% across the  $Z'$  mass range as can  
<sup>1342</sup> be seen from Table 7.4. Despite this small decrease in efficiency, the overall selection is very  
<sup>1343</sup> efficient across the range. Note that the relative number of muons closer to the jet increases  
<sup>1344</sup> with increasing  $Z'$  mass.

---

<sup>3</sup>The relationship between parent and child particles

1345 **Chapter 8**

1346 **Conclusions**

# **Appendices**

1347

1348 **Appendix A**

1349 **List of triggers used in calibration**

1350 The calibration analysis makes use of an OR of the triggers listed below. The triggers fire  
1351 based on a set of criteria summarized in the trigger name following the ATLAS trigger nam-  
1352 ing convention. The list includes generic single low- $p_T$  muon triggers such as EF\_mu6 and  
1353 EF\_mu15, single high- $p_T$  muons & jets triggers such as EF\_mu24\_j65\_a4tchad and  
1354 the specialized  $J/\psi$  trigger EF\_mu6\_Trk\_Jpsi\_loose.

- 1355 • EF\_mu24\_j65\_a4tchad\_EFxe40\_tclcw
- 1356 • EF\_mu4T\_j65\_a4tchad\_xe60\_tclcw\_loose
- 1357 • EF\_mu24\_j65\_a4tchad
- 1358 • EF\_mu18\_tight\_e7\_medium1
- 1359 • EF\_mu4T\_j65\_a4tchad\_xe70\_tclcw\_veryloose
- 1360 • EF\_mu24\_j65\_a4tchad\_EFxe60\_tclcw
- 1361 • EF\_mu24\_tight\_b35\_mediumEF\_j35\_a4tchad
- 1362 • EF\_mu20i\_tight\_g5\_loose\_TauMass
- 1363 • EF\_mu6\_Trk\_Jpsi\_loose
- 1364 • EF\_mu24i\_tight
- 1365 • EF\_mu24i\_tight\_MuonEF

- 1366      • EF\_mu24\_i\_tight\_MG
- 1367      • EF\_mu24\_i\_tight\_12muonSA
- 1368      • EF\_mu24\_tight\_3j35\_a4tchad
- 1369      • EF\_mu24\_g20vh\_loose
- 1370      • EF\_mu40\_MSonly\_barrel\_tight
- 1371      • EF\_mu50\_MSonly\_barrel\_tight
- 1372      • EF\_mu24\_tight\_EFxe40
- 1373      • EF\_mu24\_tight\_L2StarB
- 1374      • EF\_mu18\_medium
- 1375      • EF\_mu24\_medium
- 1376      • EF\_mu24\_tight
- 1377      • EF\_mu24\_tight\_MuonEF
- 1378      • EF\_mu24\_tight\_MG
- 1379      • EF\_mu24\_tight\_L2StarC
- 1380      • EF\_mu36\_tight
- 1381      • EF\_mu40\_tight
- 1382      • EF\_mu20it\_tight
- 1383      • EF\_mu24\_g20vh\_medium
- 1384      • EF\_mu18\_2g10\_medium
- 1385      • EF\_mu24\_muCombTag\_NoEF\_tight
- 1386      • EF\_mu10i\_loose\_g12Tvh\_medium
- 1387      • EF\_mu10i\_loose\_g12Tvh\_medium\_TauMass

- 1388     • EF\_mu18\_2g10\_loose
- 1389     • EF\_mu10i\_g10\_medium\_TauMass
- 1390     • EF\_mu20i\_tight\_g5\_medium\_TauMass
- 1391     • EF\_mu24\_tight\_3j45\_a4tchad
- 1392     • EF\_mu24\_tight\_4j45\_a4tchad
- 1393     • EF\_mu24\_tight\_4j35\_a4tchad
- 1394     • EF\_mu4T
- 1395     • EF\_mu6
- 1396     • EF\_mu15
- 1397     • EF\_mu40\_slow\_tight
- 1398     • EF\_mu60\_slow\_tight1
- 1399     • EF\_mu22\_IDTrkNoCut\_tight
- 1400     • EF\_mu8\_4j45\_a4tchad\_L2FS
- 1401     • EF\_mu6\_Trk\_Jpsi\_loose\_L2StarB
- 1402     • EF\_mu6\_Trk\_Jpsi\_loose\_L2StarA
- 1403     • EF\_mu24\_j65\_a4tchad\_EFxe40wMu\_tclcw
- 1404     • EF\_mu24\_j65\_a4tchad\_EFxe60wMu\_tclcw
- 1405     • EF\_mu6T\_2b55\_medium\_2j55\_a4tchad\_L1J20\_matched
- 1406     • EF\_mu24i\_tight\_muFast
- 1407     • EF\_mu4T\_L2StarB
- 1408     • EF\_mu6\_L2StarB
- 1409     • EF\_mu15\_vbf\_L1TAU8\_MU10

<sup>1410</sup> **Appendix B**

<sup>1411</sup> **List of combined muon performance**  
<sup>1412</sup> **(MCP) cuts**

# <sup>1413</sup> Bibliography

- <sup>1414</sup> [1] Particle Data Group, J. Beringer, et al. The Review of Particle Physics. *Physical Review D*,  
<sup>1415</sup> 86:010001+, 2012.
- <sup>1416</sup> [2] Nikolaos Kidonakis. NNLL threshold resummation for top-pair and single-top production.  
<sup>1417</sup> 2012.
- <sup>1418</sup> [3] Michał Czakon, Paul Fiedler, and Alexander Mitov. Total top-quark pair-production cross  
<sup>1419</sup> section at hadron colliders through  $O(\frac{4}{S})$ . *Phys.Rev.Lett.*, 110(25):252004, 2013.
- <sup>1420</sup> [4] ATLAS Collaboration. The ATLAS experiment at the CERN Large Hadron Collider. *Journal  
of Instrumentation*, 3(08):S08003, 2008.
- <sup>1422</sup> [5] ATLAS Collaboration. Measurement of the t-channel single top-quark production cross  
<sup>1423</sup> section in pp collisions at with the ATLAS detector. *Physics Letters B*, 717(4â5):330 – 350,  
<sup>1424</sup> 2012.
- <sup>1425</sup> [6] B. Odom, D. Hanneke, B. D'Urso, and G. Gabrielse. New Measurement of the Electron  
<sup>1426</sup> Magnetic Moment Using a One-Electron Quantum Cyclotron. *Physical Review Letters*,  
<sup>1427</sup> 97:030801, Jul 2006.
- <sup>1428</sup> [7] ATLAS Collaboration. Observation of a new particle in the search for the Standard Model  
<sup>1429</sup> Higgs boson with the ATLAS detector at the LHC. *Physics Letters B*, 716(1):1 – 29, 2012.
- <sup>1430</sup> [8] Serguei Chatrchyan et al. Observation of a new boson at a mass of 125 GeV with the CMS  
<sup>1431</sup> experiment at the LHC. *Phys.Lett.*, B716:30–61, 2012.
- <sup>1432</sup> [9] P.A.R. Ade et al. Planck 2013 results. I. Overview of products and scientific results. 2013.
- <sup>1433</sup> [10] D.H. Perkins. *Introduction to High Energy Physics*. Cambridge University Pres, 2000.

- 1434 [11] D. Griffiths. *Introcution to Elementary Particles*. John Wiley & Sons, Inc, 1987.
- 1435 [12] N. Cabibbo. Unitary Symmetry and Leptonic Decays. *Physical Review Letters*, 10:531–533,  
1436 Jun 1963.
- 1437 [13] M. Kobayashi and Toshihide Maskawa. CP-Violation in the Renormalizable Theory of  
1438 Weak Interaction. *Progress of Theoretical Physics*, 49(2):652–657, 1973.
- 1439 [14] Ling-Lie Chau and Wai-Yee Keung. Comments on the parametrization of the kobayashi-  
1440 maskawa matrix. *Phys.Rev.Lett.*, 53:1802, 1984.
- 1441 [15] Lincoln Wolfenstein. Parametrization of the Kobayashi-Maskawa Matrix. *Physical Review  
Letters*, 51:1945–1947, Nov 1983.
- 1442 [16] K. Marathe. *Topics in Physical Mathematics*. Springer, 2010.
- 1443 [17] J. J. Aubert, U. Becker, P. J. Biggs, J. Burger, M. Chen, G. Everhart, P. Goldhagen, J. Leong,  
1444 T. McCorriston, T. G. Rhoades, M. Rohde, Samuel C. C. Ting, Sau Lan Wu, and Y. Y. Lee.  
1445 Experimental observation of a heavy particle j. *Physical Review Letters*, 33(23):1404–1406,  
1446 1974.
- 1447 [18] J. H. Christenson, J. W. Cronin, V. L. Fitch, and R. Turlay. Evidence for the  $2\pi$  decay of  
1448 the k20 meson. *Physical Review Letters*, 13(4):138–140, 1964.
- 1449 [19] Steven Weinberg. A model of leptons. *Physical Review Letters*, 19(21):1264–1266, 1967.
- 1450 [20] Sheldon L. Glashow. Partial-symmetries of weak interactions. *Nuclear Physics*, 22(4):579  
1451 – 588, 1961.
- 1452 [21] Abdus Salam. Weak and Electromagnetic Interactions. *Conf.Proc.*, C680519:367–377, 1968.
- 1453 [22] G. Arnison et al. Experimental observation of isolated large transverse energy electrons  
1454 with associated missing energy at  $\sqrt{s} = 540$  GeV. *Physics Letters B*, 122(1):103 – 116, 1983.
- 1455 [23] S. W. Herb, D. C. Horn, L. M. Lederman, J. C. Sens, H. D. Snyder, J. K. Yoh, J. A. Appel,  
1456 B. C. Brown, C. N. Brown, W. R. Innes, K. Ueno, T. Yamanouchi, A. S. Ito, H. Jostlein, D. M.  
1457 Kaplan, and R. D. Kephart. Observation of a Dimuon Resonance at 9.5 GeV in 400-GeV  
1458 Proton-Nucleus Collisions. *Physical Review Letters*, 39:252–255, Aug 1977.

- 1460 [24] CDF Collaboration. Observation of top quark production in  $p\bar{p}$  collisions with the collider  
 1461 detector at Fermilab. *Physical Review Letters*, 74:2626–2631, Apr 1995.
- 1462 [25] D0 Collaboration. Search for high mass top quark production in  $p\bar{p}$  collisions at  $\sqrt{s}=1.8$   
 1463 tev. *Physical Review Letters*, 74:2422–2426, Mar 1995.
- 1464 [26] ATLAS Collaboration. Search for top pair candidate events in ATLAS at  $\sqrt{s}=7$  TeV, Jul  
 1465 2010.
- 1466 [27] CMS Collaboration. Selection of top-like events in the dilepton and lepton-plus-Jets chan-  
 1467 nels in early 7 TeV Data, 2010.
- 1468 [28] Johann H. Kuhn, A. Reiter, and Peter M. Zerwas. Z Decays to Top Quarks. *Nuclear Physics*,  
 1469 B272:560, 1986.
- 1470 [29] M. Aliev, H. Lacker, U. Langenfeld, S. Moch, P. Uwer, et al. HATHOR: HAdronic Top and  
 1471 Heavy quarks crOss section calculatoR. *Comput.Phys.Commun.*, 182:1034–1046, 2011.
- 1472 [30] Matteo Cacciari, Michal Czakon, Michelangelo L. Mangano, Alexander Mitov, and Paolo  
 1473 Nason. Top-pair production at hadron colliders with next-to-next-to-leading logarithmic  
 1474 soft-gluon resummation. *arXiv:1111.5869 [hep-ph]*, 2011.
- 1475 [31] O.W. Greenberg. CPT violation implies violation of Lorentz invariance. *Phys.Rev.Lett.*,  
 1476 89:231602, 2002.
- 1477 [32] ATLAS Collaboration. Measurement of the mass difference between top and anti-top  
 1478 quarks in pp collisions at  $\sqrt(s) = 7$  TeV using the ATLAS detector. *Phys.Lett.*, B728:363–  
 1479 379, 2014.
- 1480 [33] Serguei Chatrchyan et al. Measurement of the mass difference between top and antitop  
 1481 quarks. *JHEP*, 1206:109, 2012.
- 1482 [34] Lyndon Evans and Philip Bryant. Lhc. *Journal of Instrumentation*, (08):S08001.
- 1483 [35] The ATLAS Collaboration. Luminosity determination in pp collisions at  $\text{sqrt}(s)=7$  tev  
 1484 using the atlas detector at the lhc. *The European Physical Journal C*, 71(4), 2011.
- 1485 [36] ATLAS detector and physics performance: Technical Design Report, 1, 1999.

- 1486 [37] ATLAS Collaboration. Measurement of the charge asymmetry in top quark pair produc-  
1487 tion in pp collisions at  $\text{sqrt}(s) = 7$  tev using the atlas detector. *The European Physical  
1488 Journal C*, 72(6), 2012.
- 1489 [38] ATLAS Collaboration. Search for  $t\bar{t}$  resonances in the lepton plus jets final state with  
1490 ATLAS using  $4.7 \text{ fb}^{-1}$  of  $pp$  collisions at  $\sqrt{s} = 7 \text{ TeV}$ . *Physical Reviews D*, D88(1):012004,  
1491 2013.
- 1492 [39] A search for  $t\bar{t}$  resonances in the lepton plus jets final state with ATLAS using  $14 \text{ fb}^1$  of  
1493  $pp$  collisions at  $\sqrt{s} = 8 \text{ TeV}$ , May 2013. Not published in the proceedings.
- 1494 [40] Serguei Chatrchyan et al. Search for  $Z'$  resonances decaying to  $t\bar{t}$  in dilepton+jets final  
1495 states in  $pp$  collisions at  $\sqrt{s} = 7 \text{ TeV}$ . *Phys.Rev.*, D87:072002, 2013.
- 1496 [41] Serguei Chatrchyan et al. Search for anomalous  $t\bar{t}$  production in the highly-boosted all-  
1497 hadronic final state. *JHEP*, 1209:029, 2012.
- 1498 [42] CMS Collaboration. Search for  $t\bar{t}$  resonances in semileptonic final state, 2013.
- 1499 [43] Torbjorn Sjostrand, Stephen Mrenna, and Peter Skands. Pythia 6.4 physics and manual.  
1500 *Journal of High Energy Physics*, 2006(05):026–026, 2006.
- 1501 [44] J. Pumplin, D.R. Stump, J. Huston, H.L. Lai, Pavel M. Nadolsky, et al. New generation of  
1502 parton distributions with uncertainties from global QCD analysis. *JHEP*, 0207:012, 2002.